RELATION OF OPTICAL PROPERTIES TO STRUCTURE AND A MULTILAYER MODEL FOR HYDROGENATED SILICON

by

Theodore Victor Herak

A thesis

presented to the University of Manitoba

in partial fulfillment of the

requirements for the degree of

Doctor of Philosophy

in

Electrical Engineering

Winnipeg, Manitoba, 1987

ISBN 0-315-37286-9

RELATION OF OPTICAL PROPERTIES TO STRUCTURE AND A MULTILAYER MODEL FOR HYDROGENATED SILICON

BY

THEODORE VICTOR HERAK

A thesis submitted to the Faculty of Graduate Studies of the University of Manitoba in partial fulfillment of the requirements of the degree of

DOCTOR OF PHILOSOPHY

ABSTRACT

The optical and electronic properties of a-SiN_x:H alloy films fabricated by rf glow-discharge in SiH_4-N_2-H_2 have been measured for $0 \leq x \leq 0.6$. The optical gap is about 1.65 eV and is practically independent of x for $0.1 \leq x \leq 0.4$, but it increases rapidly with increasing x for $0 < x < 0.1$ and $x > 0.4$. The dark conductivity, the photoconductivity, and the ratio of the photoconductivity to dark conductivity are enhanced by nitrogen incorporation when appropriate nitrogen content is used. It is observed that the activation energy for extended-state electron conduction is unaffected by N content for $x \leq 0.4$, indicating that nitrogen does not act as a donor. The electron mobility in extended states is improved by as much as a factor of 10 by N incorporation. There is a rapid conversion from the tetrahedral network to a Si_3N_4 network as x increases above approximately 0.4.

Both amorphous and microcrystalline hydrogenated silicon films have been fabricated by microwave plasma processing in a silane-hydrogen gas mixture, in which the plasma can be made to exhibit electron cyclotron resonance (ECR). X-ray diffraction measurements and spectroscopic ellipsometry over the range of 2.0 eV to 3.5 eV indicate that the optical gap decreases from 1.70 eV to 1.40 eV as the structure changes from an amorphous network into a microcrystalline-amorphous mixture. The amorphous to microcrystalline transition is clearly indicated by the spectra of the refractive index n, and the imaginary part of the dielectric constant ϵ_2.

For ellipsometric data analysis, a multilayer optical model has been developed. The dielectric response of each layer is calculated as a function of the amorphous, crystallite, and void volume fractions through an effective medium approximation. Effects of bond length dilation, bond angle distortion and void content on the dielectric response are considered within the Penn-Phillips model of amorphous semiconductors. Ellipsometric and X-ray diffraction data indicate that the transition from amorphous to microcrystalline structure is accompanied by a reduction in material density and a significant increase in the surface roughness overlayer. X-ray diffraction measurements estimate a higher volume fraction of crystallites as compared to that obtained from optical data.

The optical, electronic and structural properties of a-Si:H films deposited by ECR microwave plasmas have been studied as functions of substrate bias. Films deposited on quartz and stainless steel substrates with their surfaces normal to the dc magnetic field display good optical and electronic properties. For moderate negative bias, the films deposited on stainless steel substrates consistently exhibited higher density and better optical and electronic properties compared to films deposited on quartz substrates. These properties are explained in terms of ion bombardment of the growing films and they are correlated with Langmuir probe plasma studies. Ion bombardment of the growing films plays an important role in film quality.

ACKNOWLEDGEMENTS

I would like to thank the Sendai group of Japan who provided the hydrogenated silicon nitrogen alloy films used in this study. The optical and electrical characterization of the films as well as the interpretation of these results (Chapter 2) were the responsibility of our Materials and Devices Research Laboratory in this collaboration with the Sendai group. R.D. McLeod was responsible for the electrical characterization, while optical characterization and annealing studies were due to myself.

Our laboratory, in particular S.R. Mejia and R.D. McLeod, have developed a new technique for thin film deposition. This new technique, microwave glow discharge, was used to fabricate the films discussed in Chapters 3, 5, and 6. Thanks therefore are due to R.D. McLeod and S.R. Mejia and also to T. Chau, who along with S.R. Mejia, were the main people responsible for operation of the deposition system and film fabrication. Also I would like to acknowledge J.J. Schellenberg and P.K. Shufflebotham. In this work, the x-ray diffraction measurements were due to J.J. Schellenberg and myself, while infrared absorption and Langmuir probe data shown in Figs. 5.6 and 6.4, respectively, were collected by P.K. Shufflebotham. Dark conductivity data given in Fig. 3.8 is due to J.J. Schellenberg. Along with S.R. Mejia and R.D. McLeod, their helpful discussion is gratefully appreciated.

Finally, I would like to thank Dr. H.C. Card and in particular Dr. K.C. Kao, for their guidance and advice concerning all aspects of this work.

TABLE OF CONTENTS

LIST OF FIGURES

Fig. 3.5 Refractive index versus photon energy for μc-Si:H films with relative volume fraction of crystallites, rf_v, as a parameter. rf_v: 0 (●), 0 (■), 0.07 (▲), 0.23 (○), 0.42 (□), 0.77 (△), 0.82 (+), and 1.0 (✕). Note, film A: (■) see text. The inset shows the refractive index versus photon energy of crystalline Si (after [3.22]).

Fig. 3.6 Refractive index at $h\nu$ = 2.0 eV of μc-Si:H films versus relative volume fraction of crystallites.

Fig. 3.7 Optical energy gap of μc-Si:H films versus relative volume fraction of crystallites.

Fig. 3.8 Optical energy gap of a-Si:H and μc-Si:H films versus room temperature dark conductivity.

Fig. 4.1 Comparison of the dielectric constants of a-Si (after [4.11]), a-Ge (after [4.12]), and a-Si_3N_4 (after [4.13]).

Fig. 4.2 A cluster of the form of the Bethe Lattice. Shells 1 and 2 are indicated. Shell 2 has 12 atoms and 36 bonds are external to the cluster.

Fig. 4.3 View of a tetragonal lattice along the [001] direction. Views along the [100] and [010] directions are identical due to the symmetry of the lattice. A void in the lattice can be created by removing a cube or a unit cell as indicated by the dashed line in (a). A larger void of dimension L=ma, or m^3 stacked unit cells, as shown in (b). In (a), shaded atoms have no bonds that are external to the void created by cutting along the dashed line. These atoms are omitted in (b) for clarity.

Fig. 6.7 The B-parameter defined by $\alpha h\nu = B(h\nu - E_{opt})^2$ as a function of substrate bias V_b, for a-Si:H films deposited on stainless steel substrates.

Fig. 6.8 Dark conductivity, σ_d, photoconductivity, σ_{ph}, and σ_{ph}/σ_d at room temperature as functions of table bias for a-Si:H films deposited on stainless steel (solid line) and quartz substrates (dotted line). Photoconductivity data is shown for a photon flux of 10^{15} photons-s^{-1}-cm^{-2} at λ = 6328 A

LIST OF TABLES

CHAPTER 1

INTRODUCTION

Amorphous materials may be simply defined as materials without long range order of atoms as is the case for crystalline materials. These materials are generally formed by the undercooling of a liquid or the condensation of a vapour onto a cold substrate. This will result in the formation of structural "defects" which disturbs the periodicity of the atomic arrangement. Materials having semiconducting properties are usually referred to as "non-crystalline semiconductors" or "amorphous semiconductors". The classification of materials into metals, semiconductors, and insulators is based on band theory[1.1,1.2], the starting point of which is a periodic arrangement of atoms in a crystalline structure. This theory has obviously been very successful in predicting the electrical and optical properties of crystalline solids. However, many solids are not crystalline, but are amorphous. A solid of amorphous structure generally exhibits similar electrical and optical properties to those of the same solid of crystalline structure, suggesting that the band theory of solids can be applied to amorphous material with some modifications. The theory of crystalline solids is now being further developed to apply to the more general class of solids, that is, amorphous or non-crystalline solids.

From a purely scientific point of view, there is much insight into the physics of solids to be gained from the study of amorphous materials. Also, these materials

have the potential for a wide range of applications. They exhibit a wide range of properties allowed by the relaxation of the constraints associated with long range order. Materials composed of exactly the same elements can have completely different structural and optoelectronic properties, depending on their fabrication processes, and optical and thermal histories. In Chapter 2 it will be shown that the optical and electronic properties of amorphous silicon films can be changed by heat treatment, suggesting that these materials have many quasi-stable configurations.

Since it is directly related to many properties of crystalline and amorphous materials, let us consider the electronic structure of these solids. The conventional approach to the understanding of the electronic structure of crystalline solids is to require that the one-electron potential energy exhibit the periodicity of the lattice. Calculations are generally made involving a small number of atoms in a single primitive cell from which the entire crystal can be generated. All electronic states are "extended" throughout the solid, and therefore, all electronic and optical properties can be interpreted in terms of a band theory. The distribution of the density of states takes the form of alternating regions of energy where states are allowed called "bands", separated from regions where no states are allowed, called "gaps". For crystalline silicon, the width of the valence band and conduction band is of the order of 4.3 eV, and they are separated by a gap of about 1.2 eV. The sharp structure in the density of states distribution of crystalline solids is as a consequence of the long range order of the lattice. The properties of amorphous solids, being similar to their crystalline counterpart, suggests that the density of states distribution in amorphous solids should be of similar form to that for the crystalline case, with some "minor"

pertubations. In fact, it is believed that the density of states distribution is more strongly associated with the local atomic environment rather than long range order[1.3,1.4].

By considering the local atomic environment, the effects of disorder, for example bond length dilation, can be studied. Either bond stretching or bond bending can introduce "localized" states into the energy gap. With increasing disorder, the density of states distribution loses its sharp structure at the band edges and is replaced with band tails, that is, a gradual decrease of the density of states with some states occurring in the forbidden region or band gap. These states, rather than being extended, now behave as "localized" states in which the electrons occupying these states are confined spatially. The valence and conduction band tails may be so extensive that they intersect at midgap, as shown in Fig. 1.1. This is the CFO model proposed by Chohen, Fritzche, and Ovshinsky[1.5]. Two critical energies for which carrier mobility increases sharply, are now defined as the band edges, and their separation as the "mobility gap". Some normally filled valence band states have energies in excess of normally empty conduction band states, resulting in a repopulation to restore equilibrium. Most other models for the density of states distribution in amorphous semiconductors are similar to the CFO model.

Localized states in the gap can also arise from impurities or defects, in addition to states due to the overlap of band tails. The magnitude of the density of states at the Fermi level $g(E_f)$, is an important parameter, and is dependent on the details of the material processing. If $g(E_f)$ is small, these states have little effect on the

electronic properties of the material, and E_f can be easily modulated by, for example, doping or charge induction. For larger values of $g(E_f)$, there is an increasing tendency to pin the Fermi level, thereby making it difficult to observe any doping effects or observe a field effect (large change in conductivity due to induction of excess charge). Perhaps the most important type of defect in amorphous material is the so-called "dangling bond", which yields localized states in the gap.

In crystalline silicon, each Si atom has four nearest neighbours. The Si atoms are said to be four-fold coordinated, each atom forming four covalent bonds with its nearest neighbours, thereby satisfying its valence requirements. An under coordinated atom is considered a defect center, the simplest of which is the three-fold coordinated Si atom, and is referred to as a "dangling bond". Dangling bonds, prevalent in amorphous material, are of extreme importance since $g(E_f)$ is directly related to the electronic properties. The reduction of the localized gap states due to dangling bonds and resultant improvement in electronic properties was the main impetus in the current wave of activity in the characterization of amorphous silicon. We shall come back to this point later.

At this time then, the most popular model for the density of states distribution in amorphous silicon is the Davis-Mott Model[1.5] or some variation of it. This is shown in Fig. 1.1(b), where localized states near band edges or band tails do not overlap and localized states near the midgap are due mainly to dangling bonds. Present thinking is that overlapping tails do not exist in amorphous semiconductors.

The classification of electronic states by k-vector (wave vector) is without meaning in amorphous semiconductors since lattice periodicity does not exist[1.5,1.6]. However, it is still appropriate to examine the state density and their localized or extended character as a function of energy. Several theoretical calculations or models exist.

(1) "Tight-binding models"[1.7]. This approach employs the tight binding approximation in which the electronic wavefunctions are linear combinations of atomic orbitals. Schrodinger's equation is then solved for the one-electron energy levels. Although this method is crude, it emphasizes the short range order and hence is applicable to amorphous materials. The approach concentrates on the effect of topological disorder (no long range order) but neglects quantitative disorder corresponding to a spread in the bond angles and next-nearest-neighbour interactions.

(2) "Crystalline polymorphs"[1.8]. In this approach the density of states is approximated by extrapolating from or averaging over the density of states calculated for various actual or hypothetical crystalline forms, all satisfying chemical valence requirements. Various atomic structural arrangements considered include the wurtzite configuration, the body centered cubic configuration, and the simple tetragonal configuration, the local disorder increasing through this series.

(3) "Cluster models"[1.9]. Multiple scattering theory is applied to clusters of up to the order of 50 atoms, for several configurations corresponding to those known or guessed to exist in amorphous materials. The final density of states is obtained by averaging over the different types of clusters. Periodic boundary conditions may be applied to the clusters.

(4) "Penn-Phillips approximation"[1.10,1.11]. In this model the macroscopic optical properties such as the dielectric constants are used to establish a small number of basic parameters, such as an average energy gap. This general model may be used to correlate various parameters in a self consistent manner. In Chapter 4 we will use this model to investigate the effects of void content, bond stretching and bond bending on the dielectric constant for amorphous and microcrystalline silicon films.

All these models predict that the sharp structure in the density of states distribution in the conduction and valence bands disappears because of lack of long range order. Also, these calculated results suggest the existence of a pseudogap between large conduction and valence band state densities, with states near the band edges assuming an increasingly localized character as their energy penetrates deeper into the otherwise crystalline band gap. These results can be well described in the CFO or Mott-Davis model of the density of states distribution. The existence of good short range order suggests that the simplest structural defects perturb the network equally at all locations and therefore give spatially localized states in a narrow band of energies of the pseudogap.

The structure of the amorphous material determines the density of states distribution which in turn determines the optical properties of the material. The optical properties usually deduced from the band theory calculations for comparison with experiment are related to the imaginary part of the dielectric constant ϵ_2. In Chapters 3 to 5, we shall discuss the relation between structural and optical properties of silicon films based on the Penn-Phillips Model. The imaginary part of the dielectric constant is given by

$$\epsilon_2(E) = const. \cdot J(E) \cdot M(E)/E^2 \quad , \tag{1.1}$$

where $J(E)$ is the joint density of states for optical transitions at energy E, and $M(E)$ is an average matrix element for transitions between valence and conduction band states. The quantity $M(E)/E^2$, the average dipole matrix element, is essentially an average probability for optical transitions between initial and final states. Joannopoulos et al.[1.4] have concluded from calculations of $\epsilon_2(E)$, $J(E)$, and $M(E)$ for several silicon polymorphs that the shape of ϵ_2 is mainly determined by the matrix element $M(E)$. For all tetrahedrally bonded amorphous solids, ϵ_2 as a function of energy has the same form as $M(E)$, since the forms of $J(E)/E^2$ and $M(E)$ are similar in all these cases.

To make comparisons between optical absorption edges for various amorphous Si films, we usually use the optical bandgap E_{opt}, which is defined on the basis of a parabolic absorption edge following the well known emperical relation[1.6]

$$\alpha = const. \cdot (h\nu - E_{opt})^2 \quad , \tag{1.2}$$

where α is the absorption coefficient and $h\nu$ is the photon energy. A rough justification of Eqn(1.2) is as follows[1.6]. In an amorphous solid, since k is no longer a good quantum number due to lack of long range order, all pairs of states (filled at energy E, and empty at energy $E + h\nu$) can be assumed to participate in optical transitions. By assuming constant matrix elements over a small range of energies near the absorption edge, Eqn(1.1) becomes

$$\epsilon_2(h\nu) = const. \cdot \int n_v(E) n_c(E + h\nu) dE \quad , \tag{1.3}$$

where $n_v(E)$ and $n_c(E)$ are the density of states of the valence and conduction bands, respectively. Assuming parabolic bands at the band edges, $n_v \propto (E_v - E)^{1/2}$ and $n_c \propto (E - E_c)^{1/2}$ as in crystalline material, gives

$$\epsilon_2 \propto (h\nu - E_{opt})^2 \quad , \tag{1.4}$$

where $E_{opt} = E_c - E_v$, and E_c and E_v are the conduction and valence band edges, respectively. Since

$$\alpha = \frac{2\pi\epsilon_2}{n\lambda} \quad , \tag{1.5}$$

where the refractive index n, and the wavelength λ, are approximately constant in the narrow spectral range near the absorption edge, Eqn(1.2) follows. The optical gap is one of many parameters generally used to characterize amorphous semiconductor films.

There are many techniques for fabricating amorphous material in thin film form which by far is the most common form of an amorphous solid. These techniques include electron beam or thermal evaporation[1.12], dc and rf (radio-frequency) sputtering[1.13], chemical vapour deposition[1.14], and the widely used glow-discharge techniques[1.15-1.17].

Amorphous films may be prepared by evaporation of an existing bulk material by either electron beam or resistive heating. For high purity silicon films, electron beam evaporation is preferred, due to the reactivity of silicon with most resistive heating sources[1.18]. Sputtering is process in which material is removed predominantly in atomic form by bombardment of energetic ionic particles which are formed in a glow discharge and gain energy from an accelerating electric field. When an ion impacts the target, ejection of one atom from the target may occur. Condensation of these atoms on any exposed substrate then forms a thin film.

The thin film deposition based on thermal decomposition of a gas mixture is generally termed chemical vapour deposition (CVD). CVD can also be accomplished by glow discharge decomposition, or plasma assisted CVD, however, it is common practice to refer to CVD in the restricted sense of thermally assisted CVD. Typical process temperatures are in the range of 900° - 1100°C which is sufficient to dissociate the gas mixture with the resultant condensation forming a thin solid film.

The broad class of plasma assisted or plasma enhanced CVD includes dc glow discharge, rf glow discharge, and the relatively new technique, microwave (MW) glow discharge[1.19]. In Chapter 3 we shall discuss the properties of silicon films

deposited from a MW plasma which can be made to undergo electron cyclotron resonance. The properties of the films prepared in such a novel way are inherently different from those prepared by other methods.

Each method of deposition has its own inherent problems. Film growth rates on the order of 1 A/s are typical for the deposition of silicon films via glow discharge. While this rate appears to be sufficient for thin film device applications, recent progress in device applications such as photovoltiac cells and electrophotography demands further increase in the deposition rate if the required film thicknesses are to be achieved in an acceptable time length. The so called Staebler-Wronski effect, that is the degradation of film properties by prolonged optical exposure, also presents problems in amorphous structure based devices. A correlation between photocreated defects and incorporation or penetration of oxygen contaminants has been reported[1.20]. In glow discharge systems, difficulty obviously exists in incorporating materials which are not directly available in a gaseous form. Sputtering is widely believed to be an unsuitable technology for surface-sensitive devices due to the ion and electron bombardment of the film during fabrication. Effects of ion bombardment on film properties have been studied and will be discussed in Chapter 6. It should be noted that some ion bombardment is required to produce "good" quality amorphous silicon films. CVD is limited by the high process temperatures required. Lower temperatures are required if, for example amorphous silicon is to be deposited, since silicon undergoes an amorphous to crystalline transition at approximately 600°C.

Amorphous silicon, a-Si, can be considered as the most technologically important amorphous semiconductor today. The electrical and optical properties of a-Si films are strongly influenced by both the method of preparation and the conditions during their fabrication. Many, if not all, of the properties of a-Si are directly related to the presence of bonded hydrogen. Reduction of the density of localized states near midgap was possible by alloying silicon and hydrogen (a-Si:H). Hydrogen "readily' satisfies the valence requirements of an otherwise three-fold coordinated Si atom, or dangling bond, thereby reducing $g(E_f)$. It then became possible to successfully dope a-Si:H n- or p-type[1.21], and the importance of hydrogen was finally realized. Discharge-grown a-Si films may contain up to an estimated concentration of 50 atomic percent of hydrogen[1.22]. Apart from its ability to reduce dangling bonds, the influence of hydrogen on the optical and electronic properties has been the subject of extensive study[1.23-1.25]. The more important factors affecting discharge-grown films appear to be, the type of discharge and the substrate temperature during deposition[1.26], which play decisive roles in determining the optical and optoelectronic properties. Photoconductivity studies on dc and rf glow discharge films indicate that the kinetics of the discharge used is an important parameter in determining film properties. Glow discharge films[1.27,1.28] are characterized by high resistivity, good photoconductive properties, and a high optical bandgap, all properties being dependent on controllable experimental conditions.

Amorphous Si films produced by evaporation or sputtering methods in the absence of hydrogen[1.29,1.30] are characterized by low resistivity for as-prepared

films, a low optical bandgap, and poor photoconductivity. The poor properties of these films have been attributed to a high density of localized states due to the absence of hydrogen. The properties of these films, however, can be improved by sputtering the films in Ar/H_2 gas mixtures[1.31,1.32]. Films fabricated in this manner have properties similar to those of glow discharge-grown films. Chittick et al.[1.16] were the first to clearly demonstrate the beneficial effects of hydrogen incorporation in amorphous silicon films.

Possible applications of amorphous materials, and in particular hydrogenated amorphous silicon, a-Si:H, and its alloys, includes solar cells, strain gauges, optical waveguides, electroluminescent devices, thin film transistors, CCD arrays and switching devices. However, to date, only solar cells are commercially available. While many possible applications are being developed through a-Si:H technology, the use of silicon based alloys has served to enhance certain properties for a particular device[1.18]. In Chapter 2, we shall discuss the basic optoelectronic properties of amorphous silicon nitrogen alloy films, one of the more extensively studied silicon based alloys. In addition to the importance of amorphous Si_3N_4 in VLSI applications, silicon-nitrogen alloy films have the potential for use as photoreceptors for electrophotography or as photodetectors. This is as a result of high photo- to dark-conductivity ratios attainable. Fine control of the optical bandgap and optoelectronic properties of silicon based amorphous materials will give a greater flexibility in the design of spectral sensitivity in thin film photovoltaic cells and imaging pickup devices.

References

[1.1] A.H. Wilson, "Theory of Metals", (Cambridge University Press, New York, 1936).

[1.2] F.Bloch, Z. Physik **52,** 555 (1928).

[1.3] David Adler in "Physical Properties of Amorphous Materials", D. Adler, B.B. Schwartz, and M.C. Steele Ed. (Plenum Press, New York, 1985).

[1.4] J.D. Joannopoulos and M.L. Cohen, Solid State Commun. **13,** 1115 (1973).

[1.5] N.F. Mott and E.A. Davis, "Electronic Processes in Non-Crystalline Materials, 2nd Ed.", (Clarendon Press, Oxford, 1979).

[1.6] R. Zallen, "The Physics of Amorphous Solids", (Wiley, New York, 1983).

[1.7] J.R. Reitz, Solid State Phys. **1,** 1 (1955).

[1.8] R. Alben, R. Goldstein, M.F. Thorpe, and D. Weaire, Phys. Stat. Sol. B **53,** 545 (1972).

[1.9] J. Ziman, J. Phys. C **4,** 3129 (1971).

[1.10]D.R. Penn, Phys. Rev. **128,** 2093 (1962).

[1.11]J.C. Phillips, Rev. Mod. Phys. **42,** 317 (1970).

[1.12]S.K. Bahl and S.M. Bhagat, J. Non-Cryst. Solids **17,** 409 (1975).

[1.13]B. Chapman, "Glow Discharge Processes", (Wiley, New York, 1980).

[1.14]B.A. Scott, R.M. Plecenik, and E.E. Simonyi, Appl. Phys. Lett. **39,** 73 (1981).

[1.15]H.F. Sterling and R.C.G. Swann, Solid State Electr. **8,** 653 (1965).

[1.16]R.C. Chittick, J.H. Alexander, and H.F. Sterling, J. Electrochem. Soc. **116,** 77 (1969).

[1.17]Semiconductors and Semimetals **21,** "Hydrogenated Amorphous Silicon, Part A" J. Pankove Ed. (Academic Press, 1984) p. 41.

[1.18]P.K. Shufflebotham, H.C. Card, and A. Thanailakis, J. Non-Cryst Solids, accepted for publication Dec. 8 (1986).

[1.19]S.R. Mejia, R.D. McLeod, K.C. Kao, and H.C. Card, Rev. Sci. Instr. **57,** 493 (1986).

[1.20]D.E. Carlson, "Proc. U.S.-Japan Jt. Semin. Technol. Appl. Tetrahedral Amorphous Solids", (1982).

[1.21]W.E. Spear and P.G. LeComber, Solid State Commun. **17,** 1193 (1975).

[1.22]M.H. Brodsky, M.A. Fritsche, J.F. Ziegler, and W.A. Lanford, Appl. Phys. Lett. **30,** 561 (1977).

[1.23]J.C. Knights, G. Lucovsky, and R. Nemanich, Philos. Mag. B **37,** 469 (1977).

[1.24]F.J. Demond, G. Muller, H. Damjantschitsch, H. Mannsperger, S. Kalbitzer, P.G. LeComber, and W.E. Spear, J. Physique **42,** C4 (1981).

[1.25]R. Messier and R.C. Ross, J. Appl. Phys. **53,** 6220 (1982).

[1.26]D.E. Carlson, R.W. Smith, C.W. Magee, and P.J. Zanzucchi, Philos. Mag. B **45,** 51 (1982).

[1.27]T. Ichimura, Y. Uchida, and O. Nabeta, "Ext. Abstr. Electrochem. Soc. Meet.", **80-2,** 1423 (1980).

[1.28]A. Madan, P.G. LeComber, and W.E. Spear, J. Non-Cryst. Solids **20,** 239 (1972).

[1.29]M.H. Brodsky, R.S. Title, K. Weiser, and G.D. Pettit, Phys. Rev. B **1,** 2632 (1970).

[1.30]J.J. Hauser, Solid State Commun. **19,** 1049 (1976).

[1.31]W.B. Jackson and M.J. Thomson, Physica B 2 C **117,118,** 883 (1983).

[1.32]E.C. Freeman and W. Paul, Phys. Rev. B **20,** 716 (1979).

FIGURES

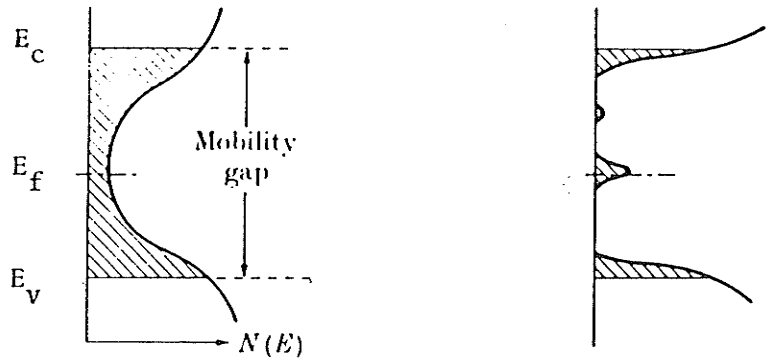

Fig. 1.1 The CFO Model, (a), and the Davis-Mott Model, (b), proposed for the density of states in amorphous semiconductors. (a) Overlapping conduction and valence band tails. (b) Non-overlapping band tails but with a band of defect levels near midgap. Localized states are shown shaded.

CHAPTER 2

OPTICAL AND ELECTRONIC PROPERTIES OF AMORPHOUS SiN_x:H ALLOY FILMS

It is well known that hydrogenated amorphous silicon has a low density of gap states because the hydrogen atoms act as effective dangling-bond terminators. Nitrogen atoms can also be incorporated into the tetrahedral network of silicon as readily as hydrogen atoms, and naturally one would expect that nitrogen atoms may also act as effective dangling-bond terminators. Several investigators[2.1-2.10] have investigated this possibility and reported that the properties of nitrogen-incorporated a-SiN_x films prepared by radio-frequency (rf) glow discharge in SiH_4-N_2-H_2 or in SiH_4-(NH_3 or N_2)-Ar gas mixtures depend upon the composition and the deposition parameters. They are also sensitive to doping impurities such as phosphorus or boron in a manner similar to the behaviour of hydrogenated amorphous silicon. In addition, the SiN_x:H films are highly photosensitive and thus have a potential application for opto-electronic devices. The purpose of this chapter is to describe the effects of the incorporation of nitrogen into amorphous hydrogenated silicon films in regards to the opto-electronic properties of these films.

2.1 Experimental Methods and Characterization

The a-SiN_x:H films were fabricated by rf glow discharge in SiH_4-N_2-H_2 gas mixtures and deposited on glass substrates. The substrate temperature during deposition was 250°C, the chamber pressure was 1 - 2.5 Torr, and the rf power density, defined as the rf power absorbed per unit target electrode area was from 0.1 to 1 W-cm^{-2}. The film thicknesses were in the range 0.8-1.5 μm. The details of the deposition parameters were reported earlier[2.1,2.2].

The refractive index n, and the extinction coefficient k, were measured over the photon energy range of 0.5 - 3.5 eV using spectrally resolved ellipsometric techniques reported previously[2.11]. For the electrical measurements, a gap-cell configuration with aluminum electrodes was adopted, the electrode width being 2.0 mm and the separation between electrodes being 2.5 mm. The photoconductivity was measured using a phase-sensitive detection technique; optical illumination from the monochromator was chopped mechanically and a reference signal was provided to a lock-in amplifier to increase the signal-to-noise ratio. The dark conductivity was measured using a Keithley 602 electrometer.

The concentrations of nitrogen and hydrogen in the a-SiN_x:H films were estimated from the IR absorption data. The films exhibited clearly the IR absorption bands with three peaks at 2100, 840, and 640 cm^{-1}. The two absorption bands at 2100 and 640 cm^{-1} are related to the vibrational mode of the Si-H bonds, and the absorption band at 840 cm^{-1} to the vibration mode of the Si-N bonds. The hydrogen concentration was estimated from the following equation:

$$[Si-H] = C \int \frac{\alpha(\tau)}{\tau} d\tau \quad , \tag{2.1}$$

where $\alpha(\tau)$ is the absorption coefficient of the film at the wavenumber τ and C is a constant. The values of C used for the estimation were 1.4×10^{20} and 1.6×10^{19} cm^{-2} based on the absorption intensities for the absorption bands at 2100 and 640 cm^{-1}, respectively; they were assumed to be independent of the composition x[2.12]. According to Shanks et al.[2.13], the 640-cm^{-1} band provides a truer scale for the H content than the 2100-cm^{-1} band, the results being presented here were based on the 640-cm^{-1} band. The concentration in terms of the atomic percentage was calculated on the basis of the atomic density of crystalline Si, which is 5×10^{22} cm^{-3}. The nitrogen concentration (840-cm^{-1} band) was estimated using the same method. The data obtained from Si wafers implanted with nitrogen were used as a calibration for the estimation of the nitrogen content in our a-SiN_x:H films. These measurements were confirmed by Auger electron spectroscopy (AES).

The composition x, which is the atomic percentage ratio of N:Si in the a-SiN_x:H films, increases with the increasing molar ratio of N_2 to SiH_4 in the reaction SiH_4-N_2-H_2 gas phase as shown in Fig. 2.1. The addition of a small amount of B_2H_6 to the gas mixture does not change the nitrogen content in these films, but the increase in nitrogen content appears to cause a slight decrease in hydrogen content, at least for films with a high nitrogen content. In all the a-SiN_x:H films under investigation, the hydrogen content decreases from 14 to 8% as the nitrogen content x increases from 0.1 to 0.6. The data in Fig. 2.1 were the average values of two to four measurements for each point.

2.2 Discussion of Optical Measurements

The dependence of n and α upon photon energy is shown in Figs. 2.2 and 2.3 where the N_2/SiH_4 mole fraction in the gas phase was the experimental parameter. For convenience the conversion to N/Si, as given in Fig. 2.1, has been made in Figs. 2.2 and 2.3. The absorption coefficient α can be related to the extinction coefficient k by

$$\alpha = 4\pi k/\lambda \quad . \tag{2.2}$$

For parabolic bands the optical energy gap E_{opt} can be related to α by

$$\alpha h\nu = B(h\nu - E_{opt})^2 \quad , \tag{2.3}$$

where B is a constant. The value of α as a function of exciting photon energy for various compositions is shown in Fig. 2.3. The plot of $(\alpha h\nu)^{1/2}$ as a function of $h\nu$ fits Eqn(2.3) well in the regions near the mobility edges of the bands as shown in Fig. 2.4, indicating that these regions are reasonably parabolic. The extrapolation of the parabolic portion to the zero absorption axis yields E_{opt}. The value of E_{opt} as a function of x is shown in Fig. 2.5. E_{opt} is about 1.65 eV and remains practically independent of x for $0.1 < x < 0.4$, but it increases with increasing x for $x < 0.1$ and $x > 0.4$. A plot of the refractive index n at photon energy $h\nu = 0.5$ eV is presented in Fig. 2.6. We observe that for nitrogen content well above that required for the increase in E_{opt} of Fig. 2.5, n approaches the value for amorphous silicon nitride (Si_3N_4) [2.15]. The interpretation of the conductivity data in the next section also

leads to the conclusion that for the highest N_2/SiH_4 ratios during fabrication, the film becomes Si_3N_4, which is an excellent insulator. These results indicate that the behaviour of nitrogen atoms in a-SiN_x:H films is similar to that of hydrogen atoms in a-Si:H films for x below a threshold concentration of about 0.4. It should be noted that E_{opt} is about 1.55 eV for x = 0. The slightly low value of E_{opt} may be associated with the measuring technique used to determine E_{opt}. It has been our experience that ellipsometric results have consistently yielded lower values for E_{opt} ($\sim 10\%$) as compared with values obtained from spectrophotometry. Since ellipsometry is more of a surface measurement as compared with spectrophotometry, this difference in E_{opt} may be due to desorption of atomic hydrogen and/or adsorption of other contaminants on the film surface. Comparisons are made in a relative manner and as such this discrepancy represents no major difficulty. As compared with spectrophotometry, it is our experience that the relative error between data points is smaller for ellipsometric measurements.

In Eqn(2.3), the parameter B is also a useful diagnostic of the material, since it is inversely proportional to the extent ΔE of the tail states at the conduction and valence band edges. It has been shown that[2.16]

$$B \approx \pi^2 \sigma_0 (n_1 C \Delta E)^{-1} \quad ,$$

where σ_0 is the minimum metallic conductivity, n_1 is the long wavelength refractive index, and C is the velocity of light. The parameter B obtained from optical data is shown in Fig. 2.7. These results indicate that the extent of the tail states in a-SiN_x:H

films increases with N content x. Figs. 2.3 and 2.7 indicate that the incorporation of nitrogen atoms increase the density of shallow localized states. This is further supported by the observation of an increasing time constant associated with the photoresponse in the long wavelength region as x increases.

2.3 Discussion of Electrical Measurements

Fig. 2.8 shows the dependence of the dark conductivity σ_d and photoconductivity σ_{ph} on x. Below the threshold concentration of x = 0.4, σ_d increases with x. Above this threshold, a rapid increase in E_{opt} ocurrs and films tend to become Si_3N_4 as mentioned earlier. The films are of good electronic grade as evidenced by the ratio of σ_{ph}/σ_d of about 10^4 for a photon flux of 5×10^{15} photons-cm^{-2}-s^{-1} at λ = 632.8 nm. The ratio of photoconductivity to darkconductivity is weakly dependent on nitrogen content, though both σ_{ph} and σ_d depend strongly on both boron and phosphorus doping[2.2]. Based on the dependence of conductivity with boron and phosphorus doping, the undoped a-SiN_x:H films are n-type with the Fermi level located about 0.65 eV below the electron-mobility edge (shown later in this chapter). Boron doping tends to change the films from n-type to p-type, thus an optimal amount of boron doping may make the films completely compensated with the Fermi level located at the middle of the mobility gap where σ_d becomes a minimum. Under this condition the ratio of σ_{ph}/σ_d can reach a value of 10^6[2.2]. This property of boron-doped a-SiN_x:H films is particularly interesting because they can be used for opto-electronic devices.

The temperature dependence of the dark conductivity (Fig. 2.9) may be understood on the basis of earlier treatments of a-Si:H thin films[2.17], with some modifications to take into account the effects of nitrogen incorporation. We describe the dark conductivity by

$$\sigma_d = \sigma_1 \exp(-\frac{E_1}{kT}) + \sigma_2 \exp(-\frac{E_2}{kT}) + \sigma_3 \exp(-\frac{C_3}{T^{1/4}}) \quad , \tag{2.4}$$

where the first term is due to conduction in extended states. This is known, on the basis of dependence on B and P doping, to be electron conduction in these undoped films[2.2]. Thus we have

$$E_1 = E_c - E_f \quad , \tag{2.5}$$

where E_c is the mobility edge in the conduction band of the a-SiN_x:H films and E_f is the energy of the Fermi level in darkness. Following Nagels[2.17], we have also that

$$\sigma_1 = e \ \mu_0 N_c \ \exp(\gamma / k) \quad , \tag{2.6}$$

where μ_0 is the mobility in the extended states, N_c is their effective density (taken at E_c), and γ is the temperature coefficient of the energy gap and k is Boltzmann's constant.

The second term in Eqn(2.4) represents electron transport in the band tails below E_c, and the third term is due to variable-range hopping conduction at the Fermi level. The latter process may be further interpreted using the model of

Mott[2.18] by writing

$$C_3 = \left(\frac{18\lambda^3}{k\ N(E_f)}\right)^{1/4} , \qquad (2.7)$$

where λ is the decay rate of the localized wave functions, and $N(E_f)$ is the density of localized states at the Fermi level.

It should be noted that σ_3 in Eqn(2.4) can also be expressed in an analytical form containing λ and $N(E_f)$, in which case it varies as $(N(E_f)/T)^{1/2}$. In general, however, this leads to unrealistic values for these quantities; several earlier workers have attributed this to an uncertainty in the appropriate expression for σ_3[2.19,2.20]. Even with this uncertainty, however, σ_3 is expected to increase approximately as $N(E_f)^{1/2}$.

Based on the dependence of σ_d upon T in the high temperature range, we have found that $E_c - E_f \simeq$ 0.62 - 0.65 eV, independent of nitrogen content, provided that it does not exceed the threshold concentration N/Si $\simeq$ 0.4 discussed above. Fig. 2.10 shows that σ_1 increases by a factor of $\simeq$ 10, as the nitrogen content x increases from 0 to approximately 0.3, then decreases with further increases in x.

Equation (2.6) implies the assumption that electron transport is dominant over hole transport for the undoped material, an assumption which has been verified for the same material by introducing dopants[2.2]. If we further assume that N_c is not greatly affected by the nitrogen content x for the small values of x during which σ_1 increases, we may interpret Fig. 2.10 as an increased mobility by the same factor of

$\simeq$ 10 due to the nitrogen incorporation. The constancy of N_c is consistent with the independence of the refractive index with composition shown in Fig. 2.6. Finally, the increase in σ_1 is very much larger than any effects arising from an uncertainty in the activation energies E_1, as is evident from the high-temperature region in Fig. 2.9.

In the intermediate temperature range, we have attempted to obtain σ_2 and E_2 in Eqn(2.4) from the experimental data. Once we remove the contributions from the first term in Eqn(2.4), which represents extended-state conduction, the current which remains is well described by the $\exp(-C_3/T^{1/4})$ dependence of the third term. In other words, the contributions from the second term in Eqn(2.4), which represents band tail conduction, are too small to be resolved in the dark conductivity data. We therefore assume that the transport is dominated by extended-state conduction at high temperature and hopping at the Fermi level at lower temperatures.

Fig. 2.11 shows the conductivity in the low temperature region, plotted to bring out the correspondence with the third term in Eqn(2.4). Since there is a $T^{-1/2}$ dependence in σ_3[2.18], we expect a linear relation between $\log(\sigma T^{1/2})$ and $(T_0/T)^{1/4}$ in this region. On the basis of these results, and adopting a value for λ of 10^7 cm^{-1} (a 10 A radius for the localized wave functions), we obtain, using Eqn(2.7), an estimation of the density of states at the Fermi level of $N(E_f) \simeq 1.1 \times 10^{17}$ $cm^{-3}eV^{-1}$. Furthermore $N(E_f)$ appears to increase very modestly with N concentration.

2.4 Effects of Annealing

Unlike crystalline materials, amorphous materials have many different electronic structures, each of which may have its own minimum equilibrium potential energy. This may be why the properties of amorphous semiconductor films are dependent on the deposition parameters, thermal and optical history. In fact, all amorphous semiconductor films exhibit a strong annealing effect. By annealing the film samples (fabricated at the substrate temperature of 250°C) at 450°C for 10 minutes and then allowing them to cool down slowly to room temperature, the values of n, α, and σ_d are changed, implying that the films under this condition have settled into another quasi-stable structure. Some typical results are shown in Fig. 2.12. Both α and σ_d have increased after annealing. This is probably due to hydrogen being driven off and some unsatisfied dangling bonds are being restored. A reduction of hydrogen content would result in a decrease in E_{opt} and hence an increase in α. In addition to the reduction of hydrogen, a possibility exists that the nitrogen content of the films is also being reduced by annealing. Fig. 2.8 shows that for $x > 0.3$ a reduction in nitrogen content would increase σ_d. Also if nitrogen is driven off, α would increase as shown in Fig. 2.4. Regarding the decrease of n with annealing, Fig. 2.2 indicates that for $x < 0.64$ a reduction in nitrogen would increase n, contrary to what is observed after annealing. This leads us to believe that the amount of nitrogen being driven off after annealing is negligible. This implies that the dominant factor for the increase in α and σ_d is hydrogen evolution. It is also possible that the elevated temperatures may also play a role in enhancing the

formation of a Si_3N_4 network, resulting in a reduction in n. Fig. 2.2 shows that as composition x increases, n decreases and approaches that of Si_3N_4. Annealing effects in a-SiN_x:H films have also been reported by other investigators[2.21].

2.5 Conclusions

On the basis of the optical and electrical measurements of undoped amorphous SiN_x:H films presented in this chapter and the above discussion we may conclude, at least for films prepared by radio-frequency glow-discharge in a SiH_4-N_2-H_2 ambient, that:

(1) Nitrogen does not act as a donor impurity since the activation energy for extended state conduction is unchanged for $0 < x < 0.4$. The optical gap, approximately 1.65 eV, is also approximately constant in this range of x.

(2) The electron mobility for conduction in the extended states may be improved by nitrogen incorporation.

(3) The density of states at the Fermi energy (in the upper part of the bandgap) is approximately independent of nitrogen content, at least for $x \leq 0.3$.

(4) The extent of the tail states increases with the degree of nitrogen incorporation, but conduction in these states provides at most a minor contribution to the total current.

(5) There is a precipitous conversion from the tetrahedral structure to Si_3N_4 above $x = 0.4$. Below this nitrogen content we may regard a-SiN_x:H as a material similar to a-Si:H with the differences outlined above.

References

[2.1] H. Watanabe, K. Katoh, and M. Yasui, Japan J. Appl. Phys. **21,** L341 (1982).

[2.2] H. Watanabe, K. Katoh, and M. Yasui, Thin Solid Films **106,** 263 (1983).

[2.3] H. Watanabe, K. Katoh, M. Yasui, and Y. Shibata, Proc. 10th Int. Conf. on Amorphous and Liquid Semiconductors, Tokyo, Japan, Aug. 22-26, (1983).

[2.4] H. Watanabe, K. Katoh, and M. Yasui, to be published in Japan. J. Appl. Phys. **23(1),** (1984).

[2.5] J. Baixeras, D. Mencaraglia, and P. Andro, Philos. Mag. **37,** 403 (1978).

[2.6] R.W. Griffith, F.J. Kampas, P.E. Vanier, and M.D. Hirsch, J. Non-Cryst. Solids **35,36,** 391 (1980).

[2.7] W.Y. Xu, Z.L. Sun, Z.P. Wang, and D.L. Lee, J. de Phys. **C4,** supp. 10, 695 (1981).

[2.8] S.M. Pietruszko, K.L. Narasimhan, and S. Guha, Philos. Mag. **43,** 357 (1981).

[2.9] H. Kurata, M. Hirose, and Y. Osaka, Japan J. Appl. Phys. **20,** L811 (1981).

[2.10]T. Noguchi, S. Usui, A. Sawada, Y. Kanoh, and M. Kikuchi, Japan J. Appl. Phys. **21,** L485 (1982).

[2.11]K.C. Kao, R.D. McLeod, C.H. Leung, H.C. Card, and H. Watanabe, J. Phys. D: Appl. Phys. **16,** 1801 (1983).

[2.12]C.J. Fang, K.J. Gruntz, L. Ley, M. Cardona, F.J. Demond, G. Muller, and S. Kalbitzer, J. Non-Cryst. Solids **35,36,** 255 (1980).

[2.13]H. Shanks, C.J. Fang, L. Ley, M. Cardona, and S. Kalbitzer, Phys. Status Solidi B **100,** 43 (1980).

[2.14]J. Tauc, in "The Optical Properties of Solids", F. Abeles Ed., (North-Holland, Amsterdam, 1970) p. 277.

[2.15]S.M. Sze, "Physics of Semiconductor Devices", 2nd Edition, (Wiley, New York, 1981) p. 852.

[2.16]E.A. Davis and N.F. Mott, Philos. Mag. **22,** 903 (1970).

[2.17]P. Nagels, in "Amorphous Semiconductors", M. Brodsky Ed., (Springer, New York, 1979) p. 123.

[2.18]N.F. Mott, Philos. Mag. **19,** 835 (1969).

[2.19]S.K. Bahl and S.M. Bhagat, J. Non-Cryst. Solids **17,** 409 (1975).

[2.20]D.K. Paul and S.S. Mitra, Phys. Rev. Lett. **31,** 1000 (1973).

[2.21]G. Sasaki, M. Kondo, S. Fujita, and S. Sasaki, Japan J. Appl. Phys. **21,** 1394 (1982).

FIGURES

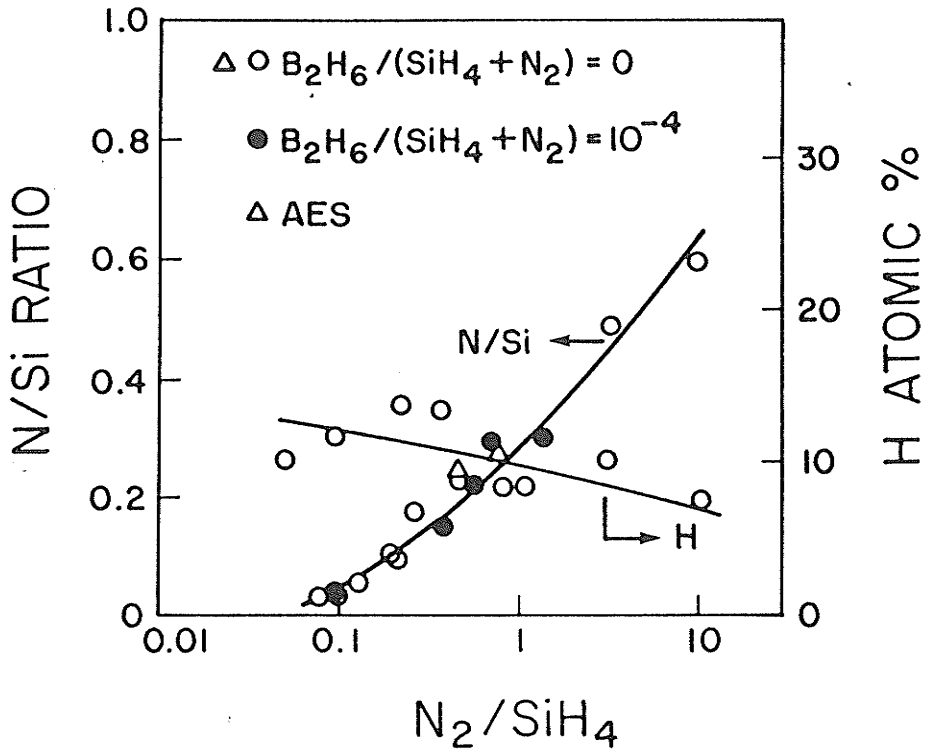

Fig. 2.1 Nitrogen-to-silicon atomic-percentage ratio and hydrogen atomic percentage as functions of molar ratio of N_2 to SiH_4 in the gas phase.

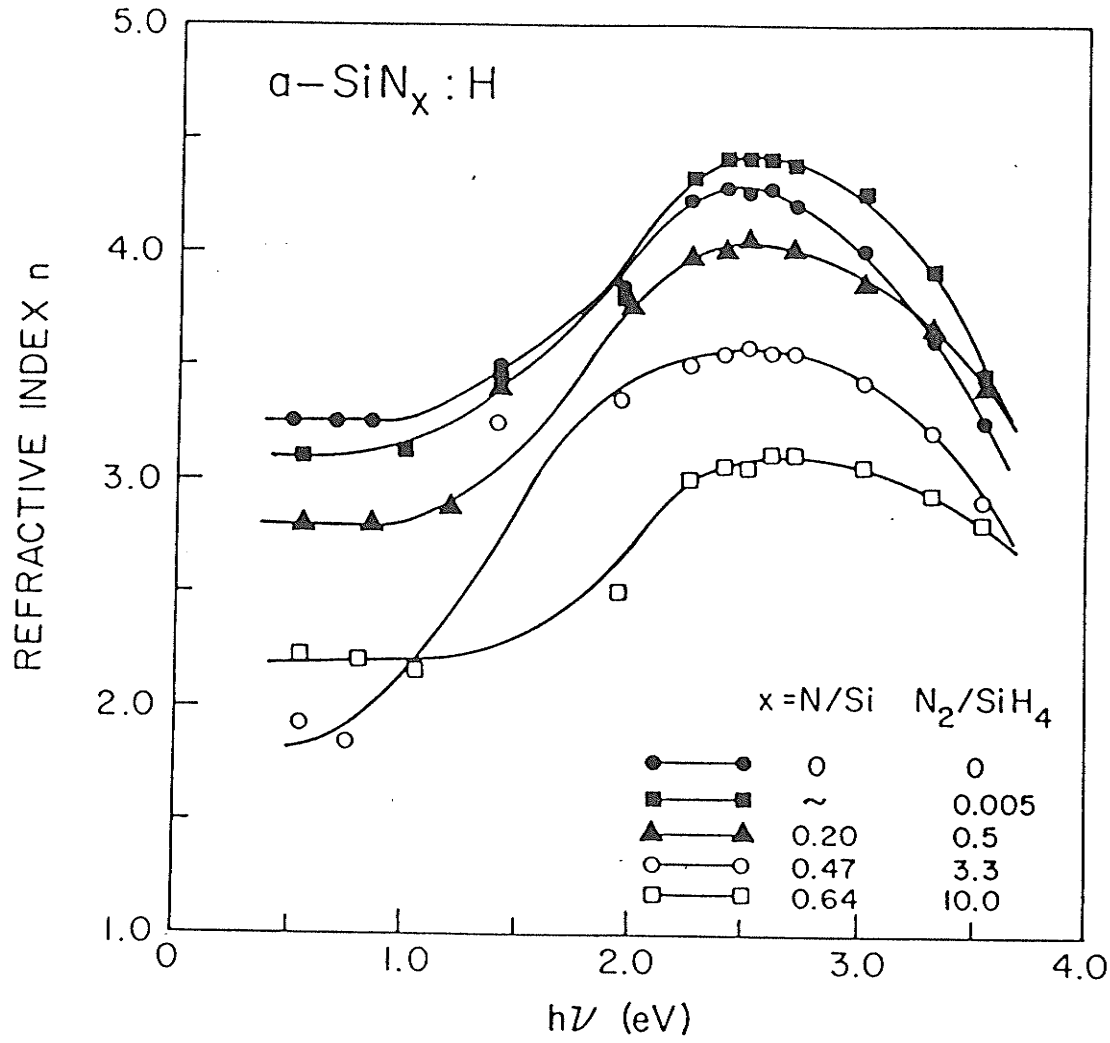

Fig. 2.2 Refractive index vs photon energy for undoped a-SiN$_x$:H films, with composition x (N/Si ratio) as a parameter. ($0 \leq x \leq 0.64$)

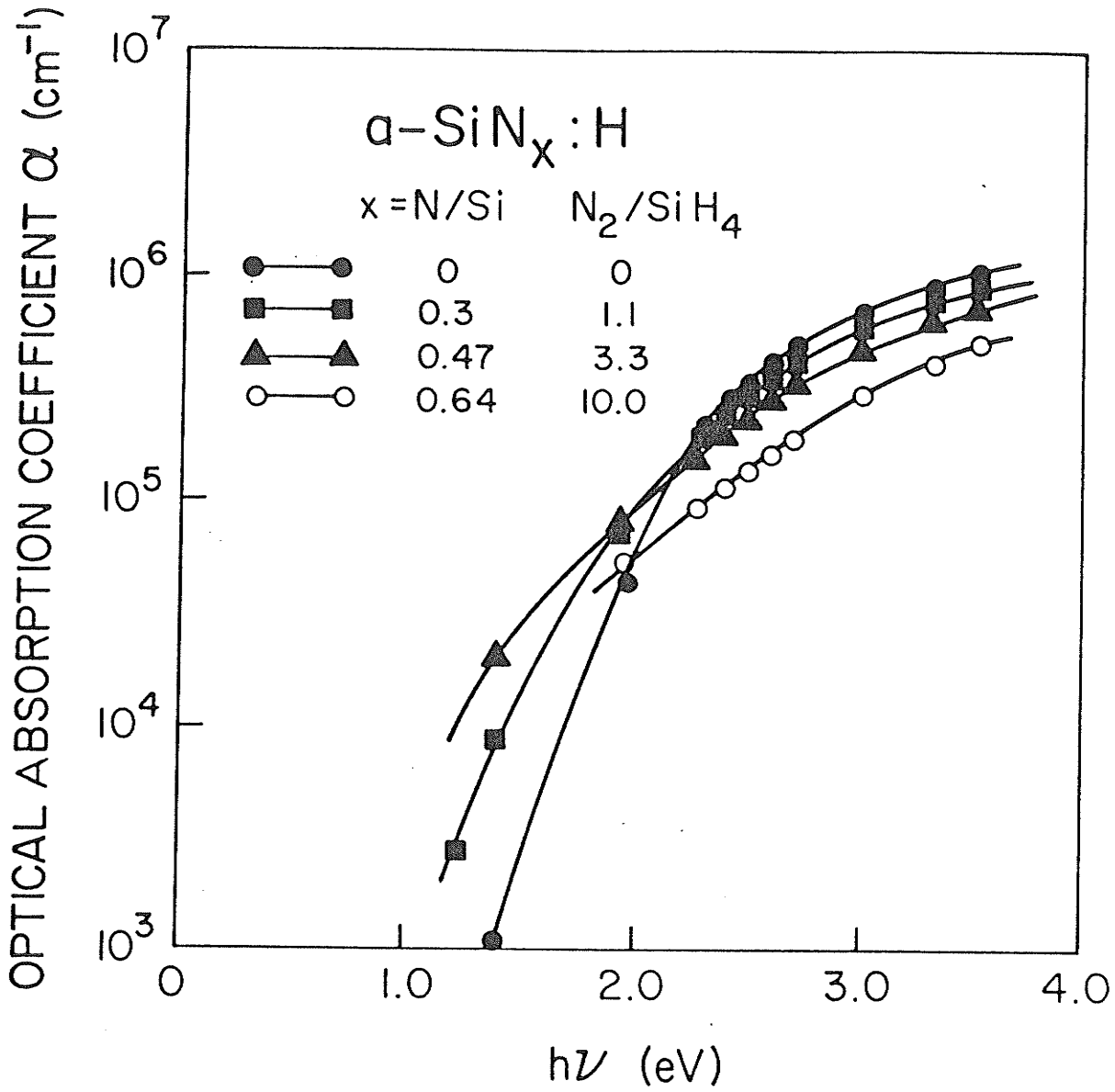

Fig. 2.3 Optical absorption coefficient vs photon energy for undoped a-SiN$_x$:H films with nitrogen content x as a parameter. ($0 \leq x \leq 0.64$)

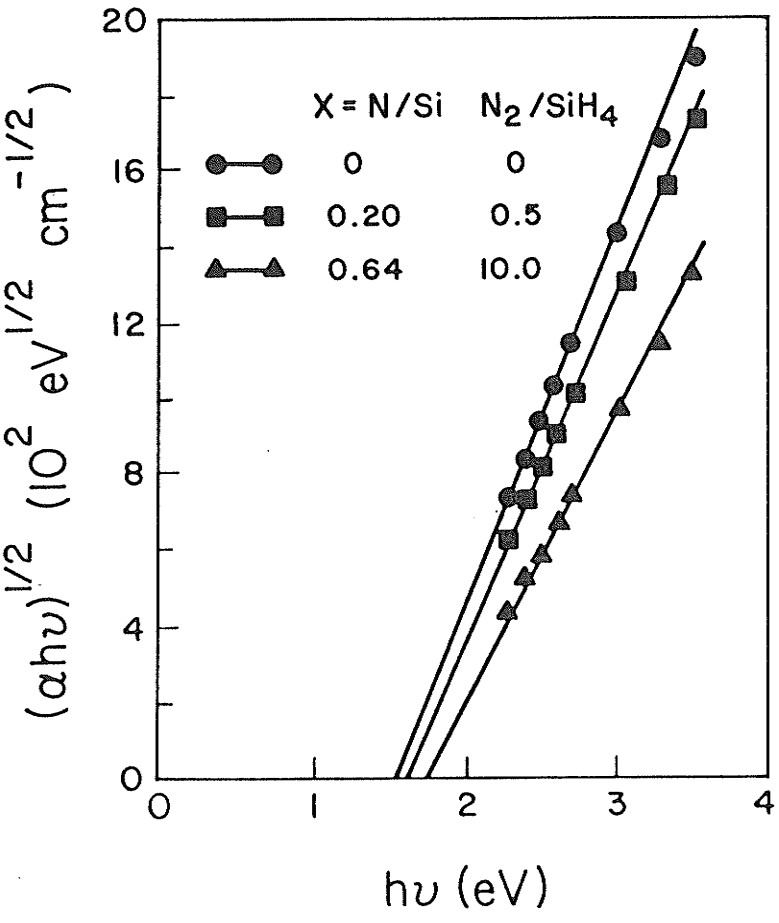

Fig. 2.4 The value of $(\alpha h\nu)^{1/2}$ as a function of exciting-photon energy (only a few are shown for clarity).

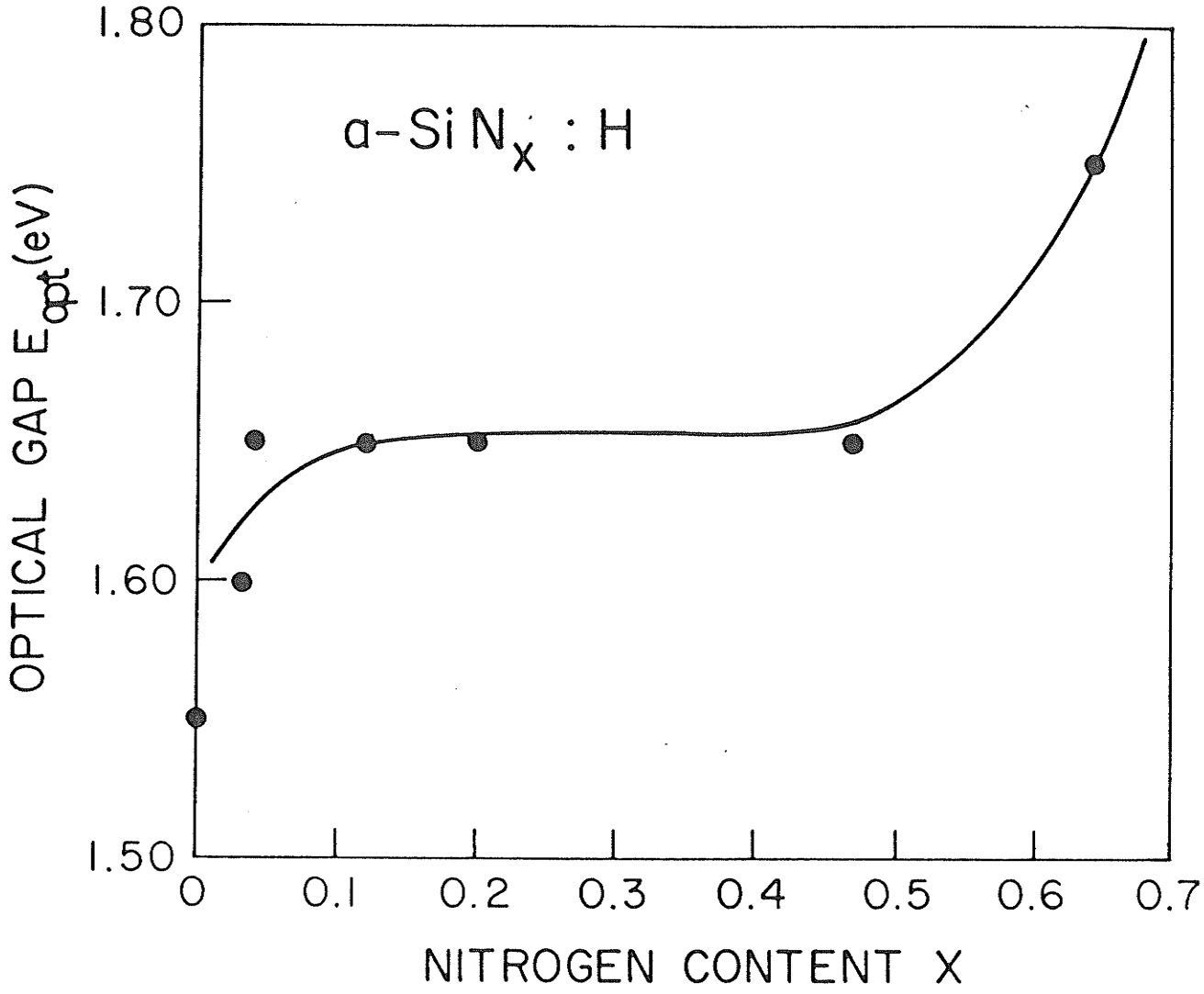

Fig. 2.5 Optical energy gap of undoped a-SiN$_x$:H films with nitrogen content x as a parameter.

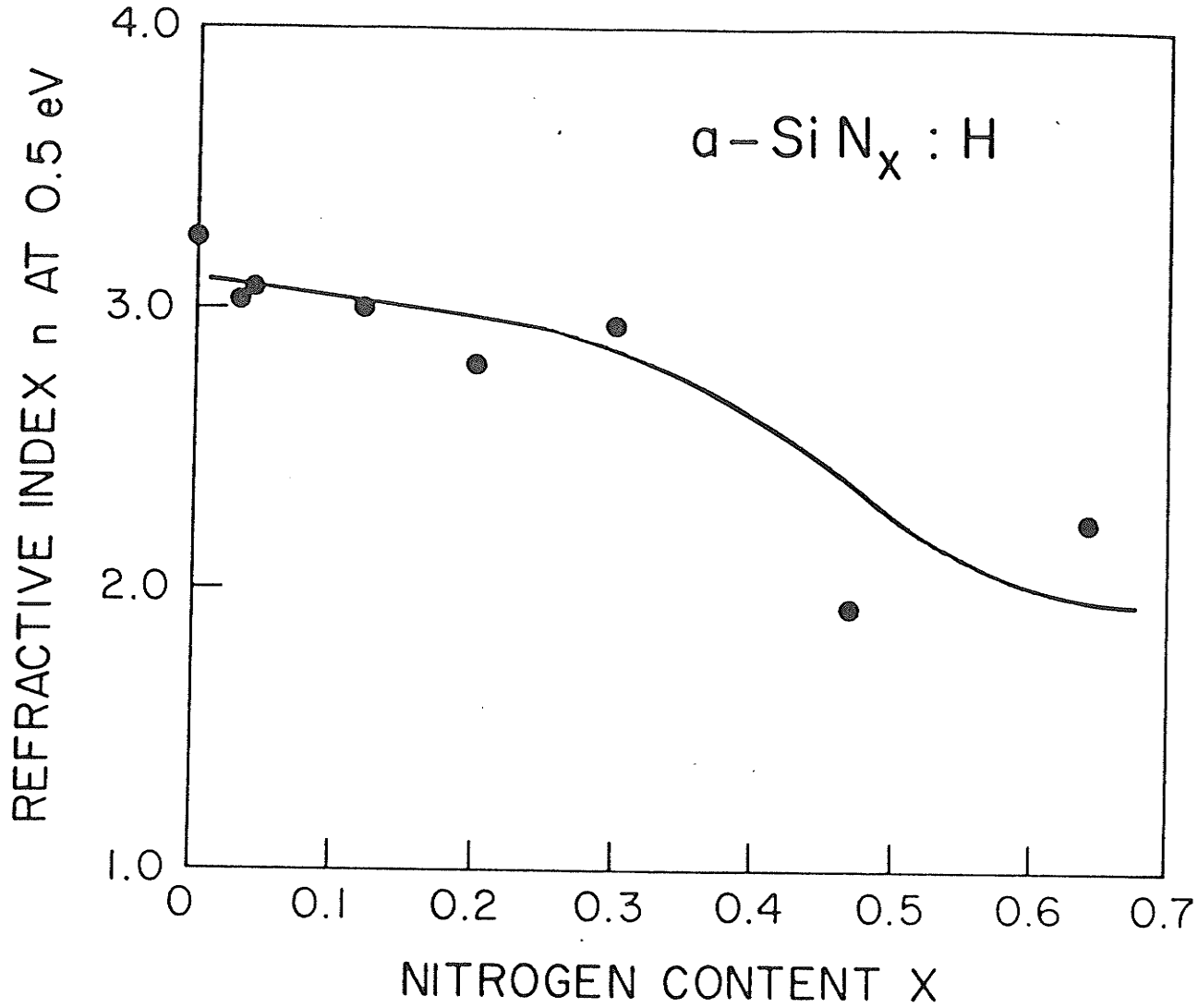

Fig. 2.6 Refractive index at $h\nu = 0.5$ eV of a-SiN$_x$:H films vs nitrogen content.

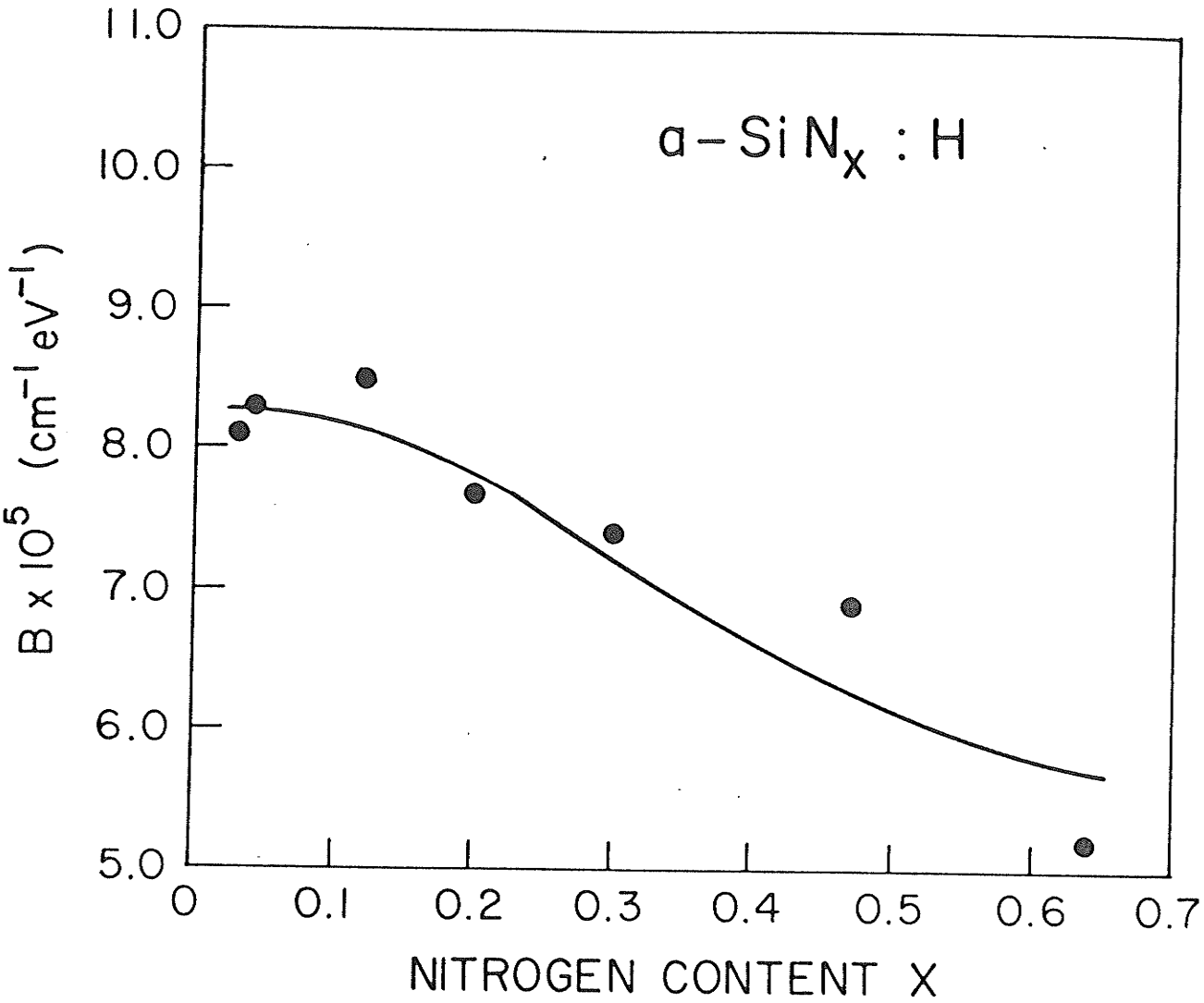

Fig. 2.7 The B-parameter in $\alpha h\nu = B(h\nu - E_{opt})^2$ vs nitrogen content x for a-SiN_x:H films. $B \sim (\Delta E)^{-1}$ where ΔE is the extent of the tail states.

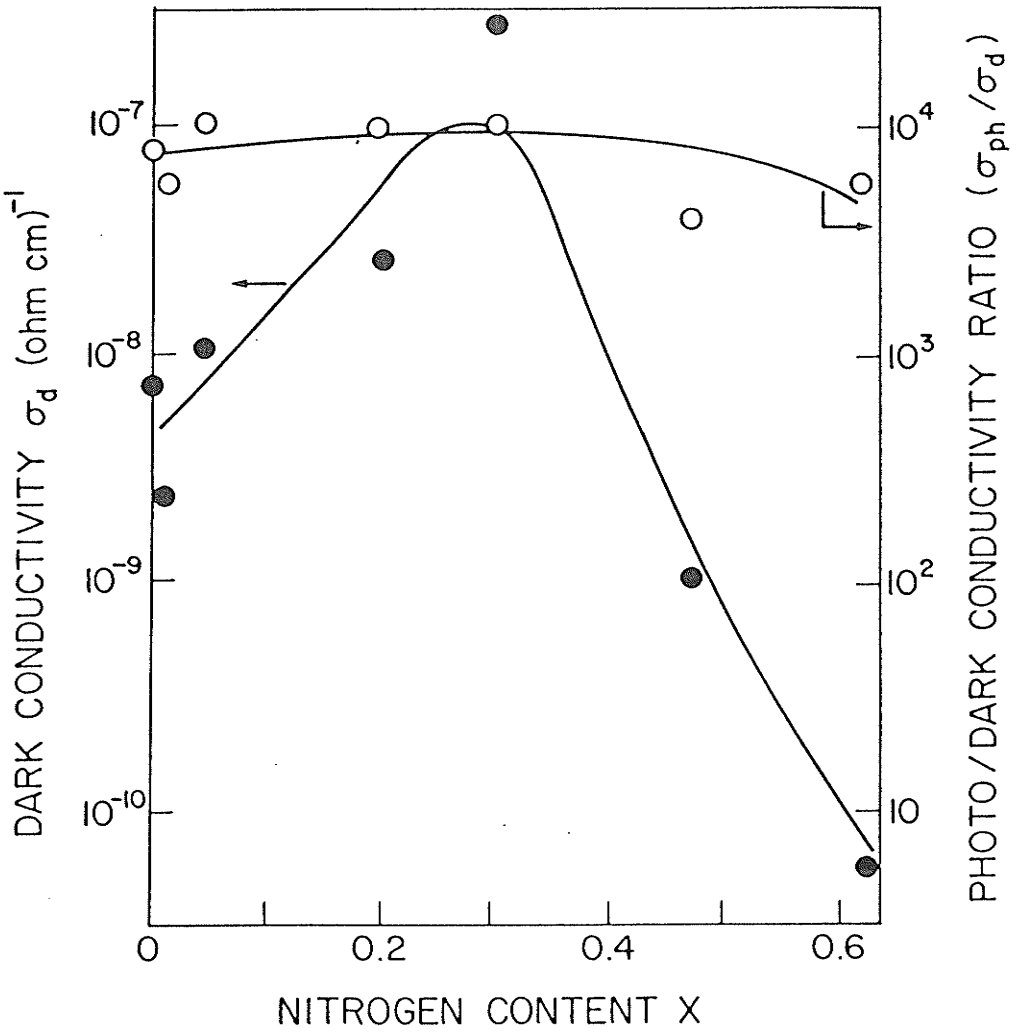

Fig. 2.8 Dark conductivity, σ_d, photoconductivity, σ_{ph}, and σ_{ph}/σ_d as functions of x for a-SiN$_x$:H films at room temperature (photon flux: 5×10^{15} photons-s^{-1}-cm^{-2} at λ = 632.8 nm).

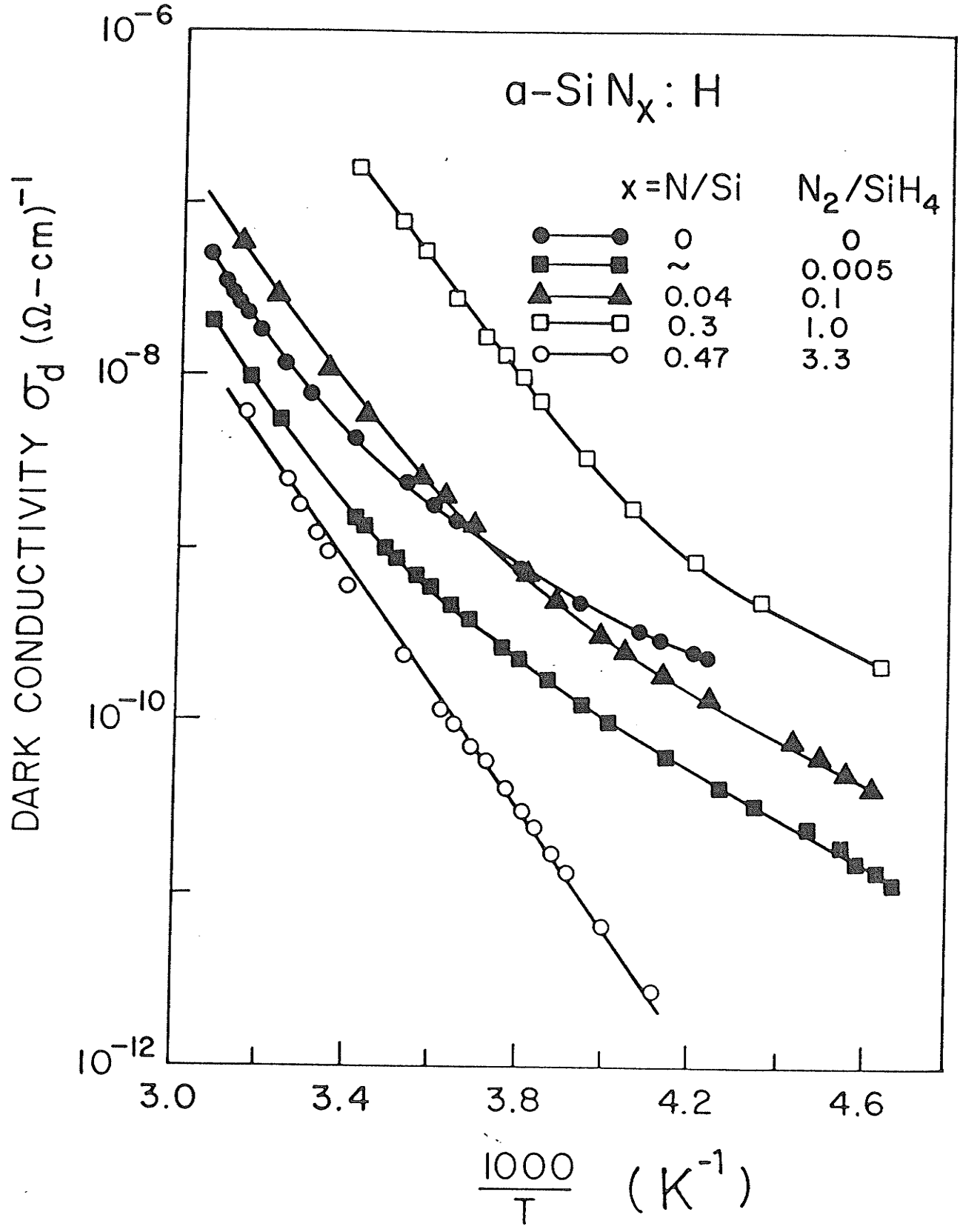

Fig. 2.9 **Dark conductivity vs temperature for undoped a-SiN$_x$:H films with nitrogen content x as a parameter.**

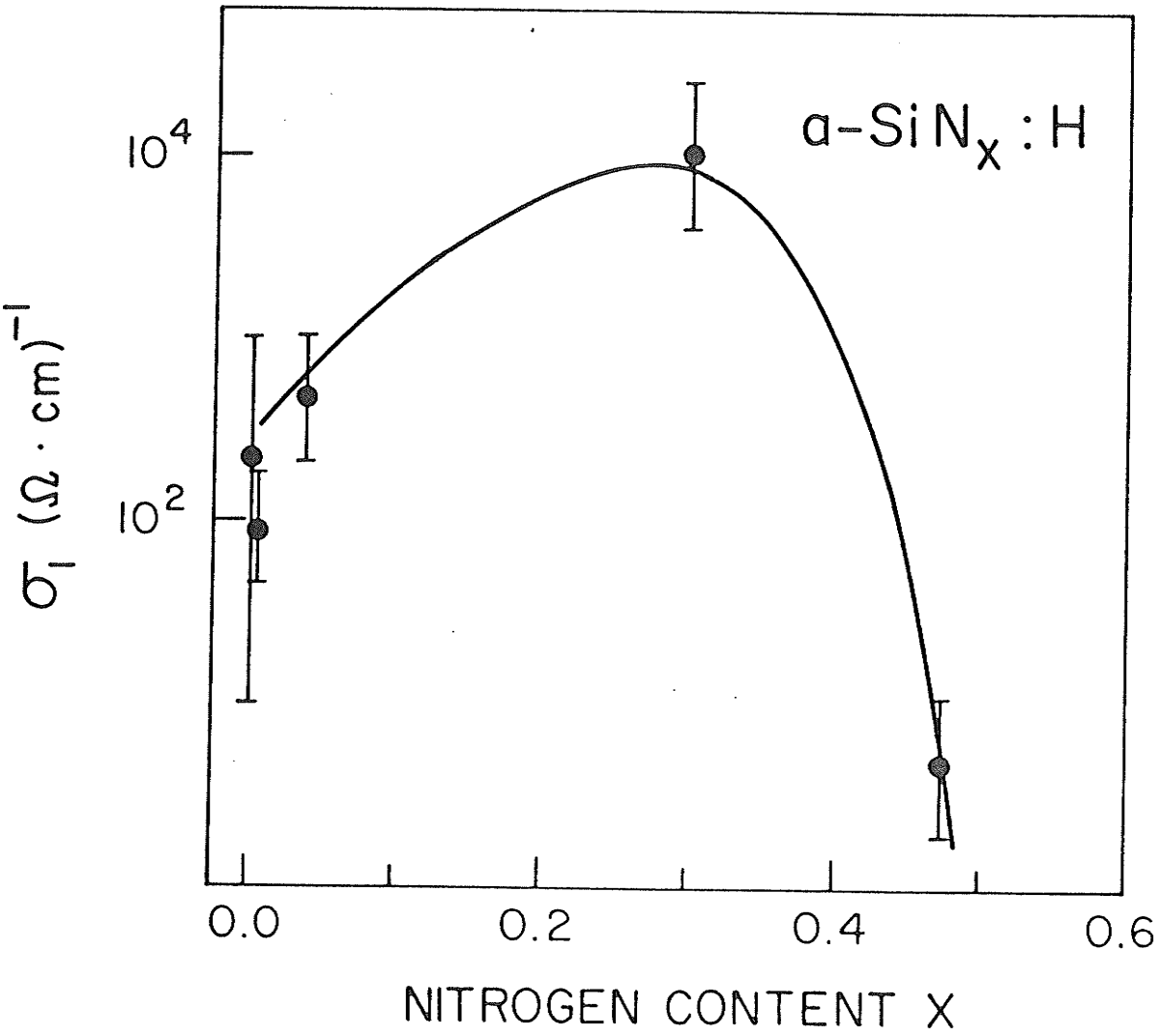

Fig. 2.10 Conductivity parameter σ_1 for extended-state conduction in first term of Eqn. (2.4), determined from experiment at high temperature, assuming $\sigma_d = \sigma_1 \exp(-E_1/kT)$.

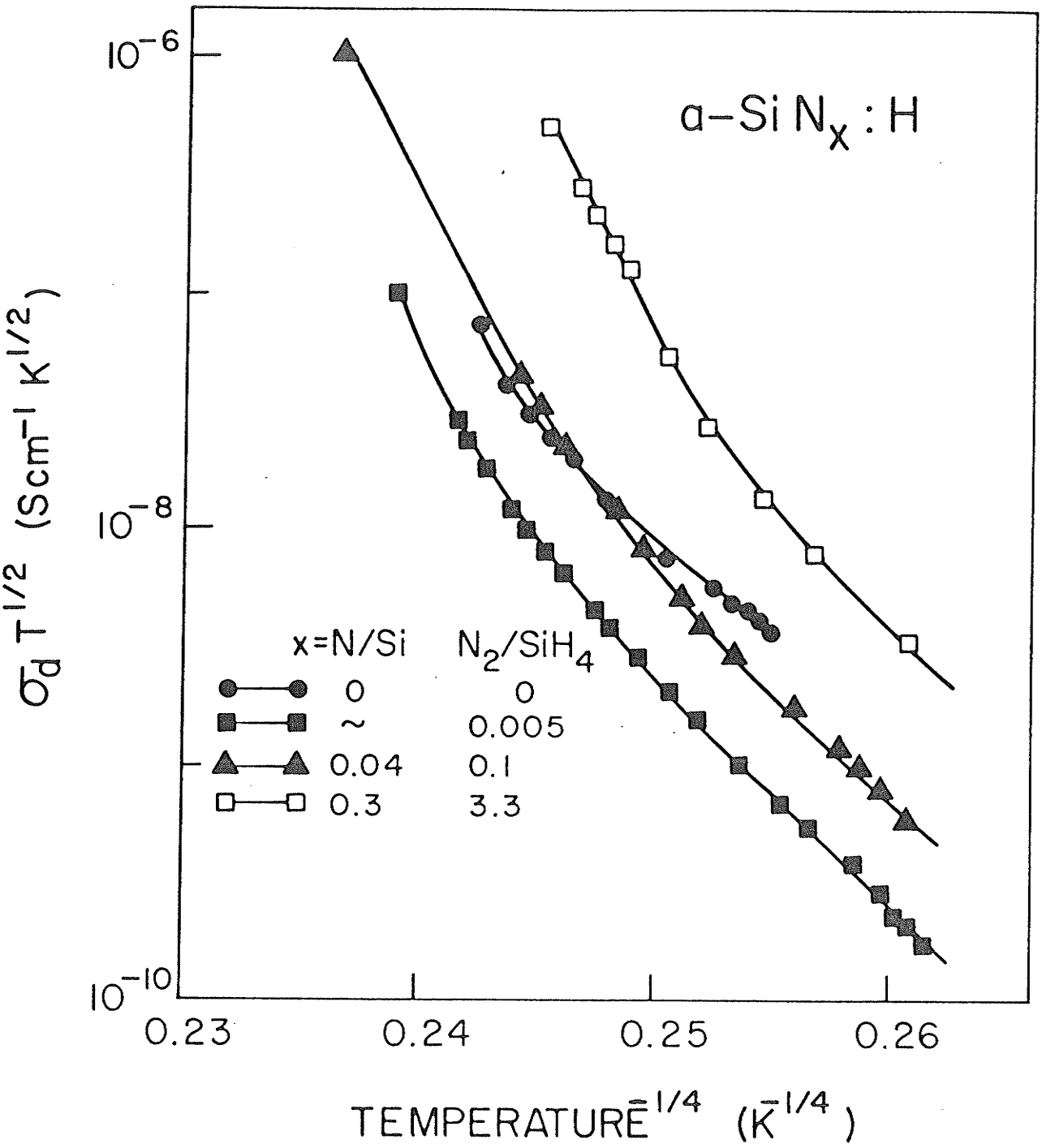

Fig. 2.11 Conductivity in low-temperature region interpreted according to Mott's model of variable range hopping at E_f. Plotted as $\log(\sigma T^{1/2})$ vs $T^{-1/4}$ for comparison with theory.

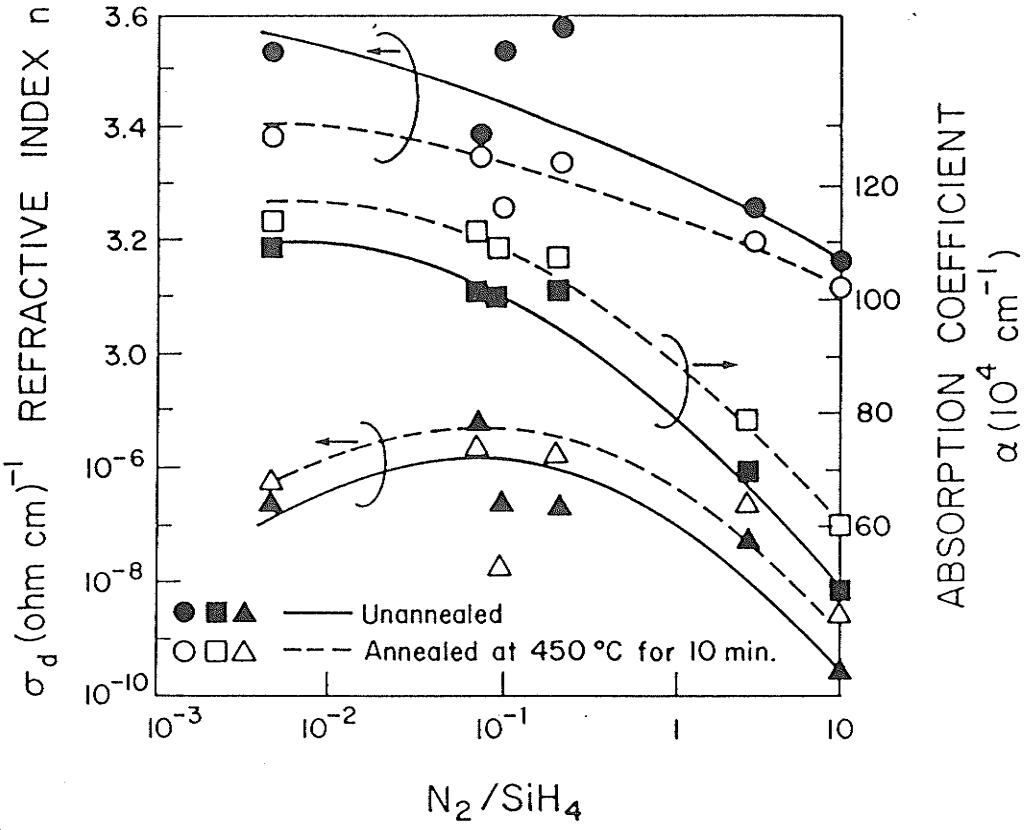

Fig. 2.12 Effects of annealing at 450°C for 10 minutes on n, α, and σ_d for a-SiN_x:H films measured at room temperature, and n and α at photon energy of 3.5 eV.

Chapter 3

AMORPHOUS AND MICROCRYSTALLINE SILICON FILMS FROM MICROWAVE PLASMAS: OPTICAL PROPERTIES AND THEIR RELATION TO STRUCTURE

Considerable interest has arisen in hydrogenated microcrystalline silicon (μc-Si:H) due to its high electrical conductivity and mobility, high doping efficiency and lower optical absorption as compared to hydrogenated amorphous silicon. Various workers have reported on the electrical, optical and structural properties of μc-Si:H [3.1-3.14]. The preparation techniques of thin films of μc-Si:H include chemical transport[3.2] and reactive sputtering in a hydrogen atmosphere[3.3,3.4]. In addition, Saito et al. [3.5] have reported μc-Si:H prepared by rf sputtering in various atmospheres, achieving high deposition rates in Kr and Ar ambients. Nishida et al.[3.6] have reported high conductivity and a wide band gap (2.2 eV) for μc-Si:F:H deposited by photo-CVD.

The role of hydrogen[3.7,3.8], the growth kinetics[3.9,3.10], and the effects of doping[3.6,3.10,3.11] on μc-Si:H have also been reported. Phosphorus-doped μc-Si:H has been proposed as a suitable material for a window layer for solar cell applications due to its low absorption but also its desirable refractive index, which results in reduced reflection of sunlight[3.11].

We report the first results of the refractive index n, and of the imaginary part of the dielectric constant ϵ_2, for μc-Si:H films deposited by microwave glow

discharge. The material prepared in this system consists of microcrystallites of silicon embedded in an amorphous matrix, and our samples span the range from pure amorphous silicon to high volume fraction microcrystalline silicon[3.15,3.30]. The optical data are correlated with structural data, in particular with the volume fraction of crystallites and their grain sizes as determined from X-ray diffraction measurements. We believe that these results are among the first investigations of the correlation between optical parameters (n and ϵ_2) and structural data in materials of this kind.

3.1 Experimental Details

The a-Si:H and μc-Si:H films were fabricated with a microwave plasma system described earlier[3.15,3.16,3.30]. Briefly, the system consists of a stainless steel waveguide in which the microwave plasma may be confined by an external axial magnetic field. This system can operate at microwave power levels as low as 1 Watt. Microwave power is generated by a magnetron operating in a continuous mode, at a frequency of 2.45 GHz. Substrates can be placed with their surfaces either parallel or normal to the magnetic field vector (the axis of the waveguide). The magnetic field provided by two external coils is on the order of 1000 Guass. A field of 875 Guass at 2.45 GHz establishes electron cyclotron resonance (ECR) enabling power levels and chamber pressure to be substantially reduced while still maintaining a stable plasma. The chamber is terminated by a mesh, sufficiently fine to represent a short circuit to the microwave power, but at the same time sufficiently coarse to

allow for visual observation of the plasma, or for optical emission spectrometry (OES). Gas composition is set and measured by mass flowmeters. An Inficon 200 quadrupole mass spectrometer is used to monitor the gas composition and its dissociation. The plasma is also monitored by real time OES which indicates an absence of oxygen or other contaminants. The deposition system is shown in Fig. 3.1.

Plasma discharge was produced in SiH_4(2%)-H_2(98%) gas mixtures and films were deposited on quartz substrates, with a substrate temperature of 150°C. Substrate surfaces were placed parallel to the axial magnetic field. The total chamber pressure and absorbed microwave power were 0.03-0.10 Torr and 1-10 Watt, respectively. Films were fabricated at magnetic fields levels near the ECR condition.

The refractive index n, and the extinction coefficient k, were measured over the photon energy range 2.0 - 3.5 eV using spectrally resolved ellipsometry[3.17,3.18]. Dark conductivity was measured in a coplanar gap configuration at fields of $\sim$ 600 V cm^{-1}, which was in the ohmic region for all films. Film thickness was measured by a Sloan thickness profiler, with sample thicknesses ranging from $\simeq$ 0.5 to 3.0 μm. Analysis of X-ray diffraction data, employing Cu-Kα (40 KeV, 20 mA) radiation, allowed the calculation of a relative volume fraction of crystallites rf_v, and the crystallite grain size. The crystallite size was determined from the full width at half-maximum (FWHM) of the (111) diffraction peak, using Scherrer's formula[3.19] with a shape factor of 0.89.

3.2 Results and Discussion

X-ray diffraction was measured in the range of scattering angles 2θ = 20 - 60°, with diffraction peaks corresponding to the (111), (220) and (311) planes being observed for μc-Si:H films. Fig. 3.2 shows a few typical X-ray diffraction patterns for various microcrystalline films, whereas films exhibiting no structure in the diffraction pattern were considered to be amorphous. The diffraction peaks at $2\theta \simeq 28.5°$ show that the crystallite size in the (111) orientation is ≃ 200 - 300 A for all films.

The ratio of peak to background intensities (P/B) of the (111) diffraction peak was chosen to characterize the degree of microcrystallinity, where (P/B) - 1 = 0, implies no crystalline structure and hence represents an amorphous film. The volume fraction of microcrystallites is estimated from diffraction lines before and after annealing. Complete thermal crystallization of the films, irrespective of any void density, was assumed after heat treatment at 1000°C for 3 hours. The volume fraction is then given as the ratio of (P/B) - 1 before and after thermal crystallization. We will, however, interpret this ratio as a relative volume fraction, rf_v, since there exists much contention as to the proper method of evaluating an absolute volume fraction, f_v, and the effects of void density are not completely well understood. The quantity rf_v, might more properly be interpreted as the ratio of volume of crystallites V_c, to the volume of crystallites and amorphous material $V_c + V_a$ (since annealing may not remove voids) though rf_v may be a good approximation to f_v. In a network completely lacking voids, rf_v would of course be equal to f_v [$rf_v = V_c/(V_c+V_a)$, $f_v = V_c/(V_c+ V_a+V_{void})$]. Also, even after thermal crystallization, (P/B) - 1 showed a

thickness dependence. This dependence is probably due to the quartz substrate, as the films were not thick enough to eliminate diffraction from the substrates. The thinner the film, the more the quartz profile was revealed, which would raise the background intensity above the purely amorphous intensity. This effect would therefore cause an underestimation of f_v while significant void density causes overestimation.

Figures 3.3-3.5 show the correlation between the optical properties and rf_v. The absorption coefficient α, is related to the extinction coefficient k by

$$\alpha = 4\pi k/\alpha \quad . \tag{3.1}$$

The optical absorption coefficient (Fig. 3.3) for μc-Si:H for photon energies above $\simeq$ 2 eV is below that of a-Si:H, with the reverse holding true for $h\nu \leq 2$ eV. Similar results have been observed for rf glow discharge films[3.20]. The relatively large absorption of μc-Si:H above 2 eV can primarily be attributed to the presence of the amorphous phase in the film[3.20]. As the films become more microcrystalline, α decreases.

The imaginary part of the dielectric constant ϵ_2, and the refractive index n, are shown in Figs. 3.4 and 3.5, where ϵ_2 is given by

$$\epsilon_2 = 2nk \quad . \tag{3.2}$$

The corresponding crystalline spectra of ϵ_2[3.21] and n[3.22] are included in Figs. 3.4 and 3.5 for comparison. As the film changes from an amorphous to a

microcrystalline structure, one observes the development of the shoulder in ϵ_2 at approximately 3.4 eV, characteristic of crystalline silicon. The ϵ_2 spectrum associated with an amorphous network exhibits a relatively broad peak at $\simeq$ 3.25 eV with the lack of a shoulder. Characteristic of the amorphous spectrum is the loss of the fine structure of the crystalline spectrum, which is related to the singularities of the band structure. The low energy tail of the ϵ_2 spectrum is suppressed as rf_v increases initially. As rf_v further increases, the development of the shoulder near 3.4 eV occurs, and a peak appears to be forming at an energy above the initial 3.25 eV peak position. As rf_v increases, ϵ_2 at $\simeq$ 3.25 eV initially decreases, and finally reaches a minimum. Subsequent increases in rf_v past this minimum results in an increase in ϵ_2 to $\simeq$ 15 at 3.5 eV. Similar behaviour has been observed following a crystalline to amorphous transition induced by ion bombardment in GaAs[3.23].

Similar overall behaviour occurs also in the n spectra, as shown in Fig. 3.5. The refractive index spectrum for an amorphous film has a broad maximum near 2.5 eV. As a transition is made to microcrystalline structure, the refractive index at 2 eV, n_o, decreases and the peak at 2.5 eV disappears. A further increase in rf_v results in a peak re-appearing, but shifted to a higher energy at 3.25 eV. A subsequent increase in n_o as a function of rf_v is illustrated in Fig. 3.6.

The low energy refractive index is given approximately by[3.24-3.26]

$$n_o^2 - 1 = \frac{4\pi N_e e^2 \bar{h}^2}{m E_g^2} \quad , \tag{3.3}$$

where N_e is the density of valence band electrons per unit volume, which is related to the material density, m is the electron mass, $\bar{h}$ is Planck's constant, and E_g represents an average separation between valence and conduction bands, and is a measure of the covalent bond strength. The behaviour of n_o and ϵ_2 at 3.5 eV may be explained in terms of material density. If the film density becomes highly deficient due to initial crystallization, one would expect n_o to decrease (Eqn(3.3)). Since these results pertain to material fabricated at a very low substrate temperature (150°C) and high deposition rates ($\simeq$ 10 A/s), one expects ϵ_2 to be suppressed due to low material density[3.31]. Other mechanisms which may be acting to reduce n_o are a reduction of dangling bond density (leading to decreased polarizability), and increased co-ordination. With the decrease of n_o a higher average separation between bonding and antibonding states may be inferred from Eqn(3.3). This increase in separation could arise from a decreased bond length[3.27], and increased co-ordination number[3.28], or removal of bond angle distortions. Paul et al.[3.29] have deduced that in amorphous germanium, the second of these factors is dominant. One may then reasonable expect that with increasing microcrystallinity, the decrease in n_o should be attributed to an increasingly four-fold co-ordinated structure. Similarly, increased material density, as the material tends to become fully co-ordinated, can explain the increase in n_o and ϵ_2 at 3.5 eV, after the initial decrease.

The optical spectra of the film with $rf_v \simeq 0.07$ illustrates the effectiveness of the n spectrum in indicating microcrystallinity. From the shape of the ϵ_2 spectrum in Fig. 3.4, on can deduce that this film is amorphous since its spectrum is very similar

to the amorphous ϵ_2 spectrum. However, the n spectrum remains distinguished from those of amorphous films. We observe no peak at 2.5 eV, associated with an amorphous structure, but rather n is approximately constant between 2 to 3 eV. The refractive index spectrum is an excellent indicator of the onset of microcrystallinity, exhibiting modifications prior to its appearance in the ϵ_2 spectrum. Also note film A in Fig. 3.5. This film was in close proximity to a μc-Si:H film during deposition. We expect that this film is at the onset of microcrystallinity. The n-spectrum indicates this, even though X-ray diffraction shows it to be amorphous.

For amorphous films a peak in n occurs at 2.5 eV, while for microcrystalline films, n is relatively constant on $2 < h\nu < 3$ eV for $rf_v \leq 0.25$ as indicated in Fig. 3.5. Table 3.1 shows the effect of various grain sizes on the n spectra. To quantify the behaviour of n on $2 < h\nu < 3$ eV we consider n at 2.5 eV, n_p (2.5 eV being the peak position for an amorphous spectrum) and n at 2 eV, n_o. The change $n_p - n_o$ is given for various microcrystallite grain sizes ((111) orientation) and for $rf_v \leq 0.25$. It can be seen that the n spectrum is sensitive to grain sizes as small as 10 - 20 A and can be used to detect microcrystallinity in fine grain films.

The optical properties for films of 10 - 20 A microcrystallite grain size, are similar to those for films of 100 - 300 A grain size. Upon crystallization, the n spectrum loses its peak at 2.5 eV and ϵ_2 decreases. The absorption is weaker compared to amorphous films for $h\nu \leq 2$ eV, reversing at higher photon energies.

For parabolic bands, the optical energy gap E_{opt}, can be related to α by

$$\alpha h\nu = B(E - E_{opt})^2 \quad , \tag{3.4}$$

where B is a constant. The plot of $(\alpha h\nu)^{1/2}$ versus $h\nu$, extrapolated to the zero absorption axis, yields E_{opt}. The optical gap versus rf_v is given in Fig. 3.7. The decrease of E_{opt} from $\simeq$ 1.70 - 1.40 , implies the change of Si:H from an amorphous to a microcrystalline structure. The values of E_{opt} versus room temperature dark conductivity σ_d, is given in Fig.3.8. As expected, σ_d increases as E_{opt} decreases. When σ_d exceeds approximately 10^{-8} (ohm-cm)$^{-1}$, crystallization of the specimens has occured, as confirmed by X-ray diffraction measurements. This corresponds to a value of $E_{opt} \sim$ 1.5 eV. Dark conductivity of μc-Si:H is as high as three orders of magnitude above that of a-Si:H.

3.3 Conclusions

X-ray diffraction measurements alone do not provide acceptable structural data, especially when very thin films are involved. This will also be the case for stratified structures such as solar cells. Furthermore, the intensities of X-ray diffraction lines may show a thickness dependence making structural determinations more difficult and less reliable. The use of spectroscopic ellipsometry in determining n and ϵ_2 provides an additional and/or alternative technique for determining structural properties of μc-Si:H films. The n and ϵ_2 spectra can provide structural information for films of crystallite size as small as 10-20 A and of volume fractions of crystallites too small to be detected by X-ray measurements. Ellipsometry also may be preferred to X-ray diffraction measurements when the surface area available is small, or when spatial profiles are desired.

Detailed analysis of the ellipsometry data indicates the following behaviour: As volume fraction of crystallites initially increases, the n spectrum loses its peak at 2.5 eV, characteristic of a-Si:H. An approximately constant value of n between 2 and 3 eV indicates weakly microcrystalline films. Films with increasingly higher volume fraction crystallites, show a peak forming in n at 3.5 eV. The ϵ_2 spectrum is initially suppressed in the low energy tail, after which a shoulder appears near 3.25 eV as the volume fraction of crystallites increases. The peak in ϵ_2 is concomitantly shifted to higher energies. The optical gap E_{opt}, decreases from 1.70 to 1.40 eV as an amorphous film takes on a $\simeq$ 100% volume fraction of crystallites.

References

[3.1] S. Veprek, Z. Iqbal. H.R. Oswald, F.A. Sarott, and J.J. Wagner, J. Phys. (Paris) **42**, C4-251 (1981).

[3.2] A. Matsuda, j. Non-Cryst. Solids, **59,60,** 767 (1983).

[3.3] A. Hiraki, T. Imura, K. Mogi, and M. Tashiro, J.Phys. (Paris) **42**, C4-277 (1981).

[3.4] T.D. Moustakas, D.A. Weitz, E.B. Prestridge, and R. Friedman, Mater. Res. Soc. **38,** 401 (1985).

[3.5] H. Saito, H. Sannomiya, T. Yamaguchi, N. Tanaka, Appl. Phys. A (Ger) **A35,** 241 (1984).

[3.6] S. Nishida, A. Tasaki, M. Konagi, and K. Takahashi, Mater. Res. Soc. **49,** 47 (1985).

[3.7] J. Shirafuji, S. Nagata, and M. Kuwagaki, J. Appl. Phys. **58,**3661

[3.8] M. Kumeda, J. Komatsu, and T. Simizu, Thin Solid Films, **129,** 227 (1985).

[3.9] S. Miyazaki, H. Hirata, S. Ohkawa, and M. Hirose, J. Non-Cryst. Solids, **77,78,** pt. 2, 781 (1985).

[3.10]G. Rajeswaran and F.J. Kampas, J. Non-Cryst. Solids, **66,** 31 (1984).

[3.11]Y. Uchida, T. Ichimura, M. Ueno, and H. Haruki, Jap. J. Appl. Phys. **L586**(1982).

[3.12]Z. Vardeny, D. Pfost, Hsian-na Lui, and J. Tauc, AIP Conf. (USA) no. 120, 107 (1984).

[3.13]S. Hasegawa, K. Kishi, and Y. Kurata, Philos. Mag. B, 52, 199 (1985).

[3.14]S. Hasegawa, S. Narikawa, and Y. Kurata, Philos. Mag. B, 48, 431 (1983).

[3.15]S.R. Mejia, R.D. McLeod, W. Pries, P. Shufflebotham, D.J. Thomson, J. White, J. Schellenberg, K.C. Kao, and H.C. Card, J. Non-Cryst. Solids, 77,78, 765 (1985).

[3.16]S.R. Mejia, R.D. McLeod, K.C. Kao, and H.C. Card, Rev. Sci. Instr., 57, 493 (1986).

[3.17]H. Adachi and K.C. Kao, J. Appl. Phys., **51,** 6326 (1980)

[3.18]K.C. Kao, R.D. McLeod, C.H. Leung, H.C. Card, and H. Watanabe, J. Phys. D, **16,**1801

[3.19]H.P. Klug and L.E. Alexander, "X-ray Diffraction Procedures" (Wiley, New York, 1954) Chap. 6.

[3.20]Y. Mishima, S. Miyazaki, M. Hirose, and Y. Osaka, Philos. Mag. B, 46, 1 (1982).

[3.21]D.T. Pierce and W.E. Spicer, Phys. Rev. B, **5,** 3017 (1972).

[3.22]G.K.M. Thutupalli and S.G. Tomlin, Solid State Phys., 10, 467 (1977).

[3.23]D.E. Aspnes, S.M. Kelso, C.G. Olson, and D.W. Lynch, Phys. Rev. Lett., 48, 1863 (1982).

[3.24]R. Zallen, "The Physics of Amorphous Solids" (Wiley, New York, 1983) Chap. 6.

[3.25]Zhang Fang-ging, Chen Guang-hua, Liu Zhi, and Wang Hui-sheng, J. Non-Cryst. Solids, **59,60,** 565 (1983).

[3.26]E.C. Freeman and W. Paul, Phys. Rev. B, **20,** 716 (1979).

[3.27]J.A. Van Vechtan, Phys. Rev., **182,** 891 (1969).

[3.28]J.C. Phillips, Phys. Status Solidi B, **44,** K1 (1971).

[3.29]W. Paul and R.J. Temkin, Adv. Phys., **22,** 531 (1973).

[3.30]J.J. Schellenberg, R.D. McLeod, S.R. Mejia, H.C. Card, and K.C. Kao, Appl. Phys. Lett., **48,** 163 (1986).

[3.31]B. Drevillon and F. Vaillant, Thin Solid Films, **124,** 217 (1985).

FIGURES AND TABLES

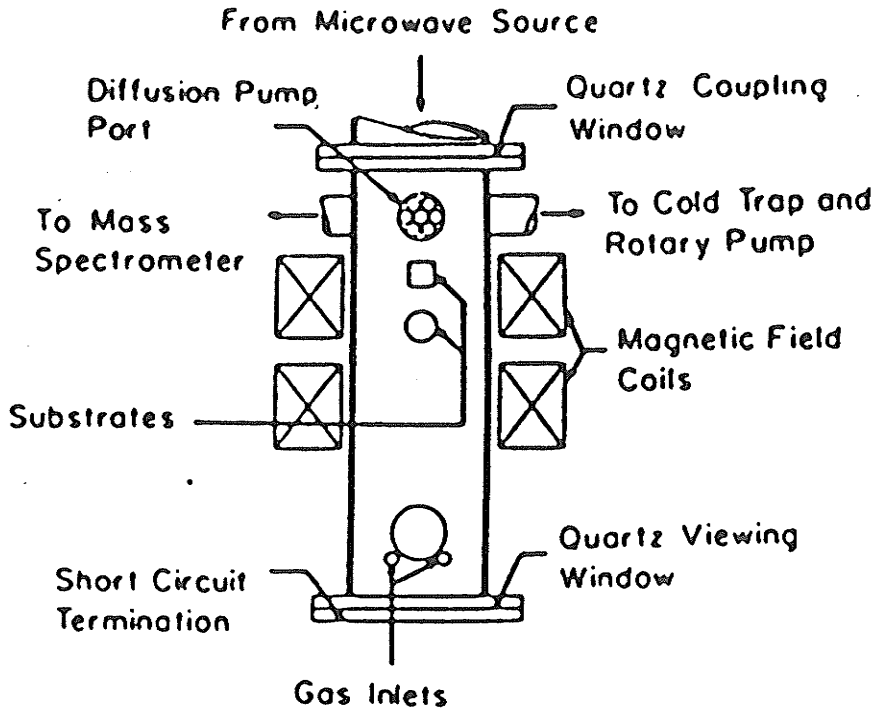

Fig. 3.1 Microwave deposition system.

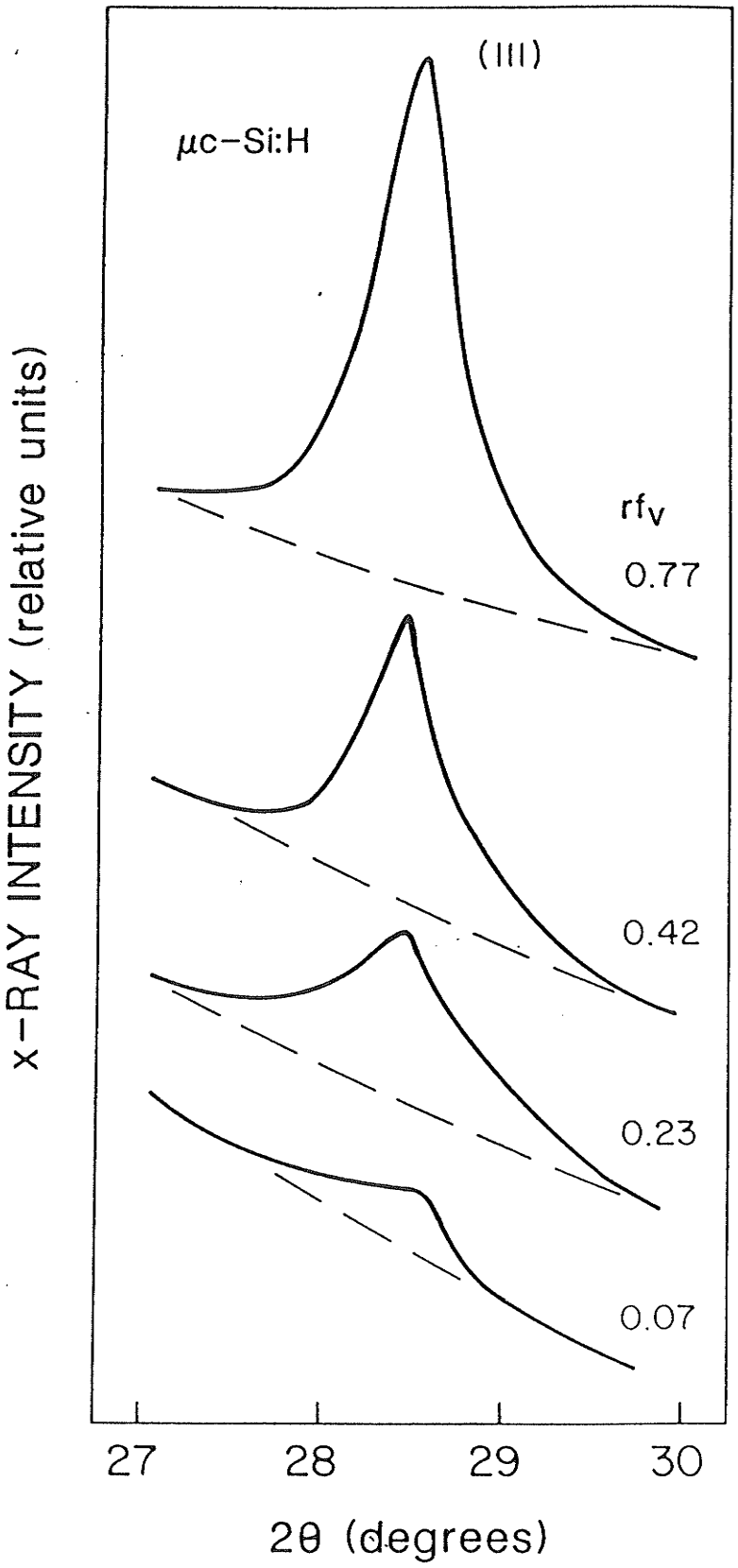

Fig. 3.2 X-ray diffraction profiles for μc-Si:H films. A measure of the relative volume fraction of crystallites rf_v, is indicated.

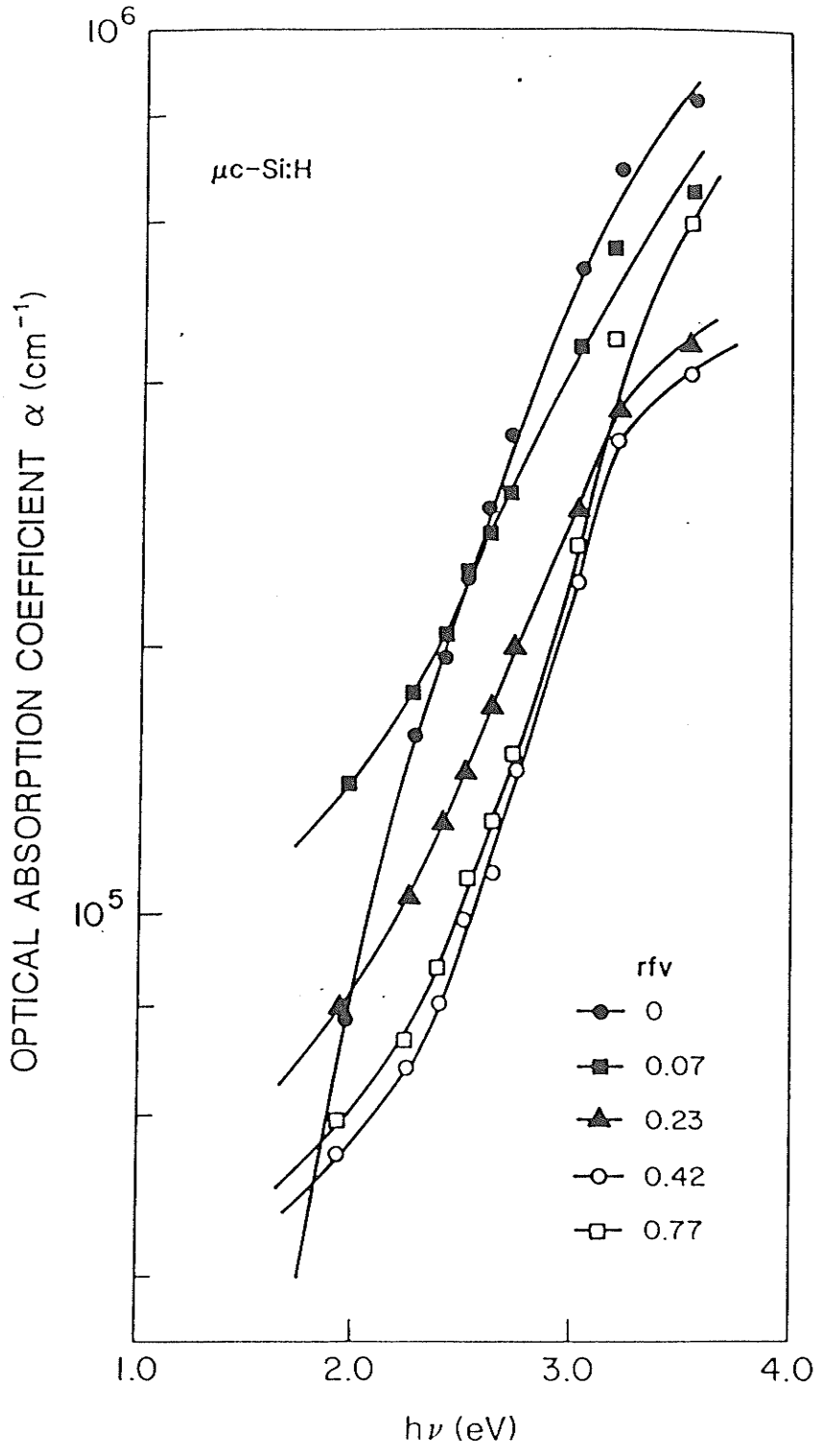

Fig. 3.3 Optical absorption coefficient versus photon energy for μc-Si:H films with the relative volume fraction of crystallites rf_v, as a parameter (only a few shown for clarity).

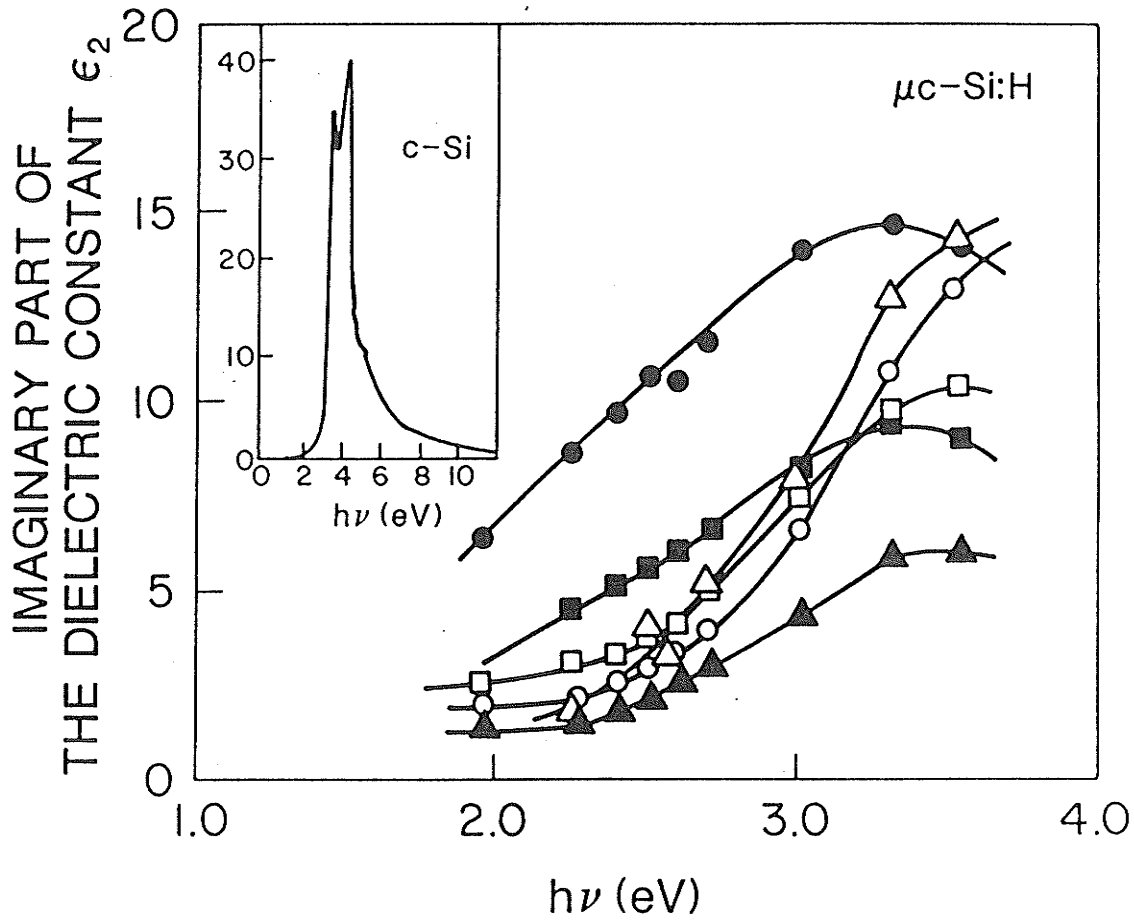

Fig. 3.4 Imaginary part of the dielectric constant versus photon energy for μc-Si:H films with the relative volume fraction of crystallites rf_v, as a parameter. rf_v: 0 (●), 0.07 (■), 0.42 (▲), 0.77 (○), 0.82 (□), and 1.0 (△). The inset shows the imaginary part of the dielectric constant versus photon energy of crystalline Si (after [3.21]).

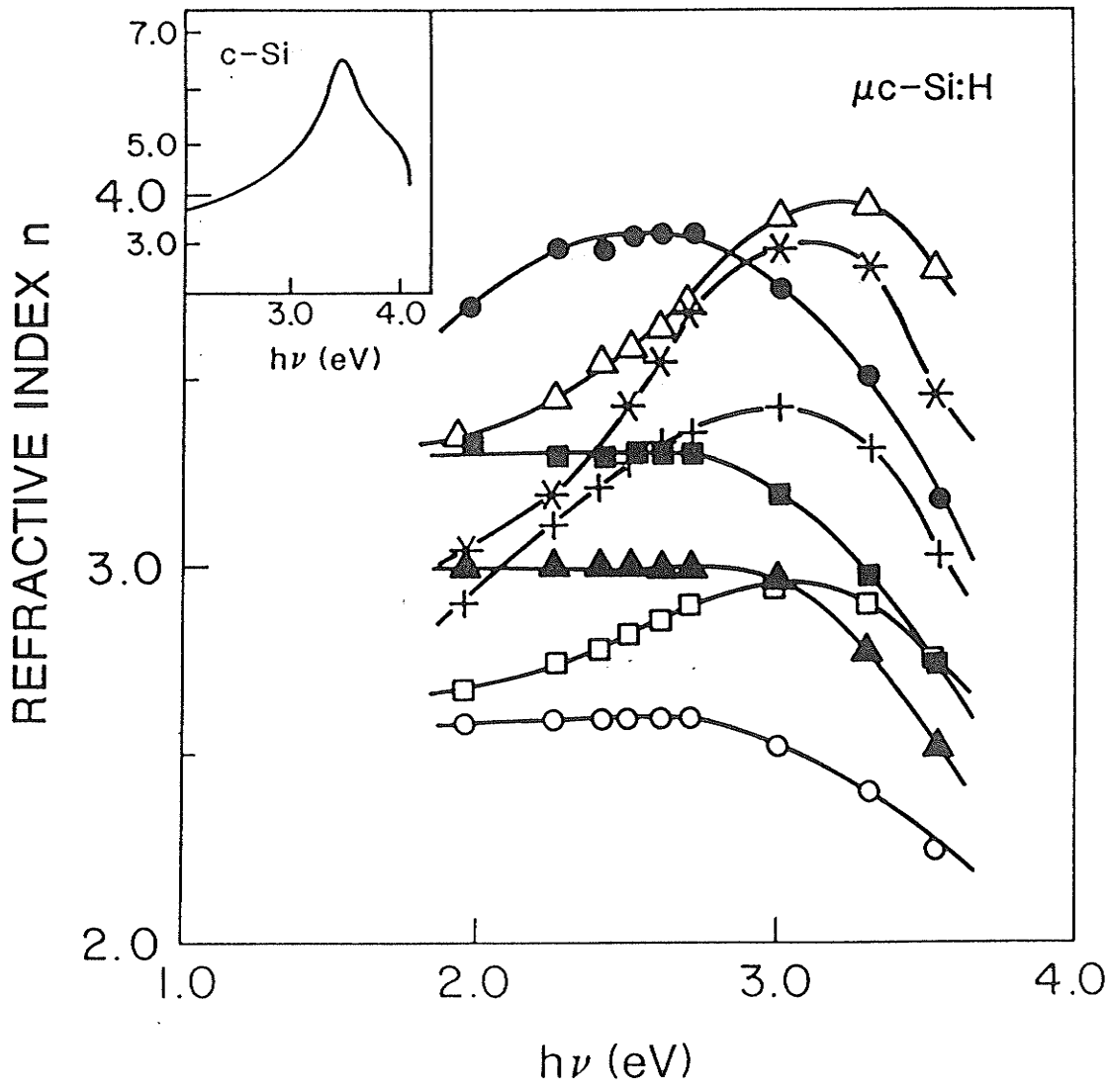

Fig. 3.5 Refractive index versus photon energy for μc-Si:H films with relative volume fraction of crystallites, rf_v, as a parameter. rf_v: 0 (●), 0 (■), 0.07 (▲), 0.23 (○), 0.42 (□), 0.77 (△), 0.82 (+), and 1.0 (✱). Note, film A: (■) see text. The inset shows the refractive index versus photon energy of crystalline Si (after [3.22]).

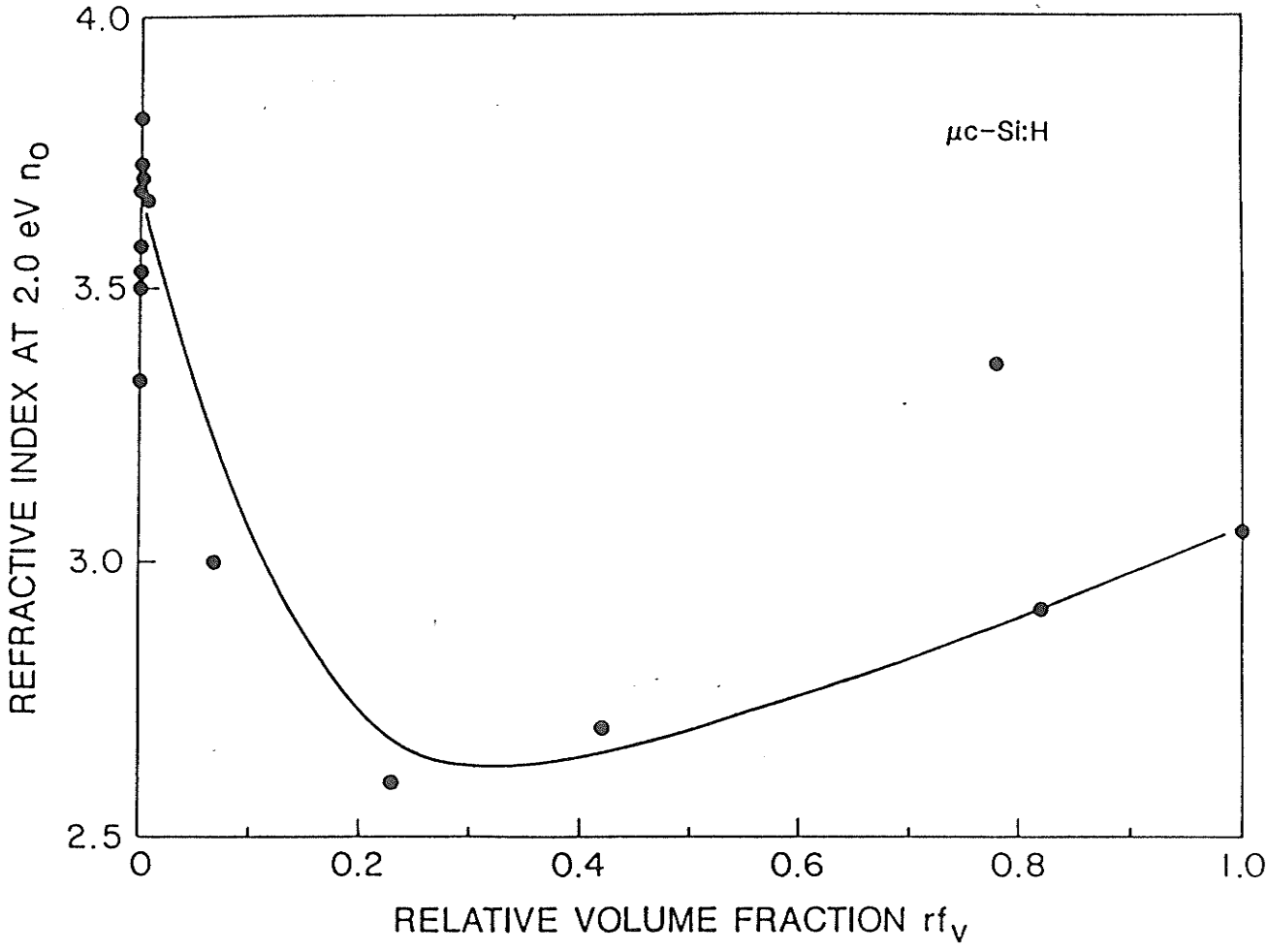

Fig. 3.6 **Refractive index at $h\nu$ = 2.0 eV of μc-Si:H films versus relative volume fraction of crystallites.**

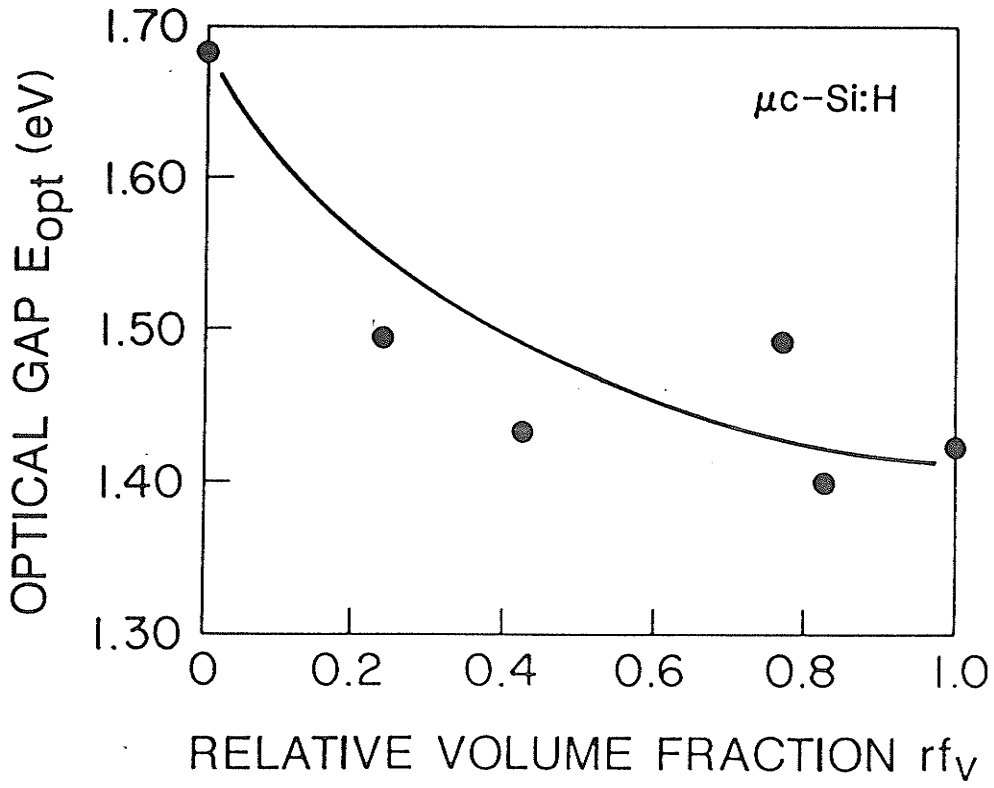

Fig. 3.7 Optical energy gap of μc-Si:H films versus relative volume fraction of crystallites.

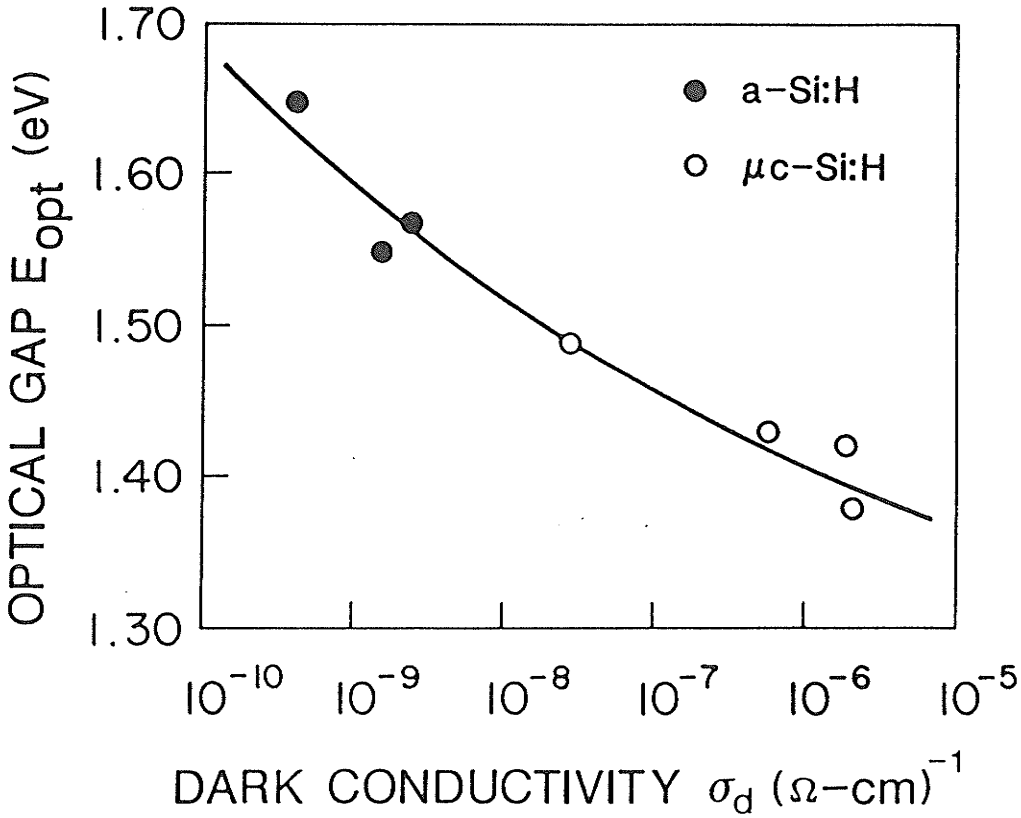

Fig. 3.8 Optical energy gap of a-Si:H and μc-Si:H films versus room temperature dark conductivity.

Table 3.1 Refractive index parameter (n_p - n_0) versus crystallite grain size (δ) for μc-Si:H films with relative volume fraction of crystallites (rf_v) ≤ 0.25.

rf_v	δ(Å)	$n_p - n_o$
0	—	0.20
<0.25	10–20	0.02
0.23	100	0.01
0.07	163	0.02

Chapter 4

A MULTILAYER OPTICAL MODEL

Here a model is developed to correlate optical and structural properties of amorphous and microcrystalline silicon films. We refer specifically to silicon films although the model is not limited to silicon films alone. In the first section of this chapter, films are modelled as multilayer structures of various compositions in order to relate optical data, or more specifically spectrally resolved ellipsometry (SE), to volume fractions of voids, amorphous, and crystalline phases. In the model, the dielectric functions of the constituents of the films, that is a-Si:H, c-Si:H and void phases, are termed the reference dielectric functions. Any real film (a-Si:H, -Si:H, or c-Si:H) can then be modelled by a combination of these reference dielectric functions through an effective medium approximation, thus obtaining the respective volume fraction of each phase.

The next section of this chapter deals with the effects of void content, bond length dilation, and bond angle variation and a more self consistent approach is developed within the Penn-Phillips Model for amorphous semiconductors. In an a-Si:H film with significant void content, we would expect that the dielectric response of the a-Si:H phase would not be the same as that for fully developed and well coordinated a-Si:H. We take the original dielectric response of the "good quality" a-Si:H, here after referred to simply as a-Si:H, and modify it to take into account defects,

such as void content and excessive bond angle distortion and bond length dilation. The dielectric response of this "defective" a-Si:H phase, here after referred to as a-Si:H', is then used as the reference dielectric function for the amorphous Si phase in the optical model calculations. In Chap. 5 it will be demonstrated that optical, density, and X-ray diffraction measurements can all be incorporated within this model on a self consistent basis to extract structural information from optical measurements for amorphous and microcrystalline thin films.

4.1 Complex Reflectance Ratio and an Effective Medium Approximation

The SE data can be analyzed on the basis of multilayer structures and an effective medium approximation. This approach was first applied by Aspnes et al.[4.1] for a-Si:H deposited by CVD. The SE data is represented by the set of points (ρ_i, E_i), $i = 1,2..N$ where the reflectance ratio $\rho_i = R_p/R_s = \tan\psi_i[\exp(i\Delta)]$, is obtained using the conventional experimentally determined ellipsometric angles Δ and ψ. Each film can be modelled as a multilayer film, with constituent layers of various compositions and thicknesses. The object then is to find the variables x_ν, $\nu = 1,2,...n$ representing the optical system, with values which minimize the error between the experimental and calculated reflectance ratio. This error is

$$\delta^2 = \sum_{i=0}^{N} |\rho_i^{exp} - \rho_i^{cal}(x_1, x_2, ...x_n, E_i)|^2 \quad , \tag{4.1}$$

where the vector $X = (x_1, x_2, ...x_n)$ represents the real variables we wish to obtain, for example, the volume fractions of a-Si, c-Si, void, etc.

The dielectric functions for each layer are determined by the Bruggeman effective medium approximation which is expressed as[4.2]

$$0 = \sum_{i=0}^{n} f_i \frac{\epsilon_i - \epsilon}{\epsilon_i + 2\epsilon} \quad , \tag{4.2}$$

where f_i is the volume fraction of each of the components i, and ϵ_i are the complex dielectric functions of that component. For Si:H films, the layers can consist of various fractions of a-Si:H, c-Si, and voids. Solving Eqn.(4.2) for ϵ gives the dielectric function of each individual layer. After the dielectric functions of the individual layers are known, the reflectivity of the entire stratified structure can be calculated from the Fresnel coefficients given in terms of the dielectric functions of the layers. We take the case of a four phase model as an illustrative calculation. The reflection coefficients for a four phase model (phases 0,1,2, and 3, phase 0 being the ambient) are given by[4.3,4.4]

$$\rho = R_p / R_s \tag{4.3a}$$

$$R = \frac{(r_{01} + r_{12}e^{-j2\beta_1}) + (r_{01}r_{12} + e^{-j2\beta_1})r_{23}e^{-j2\beta_2}}{(1 + r_{01}r_{12}e^{-j2\beta_1}) + (r_{12} + r_{01}e^{-j2\beta_1})r_{23}e^{-j2\beta_2}} \tag{4.3b}$$

$$\beta_i = 2\pi(d_i/\lambda)N_i\cos\phi_i \tag{4.3c}$$

$$\cos\phi_i = (1 - (N_0\sin\phi_0/N_i)^2)^{1/2} \quad , \tag{4.3d}$$

where N_i and d_i are the complex refractive index and thickness of the individual

layers i, respectively, ϕ_0 is the angle of incidence, and λ is the wavelength of light. Eqn.(4.3) applies to both p and s polarizations by simply attaching the subscript p or s to R and to the individual Fresnel coefficients. The Fresnel reflection coefficients are given by

$$r_{ij_p} = \frac{N_j \cos\phi_i - N_i \cos\phi_j}{N_j \cos\phi_i + N_i \cos\phi_j} \tag{4.4a}$$

$$r_{ij_s} = \frac{N_i \cos\phi_i - N_j \cos\phi_j}{N_i \cos\phi_i + N_j \cos\phi_j} \quad , \tag{4.4b}$$

where N_i is calculated through the effective medium approximation. Extension to any number of layers is easily accomplished by matrix multiplication of 2 x 2 matrices representing successive interfaces and layers of the stratified structure[4.4].

Based on linear regression analysis[4.5] the unbiased estimator of the standard deviation is given by

$$\hat{\sigma} = \delta / \sqrt{N - p - 1} \quad , \tag{4.5}$$

where p is the number of free variables. Defining a matrix M where

$$m_{\mu\nu} = \sum_{i=0}^{N} \mathrm{Re}\left(\frac{\partial \rho}{\partial x_\mu} \frac{\partial \rho^*}{\partial x_\nu} \right)_{E=E_i} \quad , \tag{4.6}$$

$a_{\mu\nu}$ is an element of matrix A where $A = M^{-1}$. The correlations $c_{\mu\nu}$ between the variables x_μ and x_ν, and the 90% confidence limits δx_ν of x_ν are then given by

$$c_{\mu\nu} = a_{\mu\nu} / \sqrt{a_{\mu\mu} a_{\nu\nu}} \tag{4.7a}$$

$$\delta x_\nu = t\ \hat{\sigma}\ \sqrt{a_{\nu\nu}}\ , \tag{4.7b}$$

where t is the 90% value of a student t-distribution.

The 90% confidence limits for the fit to the data are required to ensure that the models are not overparameterized. Too many parameters, or correlated parameters, result in drastic weakening of the confidence limits, therefore one must provide a check against adding parameters indiscriminately. If any $c_{\mu\nu} \rightarrow \pm 1$ the matrix M becomes singular and the elements of A become large, leading to very large confidence limits. The unbiased estimator of the standard deviation along with the confidence limits are used to determine the suitability of a particular model.

4.2 Dielectric Response of a "Defective" a-Si:H Matrix

Here we obtain a model to represent the dielectric spectra of the a-Si:H phase which may contain a large concentration of voids and excessive bond angle distortion and bond length dilation. Fig. 4.1 shows the dielectric response of a-Si:H, a-Ge:H, and a-Si_3N_4, which indicates that the dielectric response of many tetrahedrally based amorphous substances are similar[4.6], and that the dielectric response of such materials is essentially that of the tetrahedral bond. We can therefore model the dielectric response of the a-Si:H phase by scaling the original dielectric response as

$$\epsilon_2' = c_a \epsilon_2(c_e E)\ , \tag{4.8}$$

where ϵ_2 and ϵ_2' are the imaginary part of the dielectric constant for a-Si:H and a-Si:H', respectively. We now must calculate the amplitude and energy scaling parameters, c_a and c_e.

The energy scaling parameter should be related to the average-gap parameter or Penn gap E_g, where within the Penn-Phillips model the peak location of the ϵ_2 spectrum gives E_g. The Penn gap is simply the "average" energy separation between the conduction band and valence band and is a measure of the bond strength. We calculate c_e such that consistency is maintained with E_g, that is, c_e is given by

$$c_e = E_g / E_g' \quad , \tag{4.9}$$

where E_g' is the Penn gap of the a-Si:H' phase. The relation of E_g to the bond length, r, has been discussed by Van Vetchen[4.7] who showed that

$$E_g \sim r^{-b} \quad , \tag{4.10}$$

where for Si, $b = 2.48$. We may also include the effects of a change in average coordination number, Z. Phillips[4.8] has shown that a reduction in Z decreases E_g, or more specifically

$$E_g \sim Z^2 \quad . \tag{4.11}$$

We can thus express the Penn gaps as

$$\frac{E_g}{E_g'} = \left[\frac{r}{r'}\right]^{-b} \left[\frac{Z}{Z'}\right]^2 f_B = c_e \quad , \tag{4.12}$$

where the factor f_B is included to account for the variations of bond angles, and r' and Z' refer to a-Si:H'.

The relation between bond strength and the bond angle has been discussed by Pauling[4.9]. The angular part of the wave functions of a hybridized s-p tetrahedral orbital in the bond direction is

$$\phi(\theta_b) = \frac{1}{2} + \frac{3}{2}\cos\theta_b \quad , \tag{4.13}$$

where the bond energy is proportional to $|\phi|^2$. Eqn(4.13) has a maximum for $\theta_b = 0$. This is one tetrahedral bond, the others then forming at angles rotated through 109°28' in order to maximize the bond strength; all bonds having identical wave functions except for the rotation. If we assume that in a-Si:H, bonds are undistorted and that a-Si:H' acquires 10° bond distortion or deviation, then

$$|\phi(10°)|^2 = 3.91 = 0.977\ |\phi(0°)|^2 \quad ,$$

or the maximum effect of bond variation is only $\simeq$ 2.3%. We may then take $f_B \simeq 1$ by noting that a-Si:H may have less bond angle deviation than the a-Si:H' phase, but obviously not as small as 0°.

We can calculate the reduction in Z due to the presence of voids as follows. Assume as a first approximation, a lower density material is formed by the removal of n-atom clusters from an original high density a-Si (small H content) network without change of the remaining atomic network. This will then reduce Z by leaving some Si atoms in the remaining network with fewer Si neighbours. We further

assume that bonding requirements of all n atoms in each cluster removed are fully satisfied. Some atoms in each cluster can bond with other atoms in the same cluster, however a fraction of the bonds of the n atoms are external to the cluster. This fraction will of course depend on the size and shape of the removed cluster. We can calculate the reduction in Z due to the decrease in density, ρ. We define a parameter f as

$$f = \frac{d\ln Z}{d\ln\rho} = \frac{\Delta Z/Z}{\Delta\rho/\rho} \quad . \tag{4.14}$$

From a total of T Si atoms, consider removing a fraction F, where $F < 0.5$, of 1-atom clusters, or monovacancies. The change in density, $\Delta\rho/\rho$, is simply F. Assuming in the original a-Si phase, each Si atom has 4 Si nearest neighbours, the total number of bonds N' is now

$$N' = 4T - 4FT - 4FT \quad . \tag{4.15}$$

N' is calculated by subtracting from the total number of bonds in the original matrix, $N = 4T$, the contribution to N from the lost atoms, $4FT$, and the net loss of 1 bond for the 4 atoms surrounding the monovacancy or 4 bonds per atom lost. The third term in Eqn(4.15) represents the number of bonds external to the cluster, N_{ext}. The new coordination number Z' is now simply

$$Z' = \frac{4T - 8FT}{T - FT} = 4 - \frac{4F}{1-F} \quad , \tag{4.16}$$

which gives

$$f = \frac{\Delta Z/Z}{\Delta\rho/\rho} = \frac{4F}{1-F}\,\frac{1}{4}\,\frac{1}{F} \approx 1 + F \quad , \tag{4.17}$$

Consider removing atoms or clusters which are in n-atom chains, then

$$N' = 4T - 4FT - \frac{FT}{n}(2n+2) \quad , \tag{4.18}$$

where for each chain there are 2n+2 external bonds which are lost. For this case

$$\frac{\Delta Z}{Z} = \frac{1+\frac{1}{n}}{2}\,\frac{F}{1-F} \quad , \tag{4.19}$$

which gives

$$f \approx \frac{1+\frac{1}{n}}{2}\,(1+F) \quad . \tag{4.20}$$

We can now generalize this approach to some arbitrary size of cluster removed and estimate the maximum reduction of Z by assuming that the a-Si matrix is that of the Bethe Lattice (BL) as shown in Fig. 4.2. The BL is an infinite non-periodic fully connected system of atoms, where every atom is bonded in the same configuration. It is an ideal mathematical model of an infinite random network. In this case, no rings of Si atoms are formed and all bonds on the periphery of a removed cluster are external to the cluster and as such reduce Z of the resulting network. If the cluster is of the form of the BL, the number of atoms per cluster, n, is

$$n = 1 + 4\sum_{p=0}^{s-1} 3^p \quad , \tag{4.21}$$

where s is the number of shells in the cluster (see Fig. 4.2). If no rings exist in the original a-Si network, as assumed in the BL model, the number of external bonds per cluster is

$$3\cdot(4\cdot 3^{s-1}) = 4\cdot 3^{s} \quad ,$$

where there are $4(3^{s-1})$ atoms in the outer shell. Removing a fraction F of atoms of clusters, each with s shells, we have

$$Z' = 4 - \frac{4\cdot 3^{s}}{1 + 4\sum_{p=0}^{s-1} 3^{p}} \frac{F}{1-F} \quad , \tag{4.22}$$

which gives

$$f \approx \frac{3^{s}}{1 + 4\sum_{p=0}^{s-1} 3^{p}} (1+F) = f_{0}(1+F) \quad . \tag{4.23}$$

As s becomes large, we lose 2 bonds to the remaining network per atom removed.

To estimate the minimum effect on Z (least reduction) we consider the exact tetrahedral structure of c-Si and suppose the voids to be formed by removing cubes of atoms (ie, minimize the surface area and hence the number of external bonds for a given void volume) of dimension L, where L is an integer number of lattice constants, (L=ma). For m=1, we have the unit cell as shown in Fig. 4.3(a). The tetrahedral structure is that of two interpenetrating face-centered cubic Bravais lattices, displaced along the body diagonal of the cubic cell by one quarter the length of

the diagonal. It can be regarded as a face-centered cubic lattice with two point basis 0 and (a/4)($\hat{x} + \hat{y} + \hat{z}$). Fig. 4.3(a) gives the view along the $\hat{z}$ direction, with views along $\hat{x}$ and $\hat{y}$ being identical. If we cut the lattice as indicated in Fig. 4.3(a) (ie, we always cut just on the outside of the cube to minimize the number of external bonds per atom removed) and remove the cube, the number of external bonds is 36 with a total of 18 atoms removed, that is, 8 corner atoms × 3 bonds/corner atom plus 6 face-centered atoms × 2 bonds/face-centered atom.

Voids can be created by removing cubic clusters of dimension L=ma. Fig. 4.3(b) shows a view of a cube for m=2, where the atoms having bonds that are always internal to the cube are now not shown. As m increases, some of the bonds which were previously external become internal to the cluster. The number of atoms on the surface of one face of the cube minus those on the perimeter or edges (m atoms per edge x 4 edges) of the face is

$$(m+1)^2 + m^2 - 4m \quad ,$$

therefore the total number of surface atoms is

$$T_s = 6[(m+1)^2 + m^2 - 4m] + 2(4m) + 4(m-1) = 2(6m^2 + 1) \quad .$$

Referring back to Fig. 4.3(b), the number of external bonds per cube, N_{ext}^{cube}, is 2 x T_s + 1 bond per atom at the cube corners, or

$$N_{ext}^{cube} = 4(6m^2 + 1) + 8 = 12(2n^2 + 1) \quad . \tag{4.24}$$

We now calculate the number of atoms per cube of size L. For a cube of dimension ma, the total number of atoms per cube, $T^{cube}(m)$, is

$$T^{cube}(m) = (m+1)^3 + 3m^2(m+1) + 4m^3 = 8m^3 + 6m^2 + 3m + 1 \quad . \quad (4.25)$$

Then as before, we remove a fraction F atoms in cubes of size L=ma, which gives

$$Z' = 4 - \frac{N_{ext}^{cube}(m)}{T^{cube}(m)} \frac{F}{1-F} \quad , \quad (4.26)$$

and

$$f \approx \frac{1}{4} \frac{N_{ext}^{cube}(m)}{T^{cube}(m)} (1+F) = f_0 (1+F) \quad . \quad (4.27)$$

Fig. 4.4 shows the variation of f_0 with void size for the case of a cluster removed from a BL and a cube removed from a tetrahedral structure. The void size is roughly calculated as $2sr$ with r = 2.35 A (bond length for c-Si) for the BL case and ma, where a = 5.43 A (lattice constant for c-Si), for the cube case. It can be seen that for voids $\geq$ 25 A, we may take $f_0 \simeq$ 0.30 - 0.25. Using Eqn (4.14), we can then rewrite Eqn (4.12) as

$$c_e = \left[\frac{r}{r'}\right]^{-b} \left[\frac{\rho}{\rho'}\right]^{2f} f_B \quad , \quad (4.28)$$

where b = 2.5.

The parameter c_a can be determined from the sum rule for the effective number of electrons participating in optical transitions[4.10]

$$n_{eff} = \frac{m_e}{2\pi^2 e^2 \bar{h}^2 N_a} \int_0^E E' \epsilon_2(E')dE' = \frac{K}{N_a} \int_0^E E' \epsilon_2(E')dE' \quad , \qquad (4.29)$$

where N_a is the number of Si atoms per unit volume, m_e is the effective electron mass, and $\bar{h}$ is the reduced Planck's constant. For a-Si:H' we have

$$n_{eff}' = \frac{K}{N_a'} \int_0^E E' c_a \epsilon_2(c_e E')dE' = \frac{K}{N_a'} \frac{c_a}{c_e^2} \int_0^E \mathrm{E}' \epsilon_2(\mathrm{E})d\,\mathrm{E}' \quad . \qquad (4.30)$$

From Eqn(4.29) and Eqn(4.30), we have

$$c_a = \frac{n_{eff}'}{n_{eff}} \frac{N_a'}{N_a} c_e^2 \quad . \qquad (4.31)$$

Finally, we must determine the scaling of the real part of the dielectric constant, ϵ_1. Here we can make use of the well known Kramers-Kronig dispersion relation[4.10]

$$\epsilon_1(\omega) = 1 + \frac{2}{\pi} P \int_o^\infty \frac{\omega' \epsilon_2(\omega')d\,\omega'}{[\omega']^2 - \omega^2} \quad , \qquad (4.32)$$

where P denotes the Cauchy principal of the integral. Obviously, if we scale ϵ_2 in energy, we must also scale ϵ_1 by the same factor c_e [ie., $\epsilon_1(E) \rightarrow \epsilon_1'(c_e E)$] to maintain consistency with Eqn(4.32). To determine ϵ_1' uniquely, we can calculate ϵ_1'

from the sum rule obtained from Eqn(4.32) when $\omega \rightarrow 0$ or

$$\epsilon_1(0) - 1 = \frac{2}{\pi}\int_0^\infty \frac{\epsilon_2(\omega')}{\omega'} d\omega' \quad , \tag{4.33}$$

or in terms of energy E

$$\epsilon_1(0) - 1 = \frac{2}{\pi}\int_0^\infty \frac{\epsilon_2(E')}{E'} dE' \quad . \tag{4.34}$$

Therefore we can write

$$\epsilon_1'(0) - 1 = \frac{2}{\pi}\int_0^\infty \frac{c_a \epsilon_2(c_e E')}{E'} dE' = c_a \frac{2}{\pi}\int_0^\infty \frac{\epsilon_2(\mathbf{E}')}{\mathbf{E}'} d\mathbf{E}' \quad . \tag{4.35}$$

This gives with Eqn(4.34)

$$\epsilon_1'(0) = 1 + c_a[\epsilon_1(0) - 1] \quad . \tag{4.36}$$

Since ϵ_1 must also be scaled in energy, we have

$$\epsilon_1'(E) = 1 + c_a[\epsilon_1(c_e E) - 1] \quad . \tag{4.37}$$

We can now calculate the dielectric response of the a-Si:H′ network in terms of the a-Si:H dielectric response.

4.3 Concluding Remarks

The basic procedure to extract the volume fractions of the a-Si, c-Si, and void phases in a silicon film has been outlined in section 4.1. We can incorporate second order effects, such as bond length dilation, to obtain a more self consistent model. X-ray diffraction measurements can be used to substantiate the parameters r', Z', and ρ and volume fraction of crystallites, and hence these measurements can also be useful within this model. This point will be discussed further in Chapter 5 where we will apply the model to the experimental results presented in Chapter 3.

In summary, Eqn(4.1) allows us to extract the film properties of interest, for example, the volume fraction of the a-Si phase in a microcrystalline silicon film. The variable ρ_i^{cal} is calculated via Eqn(4.3) and Eqn(4.4). The reference dielectric constant of any phase can be obtained from data available in literature, and hence the dielectric response of a composite layer is calculated from Eqn(4.2) for use in Eqn(4.3) and Eqn(4.4).

An improvement to the model can be acheived as outlined in section 4.2. The reference dielectic constant of the a-Si:H phase can be used in Eqn(4.8) and Eqn(4.37) to calculate a new dielectric response due to the effects of voids, bond length dilation, and bond angle distortions. This dielectric response is then used in Eqn(4.2) to calculate the dielectric response of a composite layer.

References

[4.1] D.E. Aspnes and J.B. Theeten, Phys. Rev., **B20,** 3292 (1979).

[4.2] D.A.G. Bruggeman, Ann. Phys. (Leipzig), **24,** 636 (1935).

[4.3] O.S. Heavens, "Optical Properties of Thin Solid Films", (Dover, New York, 1965).

[4.4] R.M.A. Azzam and N.M. Bashara, Ellipsometry and Polarized Light (North-Holland, Amsterdam, 1977).

[4.5] E.S. Keeping, "Introduction to Statistical Inference", (van Nostrand, Princeton, 1962), chap. 12.

[4.6] M.L. Theye, in "Optical Properties of Solids: New Developments", B.O. Seraphin, Ed. (North-Holland, Amsterdam, 1976) p. 353.

[4.7] J. Van Vetchen, Phys. Rev., **182,** 891, (1969).

[4.8] J.C. Phillips, Phys. Stat. Sol. B, **44,** K1 (1971).

[4.9] L. Pauling, "The Nature of the Chemical Bond", (Cornell University Press, 1967) Chap. 4.

[4.10]Topics in Appl. Phys., **56,** "The Physics of Hydrogenated Amorphous Silicon II, Electronic and Structural Properties", J.D. Joannopoulus and G. Lucovsky, Ed. (Springer-Verlag, 1984) Chap. 3.

[4.11]D.T. Pierce and W.E. Spicer, Phys. Rev., **B2**, 3017 (1972).

[4.12]T.M. Donovan, W.E. Spicer, J.M. Bennett, and E.J. Ashley, Phys. Rev., **B2**, 397 (1970).

[4.13]H.R. Phillip, J. Electrochem. Soc., **120**, 295 (1973).

FIGURES

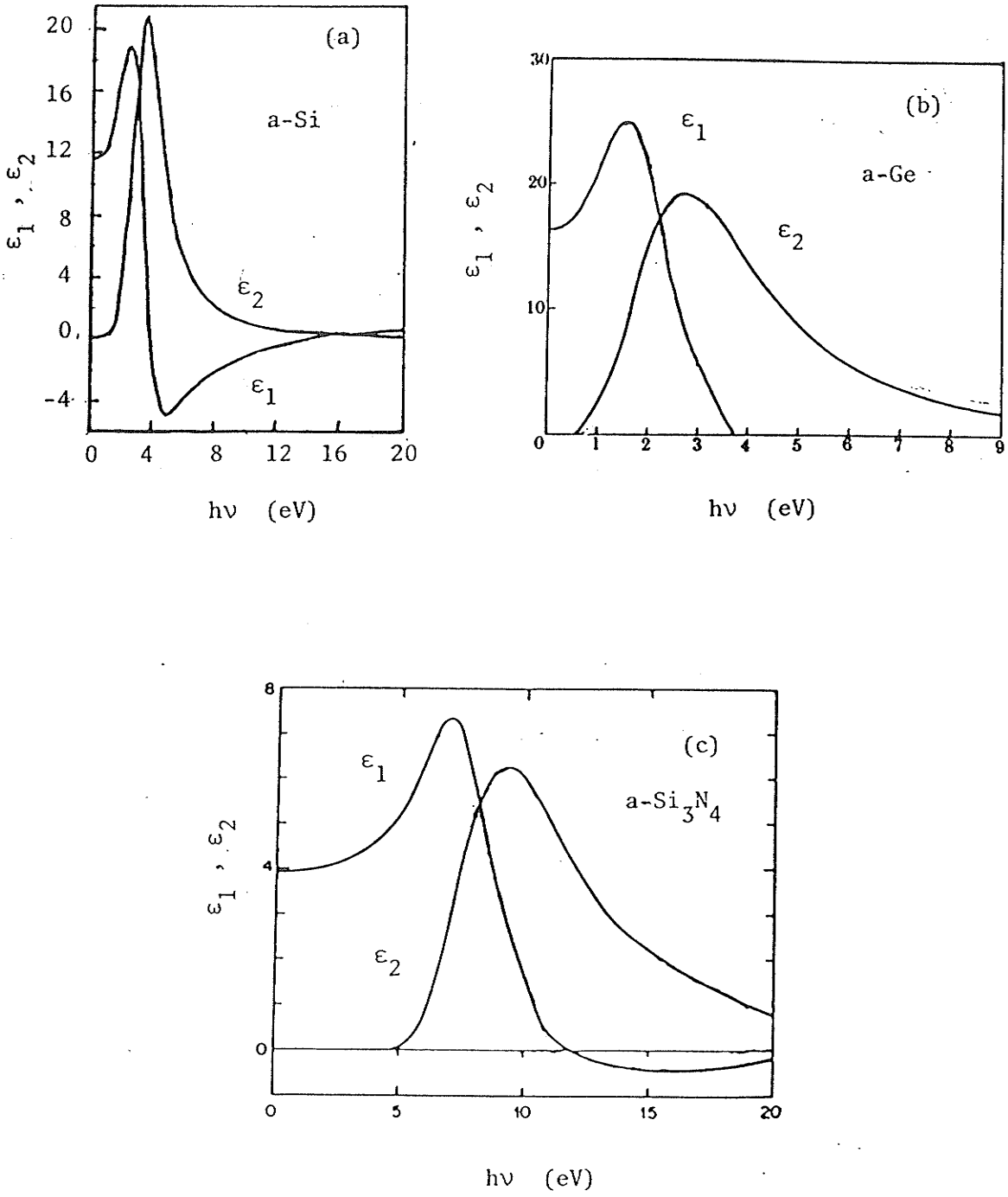

Fig. 4.1 Comparison of the dielectric constants of a-Si (after [4.11]), a-Ge (after [4.12]), and a-Si_3N_4 (after [4.13]).

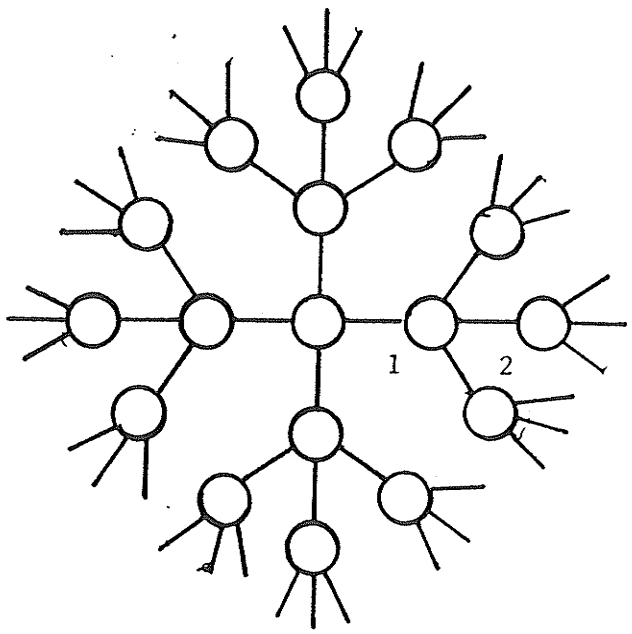

Fig. 4.2 A cluster of the form of the Bethe Lattice. Shells 1 and 2 are indicated. Shell 2 has 12 atoms and 36 bonds are external to the cluster.

(a)

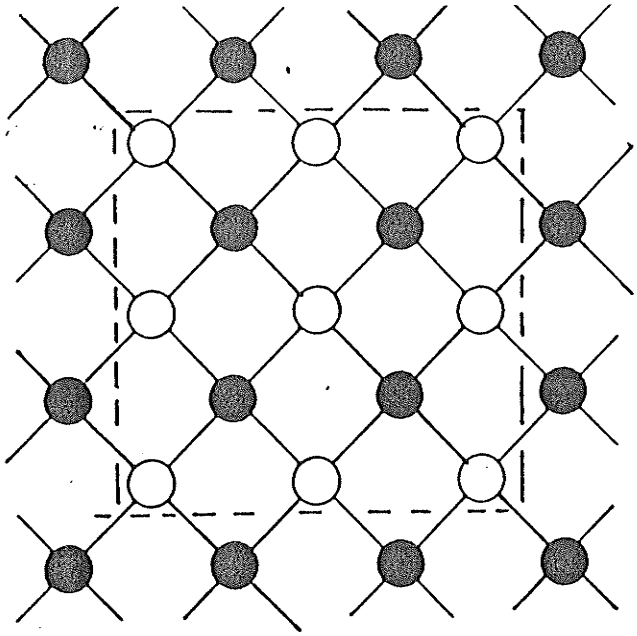

(b)

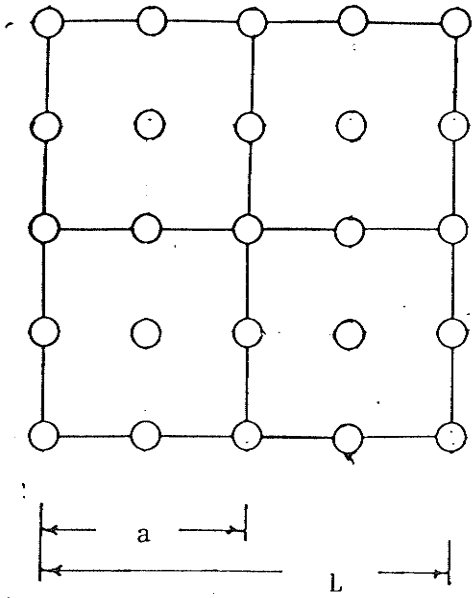

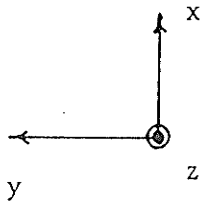

Fig. 4.3 View of a tetragonal lattice along the [001] direction. Views along the [100] and [010] directions are identical due to the symmetry of the lattice. A void in the lattice can be created by removing a cube or a unit cell as indicated by the dashed line in (a). A larger void of dimension L=ma, or m^3 stacked unit cells, as shown in (b). In (a), shaded atoms have no bonds that are external to the void created by cutting along the dashed line. These atoms are omitted in (b) for clarity.

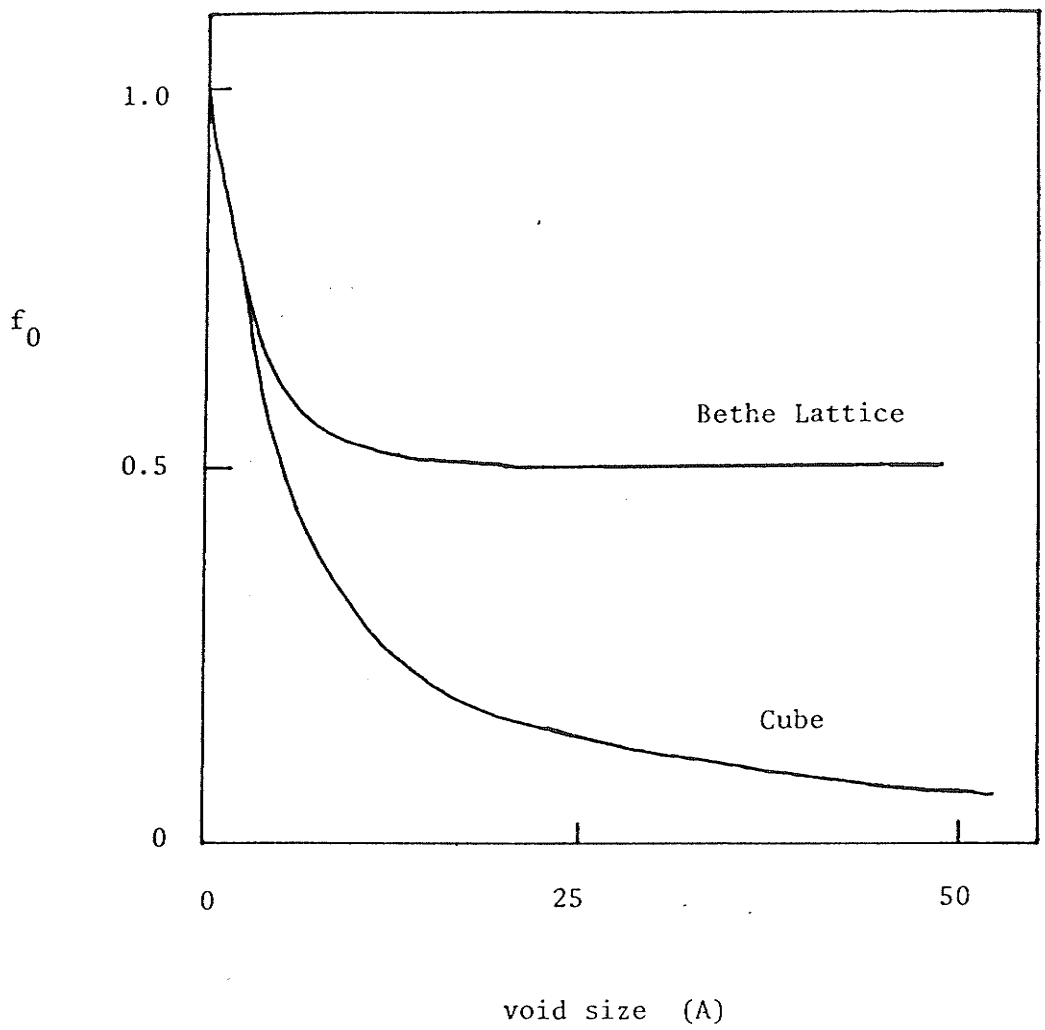

Fig. 4.4 The parameter f_0 defined in Eqn(4.23) for voids formed by removing clusters from a Bethe Lattice (BL) and removing cubes from a tetragonal lattice. Void size is calculated as 2sr for the BL case and ma, where m is an integer, for the cube case. The bond length, r, and lattice constant, a, for Si are taken as 2.35 A and 5.43 A, respectively. The parameter s, is the number of shells for the BL cluster.

CHAPTER 5

COMPARISON BETWEEN EXPERIMENT AND MULTILAYER OPTICAL MODELS

In this chapter, we apply the multilayer optical modelling technique described in Chapter 4 to the microwave glow-discharge grown a-Si:H and μc-Si:H films described in Chapter 3. The correlation between the optical and structural properties is facilitated by modelling the films as multilayer structures of various compositions within an effective medium approximation to extract volume fractions of voids, amorphous, and microcrystalline phases. These results are then compared with X-ray diffraction data.

For convenience we reproduce Figs. 3.1, 3.3, and 3.4 as Figs. 5.1, 5.2, and 5.3 here. Fig. 5.1 shows the X-ray diffraction patterns for the μc-Si:H films, with the diffraction peak corresponding to the (111) plane being observed at $2\theta \simeq 28.5°$. As discussed in Chapter 3, the volume fraction of microcrystallites is estimated from diffraction lines before and after thermal crystallization of the films. Fig. 5.2 shows the imaginary part of the dielectric constant spectra, ϵ_2, as a function of photon energy. As the film changes from an amorphous to a microcrystalline structure, the low energy tail of the ϵ_2 spectrum is suppressed, the development of the shoulder near 3.4 eV occurs, and a peak appears to form at an energy above the initial 3.25 peak position. Similar behavior occurs in the n spectra, as shown in Fig. 5.3. The refractive index spectrum for the amorphous film has a broad maximum near 2.5 eV.

As a transition to microcrystalline structure occurs, the refractive index at 2 eV decreases and the peak at 2.5 eV disappears. A further increase in rf_v results in a peak reappearing, but shifted to a higher energy at 3.25 eV.

5.1 First-Order Approximation

5.1.1 Application of Multilayer Optical Models to Silicon Films

We now attempt to model the silicon films as described earlier, where we will at present neglect second order effects described in section 4.2. The data of Aspnes and Studna[5.1] are used for the reference dielectric function of c-Si, while that of Bagley et al[5.2] was used for dense a-Si:H. This data is chosen since it represents the apparent limiting value of the maximum in the ϵ_2 spectrum ($\epsilon_2 \simeq 29$) and hence should be most representative of dense bulk a-Si:H. The films are modeled in one and two layer models, each layer consisting of volume fractions of amorphous silicon, crystalline silicon and voids. Table 5.1 shows the best fit of a one layer model (including confidence limits) for films A to D. It can be seen that the films are amorphous as calculated from optical data. Adding another parameter to the bulk layer, or more specifically a possibility of c-Si in the bulk, does not improve $\hat{\sigma}$. In fact $\hat{\sigma}$ increases, hence the addition of this parameter is not justified. In addition, for this case, the best fit to the experimental data occurs for zero volume fraction of c-Si. In light of these two factors, films A to D may be considered amorphous. The results of two parameter bulk layer models for films E and F are also given in Table 5.1. In this a three parameter bulk layer model is justified. An improvement in $\hat{\sigma}$ is

observed without drastic increases in the confidence limits of the parameters, hence this model is justified. These films therefore consist of mixed phases of a-Si and c-Si. From the one layer model we see that the X-ray diffraction analysis has overestimated the volume fraction of crystallites as shown in Table 5.2. Only films E and F can be modelled with a non-zero volume fraction of microcrystallites. For film E, we have $rf_v = 0.42$ and $rf_v' = 0.20$, where rf_v' is the relative volume fraction as determined by the optical model[ie, $rf_v' = 0.10/(0.10+0.41)$ for film E]. For film F, we have $rf_v = 0.77$ whereas $rf_v' = 0.42$.

Progressing to a two layer model for films A to D provides a better fit to the experimental data. The error or $\hat{\sigma}$ has been reduced without drastic increases in the confidence limits as shown in Table 5.3, in justification of the two layer model. In general, the films can be described as a low density material, film A containing approximately 20% voids. From the model calculations, film A has an 80 A surface roughness layer. The transition to microcrystallinity is accompanied by an increase in the surface roughness or transition layer thickness to about 150 to 225 A. Going to a two layer model for films E and F gives no significant improvement in $\hat{\sigma}$, hence these films represent a relatively sharp interface with the ambient and have considerably less surface roughness. The transition to μc-Si:H is manifested as a loss of the peak in n at 2.5 eV due to the increase in surface roughness. Figures 5.4 and 5.5 shows how well the model fits the experimental or pseudo-optical constants for films A and C.

In the IR absorption spectrum of glow discharge μc-Si films, the main absorption band for the SiH stretching mode is near 2000 cm^{-1}. Fig. 5.6 shows the IR absorption spectra for film A, that representative of films B to E, and film F. The absorption at 2090 cm^{-1} has been attributed to SiH_2 and/or SiH_3 groups[5.3]. From Fig. 5.6 it can be seen that in film A, $rf_v = 0$ and most of the hydrogen is bonded as Si-H. The IR spectra representative of films B to E, which are slightly microcrystalline, indicates a substantial amount of hydrogen bonded as $Si-H_2$. Film F with rf_v = 0.77 also has a significant amount of hydrogen bonded as $Si-H_2$ but relatively less than that of films B to E. The initial transition to microcrystallinity is accompanied by an increase in the amount of bonded hydrogen, much of which is bonded as $Si-H_2$. As the material becomes more microcrystalline the amount of hydrogen bonded as $Si-H_2$ and Si-H, may reach a limiting value which is lower than that during the initial transition. The large concentration of hydrogen induces an increase in the microstructure and void content, in addition to modifying the dielectric function of the bulk material itself.

The energy levels of hydrogen bonded as Si-H or $Si-H_2$ in a-Si are more than 4 eV below E_v[5.4]. With respect to the dielectric function we would thus expect that, at least up to $\simeq$ 6 eV, the presence of hydrogen behaves as a void fraction. Microcrystallinity is known to be accompanied by hydrogen bonded as $(Si-H_2)_n$ around the crystallite regions[5.5,5.6]. Therefore the void content may be thought of as the volume fraction of void and that of $(SiH_2)_n$ in the material.

The density of film F was determined by floating a small fragment of the sample removed from the substrate in a mixture of zinc bromide and water, the density of the solution being varied by the addition of appropriate amounts of solute. The density of film F was found to be $\simeq$ 2 g/cm^3,corresponding to a void fraction of $\simeq$ 15% based on a value of 2.33 g/cm^3 for dense a-Si. The difference between this value and the model calculation which is of $\simeq$ 30%, is due to the effect of the dielectric function of SiH_2. In view of the definition of the dielectric function as the dipole moment per unit volume, we are in essence measuring the density of polarizable species or Si-Si bonds in silicon films. Since, as discussed previously, Si-H bonds tend to simulate the dielectric function of voids, we can suppose that the residual 15% void volume fraction is actually due to the effect of the Si-H bonds. Of the 85% solid matrix in film F, 15% behaves as a void matrix. Assuming both Si-Si and Si-H bonds occupy essentially the same volume, $N_H/N = 0.15/0.85 = 0.18$, N_H and N being the number of Si-H and total number of bonds (Si-H and Si-Si), respectively.

For a total of T Si and H atoms, the number of Si-H bonds, N_H, is simply $P_H T$, where P_H is the atomic fraction of H atoms. The total number of bonds N is therefore

$$N = (P_s T - P_H T)\frac{Z}{2} + P_H T\frac{Z-1}{2} + P_H T \quad , \tag{5.1a}$$

or

$$N = \frac{Z}{2}P_S T + \frac{1}{2}P_H T \quad , \tag{5.1b}$$

where P_S is the atomic fraction of Si atoms. In these equations we have assumed that $P_H < P_S$, that all the Si atoms have coordination number Z, and that all hydrogen is bonded as Si-H. If all hydrogen forms dihydrides (SiH_2), we obtain the same result for N, or explicitly

$$N = (P_S T - \frac{P_H T}{2})\frac{Z}{2} + \frac{P_H T}{2}\frac{Z-2}{2} + P_H T \quad , \tag{5.1c}$$

which reduces to Eqn.(5.1b). Thus we have

$$\frac{N_H}{N} = \frac{2P_H}{ZP_S + P_H} \quad . \tag{5.2}$$

With $P_S = 1 - P_H$, solving for the atomic fraction of hydrogen gives,

$$P_H = \frac{Z(N_H/N)}{2 + (Z-1)(N_H/N)} \quad . \tag{5.3}$$

If $Z = 4$, or the Si atoms are four-fold coordinated, and $N_H/N = 0.18$, we then obtain $P_H = 0.28$, or 28 at.% hydrogen in film F.

5.1.2 Discussion

Although oxygen is readily adsorbed on c-Si, in general, oxygen is not adsorbed onto a-Si:H to any significant extent. The reactivity of c-Si is mainly due to unsaturated surface states (dangling bonds) which are available to form Si-O bonds. In a-Si:H these states are already saturated with hydrogen. However, the degree of oxidation of a-Si:H may depend significantly on preparation conditions. Oxidation can

depend on how H is bonded (polyhydride vs. monohydride) and in fact O can be bonded as Si-H-O in which oxygen is not bonded directly to silicon[5.7]. Material deposited at low substrate temperature, particularly that with columnar morphology, can in some instances undergo surface (internal or external) oxidation leading to significant oxygen concentrations[5.6,5.8]. Irrespective of the fact that the oxidation rate of a-Si:H may be minimal even for less than ideal a-Si:H, we consider the possibility of a non-zero volume fraction of silicon oxide in our films.

We consider SiO_2 in the surface layer only, since no Si-O vibrational modes were observed in the IR absorption spectra and hence we do not expect any significant content of SiO_2 in the bulk. Allowing the surface layer to contain SiO_2 in addition to a-Si,c-Si and voids does not improve $\hat{\sigma}$ significantly. In those cases where $\hat{\sigma}$ did improve, however slightly, the confidence limits of the model parameters became large. An SiO_2 layer in addition to the surface and bulk layers (ie. a 4 phase model) also does not improve $\hat{\sigma}$. There is no evidence for significant amounts of SiO_2 in these films even though they may possess significant columnar morphology. We do note, however, that the presence of SiO_2 may be difficult to detect in our case since our optical measurements are limited to below 3.5 eV. Also we have not investigated the possibility of nonstoichiometric oxides.

The correlation of the film properties with deposition parameters has been discussed previously[5.9-5.11]. Although the relationship between film properties and deposition parameters is difficult to interpret, we find that in general the degree of microcrystallinity can be controlled by suitable adjustment of deposition parameters.

At magnetic fields above electron cyclotron resonance (ECR) and low absorbed power (≃ 1 W), films are amorphous. At fields below ECR, films tend to be microcrystalline. Results from deposition of Si by chemical transport indicate that stable nuclei for microcrystalline growth are likely when plasma conditions are such that a chemical equilibrium is approached at the plasma-solid interface, $SiH_x(g) \rightarrow Si(s) + xH(plasma)$ [5.12,5.13]. Hydrogen dilution of the SiH_2/H_2 gas mixture (enhancing the reverse reaction and thereby reducing the deposition rate) to approach equilibrium would promote microcrystalline formation. Osaka et al.[5.14] have found that microcrystalline films produced by RF plasma are indeed associated with lower deposition rates as compared to a-Si:H films. However, we observed the opposite trend, films being microcrystalline at higher deposition rates as compared to amorphous films.

Considering the IR absorption data shown in Fig. 5.6, we have previously stated that films B to E have the largest concentration of H bonded as SiH_2. Although there is some contention to the assignment of the absorption at 2090 cm^{-1}, we have interpreted this absorption band as due to SiH_2. The occurrence of the absorption doublet at 840 cm^{-1} and 940 cm^{-1} is often taken as confirmation of the SiH_2 stretching mode at 2090 cm^{-1} and is employed here. Fig. 5.6 shows that films B to E have the most pronounced 840 cm^{-1} absorption band. More pronounced columnar morphology has been linked to increases in absorption in the 840 cm^{-1} band[5.8], therefore columnar morphology is most prevalent in films at the onset of microcrystallization due to the initial nucleation of crystallites. This is consistent with optical model calculations where these films have the lowest density. Large H concentrations in films of low rf_v may act as a hindrance to the coalescence of initially nucleated

crystallites leading to increased columnar morphology. This can be envisioned if surface bonds on the periphery of these crystalline growth sites are quickly satisfied by H. Films of increasing volume fraction of crystallites (specifically E and F) present a sharper interface with the ambient, as indicated by model calculations, due to a lower degree of columnar structure associated with a lower H content, and material densification associated with a more fully developed network. Perhaps there are optimum concentrations of H and SiH species at the film surface for microcrystallite growth. An excessive increase in H radical concentration via hydrogen dilution (in an attempt to fabricate μc-Si:H) or adjustment of other deposition parameters may result in an increase in the surface reaction $SiH + H \rightarrow SiH_2$. This then creates phase boundaries and hinders proper development or coalescence of the growth network. The conditions of growth for films E and F may be near this optimum point. However, the mechanisms controlling hydrogen incorporation into our films as related to deposition parameters have not yet been firmly established.

The density of film F was determined to be approximately 2 g/cm^3. Films B to E may be of lower density, although not as low as optical model calculations since these films contain more H which tends to behave as voids. Most a-Si:H films have densities in the range 1.90 to 2.33 g/cm^3, although some films have been reported with densities as low as 1.40 g/cm^3[5.15,5.16].

Low density material and the relatively thick surface roughness or transition layer of films B to D may not be surprising in view of high H content, columnar growth, and large crystallite grain size. Hydrogen has been known to induce film

microstructure. As H content increases from 0 to 20 at. %, the density of sputtered a-Si:H films decreases from approximately 2.3 g/cm^3 to 2 g/cm^3[5.17] although glow discharge a-Si:H films may not show this reduction. Leadbetter et al.[5.18] have suggested that the intercolumnar spaces are in fact empty, that is, true voids. Crystallite grain sizes in these films have been determined to be of the order of 200 A from the full width at half-maximum of the (111) diffraction peak using Scherrer's formula[5.19].

Film A may contain a void density of 20% as given in Table 5.3. As the films initially become microcrystalline, an increase in hydrogen content and hydrogen bonded as Si-H_2 induces an increase in void content and also reduces the dielectric function. This results in the reduction of n and ϵ_2. As the material microcrystallinity further increases, the amount of hydrogen bonded as Si-H_2 may be reduced and this, together with material densification, results in the increase in n and ϵ_2.

Mishima et al.[5.20] have reported a volume fraction of crystallites of about 0.65 associated with a room temperature dark conductivity σ_{RT}, of 10^{-4} (ohm-cm)$^{-1}$ for RF glow discharge produced μc-Si:H films. Spear et al.[5.21] have reported a limiting value of $\sigma_{RT} = 10^{-2}$ (ohm-cm)$^{-1}$ for μc-Si:H as compared to $\sigma_{RT} = 10^{-8}$ (ohm-cm)$^{-1}$ for a-Si:H RF glow discharge films. For films A to F we obtain $\sigma_{RT} \leq 10^{-6}$(ohm-cm)$^{-1}$. This suggests that $rf_v = 0.77$ for film F is an overestimation. From optical data we have $rf_v' = 0.42$ which is in better agreement with previous reports when σ_{RT} is considered.

Films E and F can be described in a one layer model, giving a good fit between experimental and calculated results. Why then is $\hat{\sigma}$ for film F significantly larger than $\hat{\sigma}$ obtained for film A? The reason is illustrated in Fig. 5.7, where the model calculations show good agreement with experimental data except near 3.4 eV. The agreement on 2 to 3.4 eV is sacrificed if the model parameters are adjusted to improve the fit at 3.4 eV. Model calculations show that the inclusion of a surface layer for films E and F will shift the dielectric spectra to lower energy. Since the experimental spectra are not red shifted with respect to the one layer model calculations, addition of a surface layer in the optical model would not be expected to improve $\hat{\sigma}$, as was the case. The model predicts well the experimental data for both films E and F; it is this particular region near 3.4 eV which accounts for the larger $\hat{\sigma}$. Lack of observation in the experimental dielectric spectra of this sharper feature at 3.4 eV present in the model calculation may be a result of an inability of the effective medium approximation used in predicting the dielectric response of the crystallites embedded in the amorphous matrix. Even though the crystallites are not particularly small ($\simeq$ 200 A), the electronic structure of the crystallites may not maintain bulk crystalline identity. This difficulty would then result in an underestimation of the volume fraction of crystallites. It appears that the true rf_v is bounded above and below by values obtained from X-ray and optical data, respectively.

Generally, films produced on substrates at approximately 250°C and hydrogen contents of <15 at. % are dominated by IR bands at 2000 cm^{-1} and 630 cm^{-1}. Features near 830 to 940 cm^{-1} and a shift in the bond-stretching frequency to higher wavenumber occur together and appear in films with higher bonded H

concentrations and in films depositied on substrates held at lower temperatures[5.8,5.22,5.23]. These features are observed in the IR spectra of our films and also, considering the deposition temperature (150°C), it is not unlikely that film F may contain up to 28 at. % H as estimated. If as is the usual case, about 5 to 10 at.% H is bonded in the amorphous and microcrystalline phases comprising the columns, 18 to 23 at.% H would be bonded in polyhydride configurations around the columns. Film deposition in highly hydrogen diluted gas mixtures to promote microcrystallite formation may enhance the surface reaction SiH + H → SiH_2 as mentioned previously. This would then explain the existence of significant SiH_2 in μc-Si.

Calculation of the H concentration from the integrated intensity of the Si-H wagging band at 630 cm^{-1} using the standard method of Shanks et al.[5.24] yields 6 at.% for film F. This severe underestimation is to be expected, as the presence of large concentrations of Si-H_2 oscillators in μc-Si:H have been found to contribute little to the wagging mode[5.25], due presumably to a very small oscillator strength. Thus IR absorption is not presently a reliable indicator of the total H content of μc-Si:H films, a conclusion shared by other researchers[5.25].

5.1.3 Conclusions

The transition from amorphous to microcrystalline Si:H is accompanied by a change in the refractive index spectra, specifically the loss of the peak in n near 2.5 eV. This is a result of an increase in surface roughness or in transition layer thickness accompanied by an increase in hydrogen bonded as SiH_2 and a reduction in

material density. After this transition, the films may be thought of as having a relatively sharp interface with the ambient which nevertheless exhibits a low density. The low values of ϵ_2 can not be accounted for by a single thin overlayer but must be due to low density bulk layers. The degree of microcrystallinity of the films appear to be between the values obtained from X-ray diffraction measurements and optical model calculations.

Non-destructive depth profiling can be achieved by spectrally resolved ellipsometry due to the variation of penetration depth of the incident light with wavelength. In addition to information on degree of crystallization in microcrystalline films, we can characterize oxide overlayers and surface microroughness. We conclude that spectrally resolved ellipsometry combined with X-ray diffraction measurements provide powerful phenomenological information to optical models of mixed phase thin films.

5.2 Effects of Voids, Bond Length Dilation, and Bond Angle Variation

5.2.1 Application of Multilayer Optical Models to Silicon Films

We now consider the effects the pertubations described in section 4.2 have on the optical model calculations. Let us consider film F as discussed in section 5.1, where we have measured $\rho/\rho' = 1/0.85$, or $F = 0.15$. Assume $f_0 \simeq 0.25$ from Fig. 4.4, $f_B \simeq 1$, and $r/r' = 1/1.01$, the dilation estimated from the position of the (111) peak obtained from X-ray diffraction measurements[5.26]. These values in Eqn(4.28)

give c_e = 1.126. The value of c_a is calculated according to Eqn(4.31), where we assume $N_a'/N_a \approx (r'/r)^{-3}$ and that $n_{eff}' = n_{eff}$. The effective number of electrons is assumed to be unchanged since removal of a cluster in creating a void still leaves the electron occupying the resultant internal surface dangling bond as a participant in optical transitions. We then calculate c_a = 1.231. Using these scaling parameters we now calculate ϵ of a-Si:H' according to Eqn(4.8) and Eqn(4.37).

Table 5.4 shows the results of a one layer model calculation, outlined in Chapter 4, using the calculated dielectric constant of a-Si:H' as a reference for the amorphous Si matrix. The effect of a more self consistent approach in modelling the μc-Si:H films is that rf_v', the relative volume fraction of crystallites, has increased and this may be a more accurate estimation of the true rf_v, at least for film F. It should be noted in Table 5.4 that we have used the same scaling parameters, as calculated from the density measurement of film F, for all the films. Ideally, we would calculate the scaling parameters for each film individually from their respective densities. Unfortunately, only density data for film F was available.

5.2.2 Discussion

For film F we have used F = 0.15 and f_0 = 0.25; this then gives Z' = 3.82 if the original a-Si:H phase had Z = 4. For sputtered a-Si:H, Z is reduced from $\simeq$ 3.9 for high density material to $Z \simeq$ 3.3 for an $\simeq$ 15% density deficit[5.27]. For rf glow discharge a-Si:H, Z varies from 3.9 to 3.6 for density deficits of 0 to 5%[5.27]. Using a value of $f_B \simeq 1$ is not unreasonable in view of the fact that annealing studies of

a-Si:H show on the order of only $\simeq$ 7% reduction in bond angle variation after temperature treatment. Effects of hydrogen concentration have not been considered, where high H content could reduce Z. In calculating c_e we included only the effect of density reduction. If high H content reduces Z further, E_g' shifts still further to low energy and c_e increases. However, if most H is bonded on the outside of the μc-Si columns, Z will not be decreased significantly.

In calculating the effects of voids, we have obviously neglected the fact that once an atom cluster is removed there can be bond rearrangement of the resulting network. The effect of void content on reduction of Z would then be overestimated. However, we have chosen f_0 to be in the mid-ground between the two possible extremes shown in Fig. 4.4. The scaling of the original a-Si:H dielectric function has not included any broadening in the ϵ_2 spectrum. A mathematical formulation to include some broadening due to "increased disorder" should provide even better information on structural aspects of a-Si:H and μc-Si:H films through optical measurements.

5.2.3 Conclusions

With low H content a-Si:H and μc-Si:H films such that effects of H content on optical data are minimal, we can obtain self consistency in void content estimated from optical model calculations and density measurements. This will then give us more accurate estimates of the correct scaling parameters c_a and c_e. Also we can require self consistency with X-ray diffraction and scattering measurements. X-ray

small angle scattering measurements can be used to substantiate density estimates. In addition, integration of the radial distribution function obtained from X-ray diffraction, would give us values of the coordination number. This in turn provides us with a means of determining void sizes and size distributions. By making optical, density, and X-ray diffraction data completely self consistent, we can obtain good estimates of volume fractions of the a-Si:H, μc-Si:H, and void phases in addition to information on void size distribution.

References

[5.1] D.E. Aspnes and A.A. Studna, Phys. Rev., **B27,** 985 (1983).

[5.2] B.G. Bagley, D.E. Aspnes, A.C. Adams, and F.B. Alexander Jr., Bull. Am. Phys. Soc., **25,** 12 (1980).

[5.3] Topics in Applied Physics, vol. 56, "The Physics of Hydrogenated Amorphous Silicon II, Electronic and Vibrational Properties", J.D. Joannopoulos and G. Lucovsky Ed., Springer-Verlag, 1984, p. 333.

[5.4] In ref. 5.3, p 90.

[5.5] A. Matsuda, T. Yoshida, S. Yamasaki, and K. Tanaka, Jpn. J. Appl. Phys., **20,** L439 (1981).

[5.6] J.C. Knights, Jap. J. Appl. Phys., **18,** suppl. 18-1, 101 (1979).

[5.7] L. Ley, H. Richter, R. Karcher, R.L. Johnson, and J. Reichardt, J. Phys. (Paris), C4 **42,** 753 (1981).

[5.8] G. Lucovsky, R.J. Nemanich, and J.C. Knights, Phys. Rev. B, **19,** 2064 (1979).

[5.9] S.R. Mejia, R.D. McLeod, W. Pries, P. Shufflebotham, D.J. Thomson, J. White, J. Schellenberg, K.C. Kao, and H.C. Card, J. Non-Cryst. Solids, **77,78,** 765 (1985).

[5.10]S.R. Mejia, R.D. McLeod, K.C. Kao, and H.C. Card, Rev. Sci. Instr., **57,** 493 (1986).

[5.11]J.J. Schellenberg, R.D. McLeod, S.R. Mejia, H.C. Card, and K.C. Kao, Appl. Phys. Lett., **48,** 163 (1986).

[5.12]S. Veprek, Chimia, **34,** 489 (1980).

[5.13]S. Veprek, Z. Iqbal, H.R. Oswald, and A.P. Webb, J. Phys., **C14,** 295 (1981).

[5.14]Y. Osaka and T. Imura, "Amorphous Semiconductor Technologies and Devices", Jpn. Ann. Rev. Electron. Comput. Telecommum., Y. Hamakawa, Ed. (North-Holland, Amsterdam, 1984), JARECT, vol. 16, chaps. 2 and 3.

[5.15]M.H. Brodsky, M.A. Frisch, J.F. Ziegler, and W.A. Lanford, Appl. Phys. Lett., **30,** 561 (1977).

[5.16]J.C. Knights, "Structure and Excitations of Amorphous Solids", G. Lucovsky and F. Galeener, Ed., AIP Conf. Proc. No. 34 (AIP, New York, 1976) p. 296.

[5.17]Semiconductors and Semimetals, vol. **21,** "Hydrogenated Amorphous Silicon Part A, Preparation and Structure", J.I. Pankove Ed., (Academic Press, 1984) p. 283.

[5.18]A.J. Leadbetter, A.A.M. Rashid, N. Colenutt, A.F. Wright, and J.C. Knights, Solid State Commun., **38,** 957 (1981).

[5.19]H.P. Klug and L.E. Alexander, "X-ray Diffraction Procedures", (Wiley, New York, 1954) chap. 6.

[5.20]Y. Mishima, S. Miyazaki, M. Hirose, and Y. Osaka, Philos. Mag. B, **46,** 1 (1982).

[5.21]W.E. Spear, G. Willeke, P.G. LeComber, and A.G. Fitzgerald, J. Physique, **42,** C4, 257 (1981).

[5.22]M.H. Brodsky, M. Cardona, and J.J. Cuomo, Phys. Rev. B, **16,** 3556 (1972).

[5.23]J.C. Knights, G. Lucovsky, and R.J. Nemanich, Phil. Mag. B, **37,** 467 (1978).

[5.24]H. Shanks, C.J. Fang, L. Ley, M. Cardona, F.J. Demond, and S. Kalbitzer, Phys. Stat. Sol.(b), **100,** 43 (1980).

[5.25]M. Kumeda, Y. Yonezawa, K. Nakazawa, S. Ueda, and T. Shimizu, Jap. J. Appl. Phys., **22,** L194 (1983).

[5.26]unpublished data.

[5.27]Semiconductors and Semimetals, **21,** "Hydrogenated Amorphous Silicon, Part A: Preparation and Structure", J. Pankove Ed. (Academic Press, 1984) p. 283.

FIGURES AND TABLES

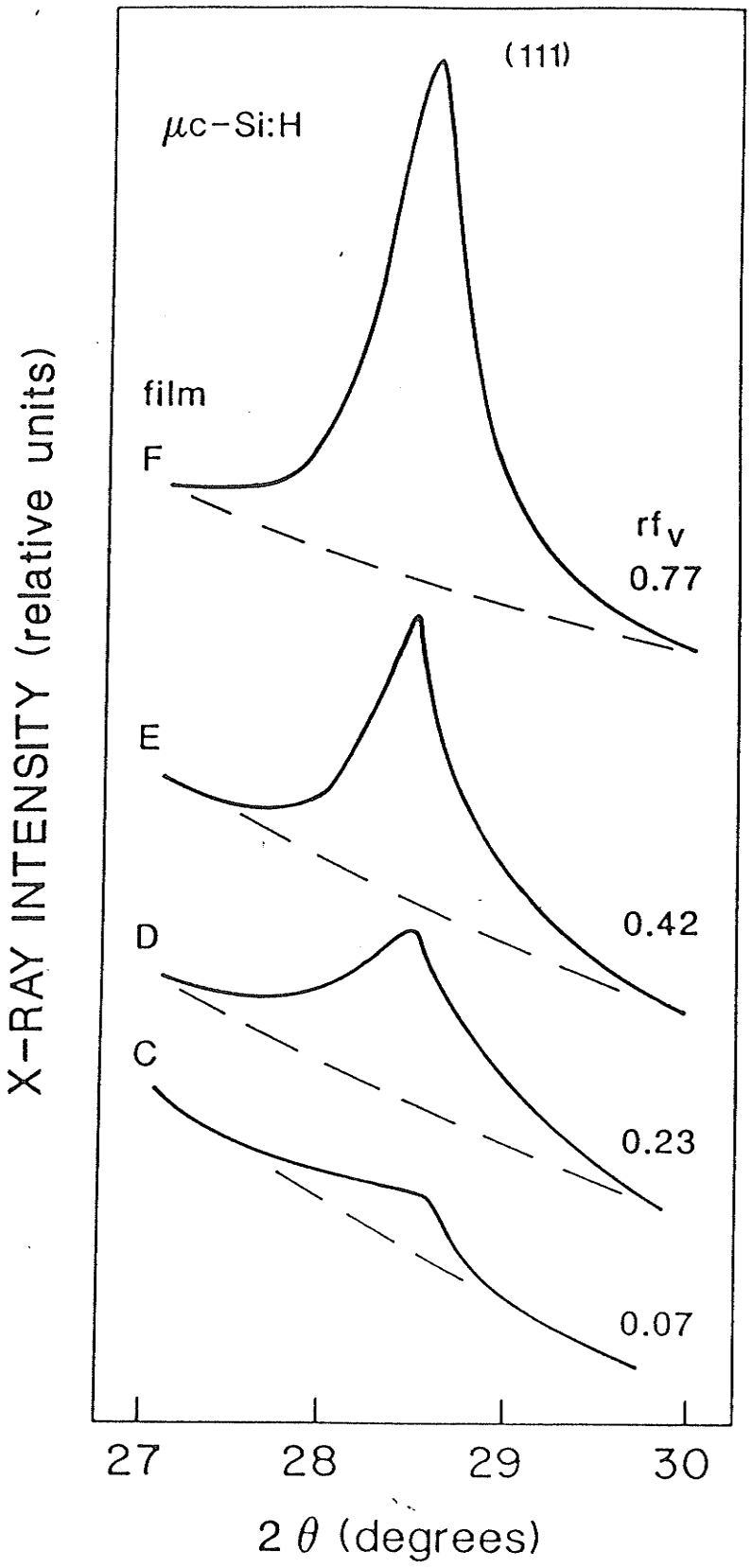

Fig. 5.1 X-ray diffraction profiles for μc-Si:H films. A measure of the relative volume fraction of crystallites rf_v, is indicated.

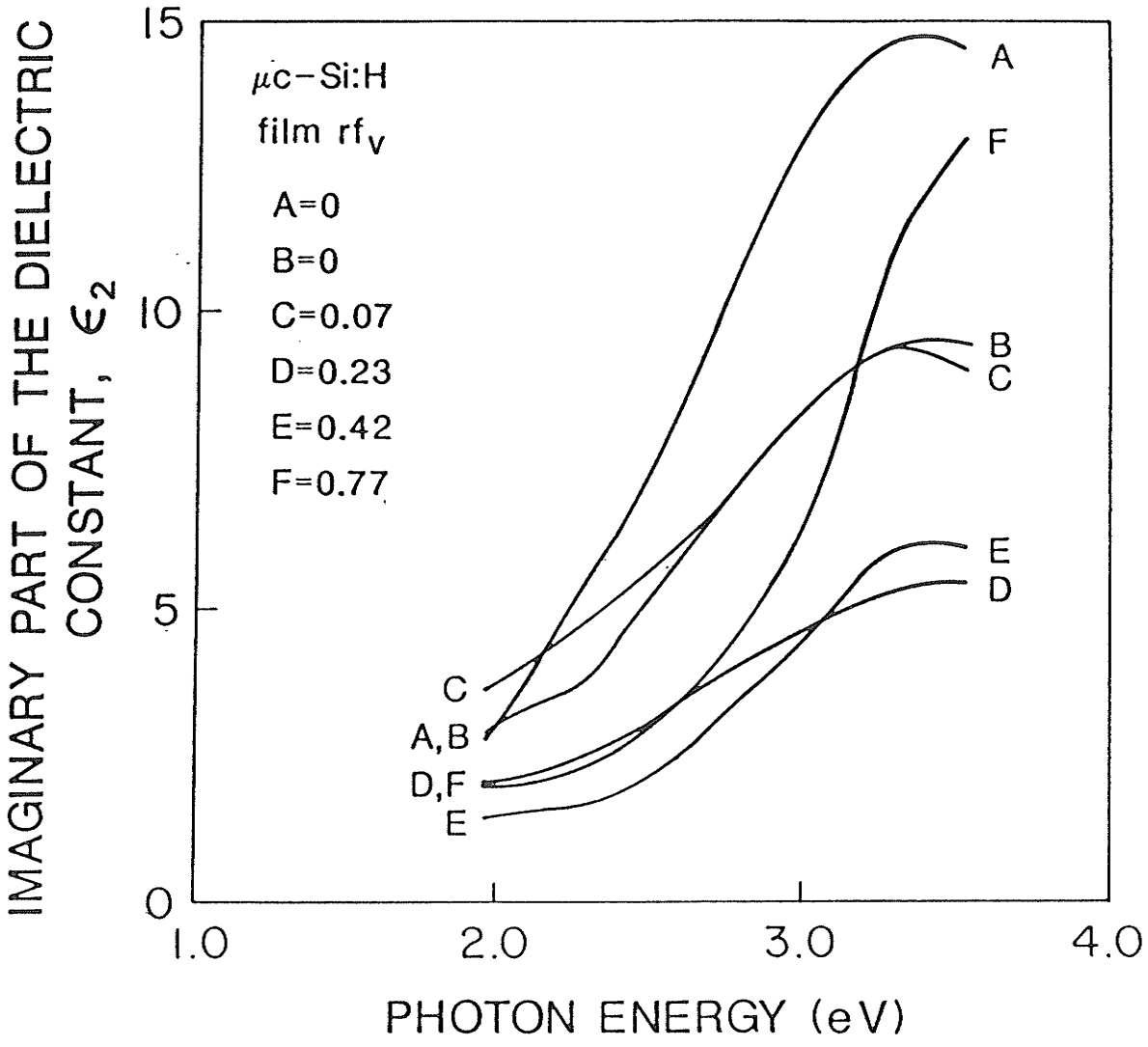

Fig. 5.2 Imaginary part of the dielectric constant versus photon energy for μc-Si:H films with relative volume fraction of crystallites rf_v, as a parameter.

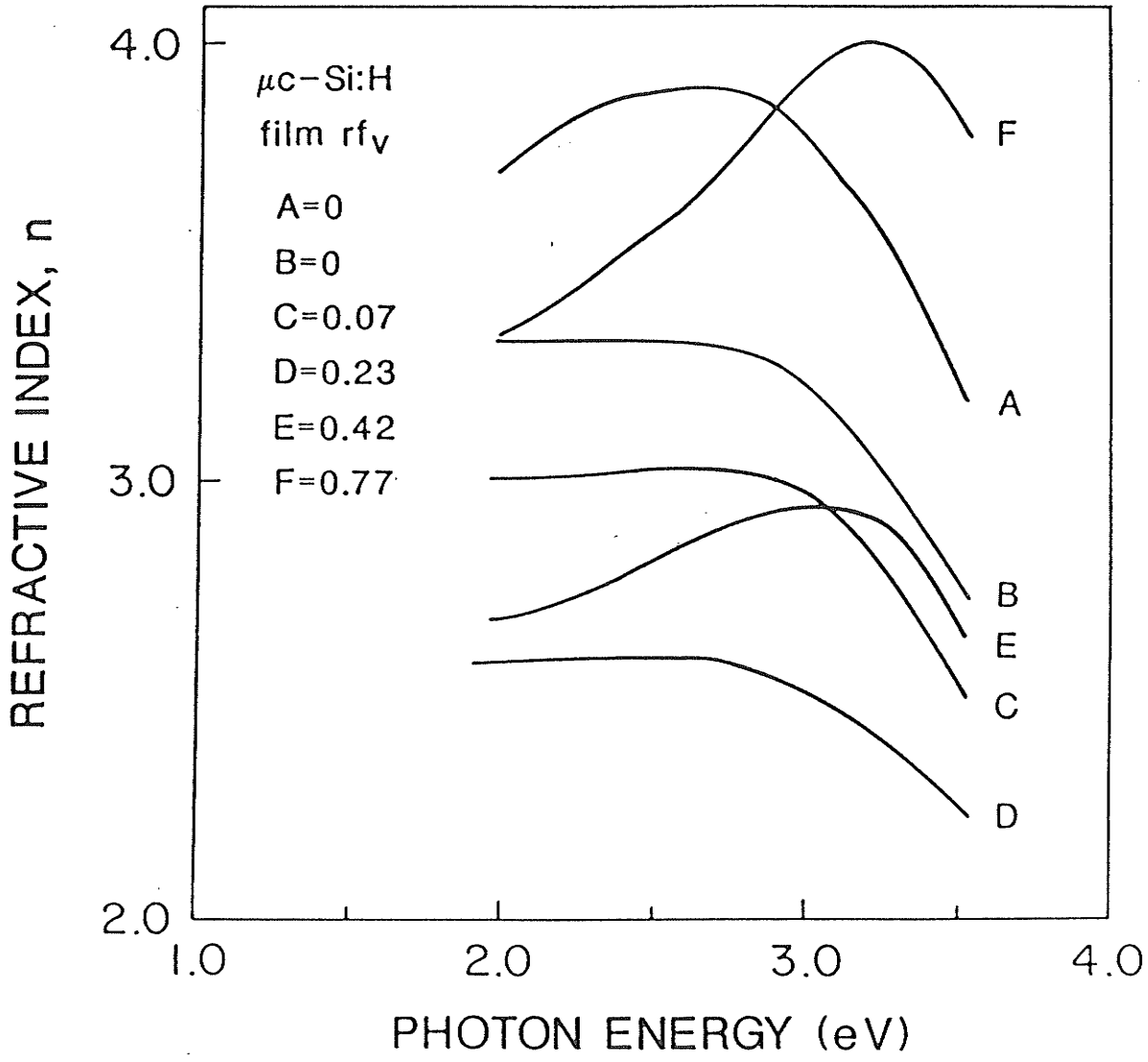

Fig. 5.3 **Refractive index versus photon energy for μc-Si:H films with relative volume fraction of crystallites rf_v, as a parameter.**

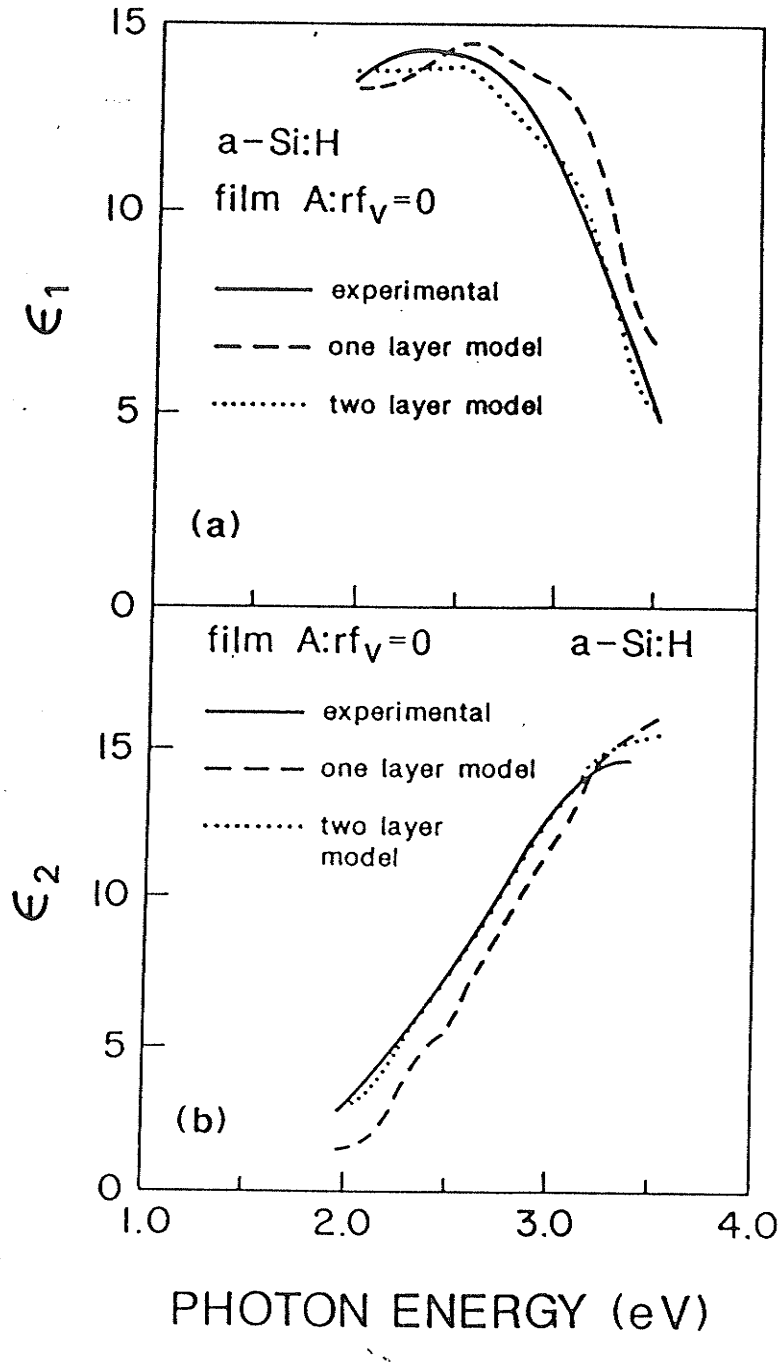

Fig. 5.4 Comparison between experimental and calculated dielectric functions for the best fit one and two layer models, from Tables 5.1 and 5.2, of film A (a-Si:H rf_v = 0). (a) Real part of the dielectric constant, ϵ_1. (b) Imaginary part of the dielectric constant, ϵ_2.

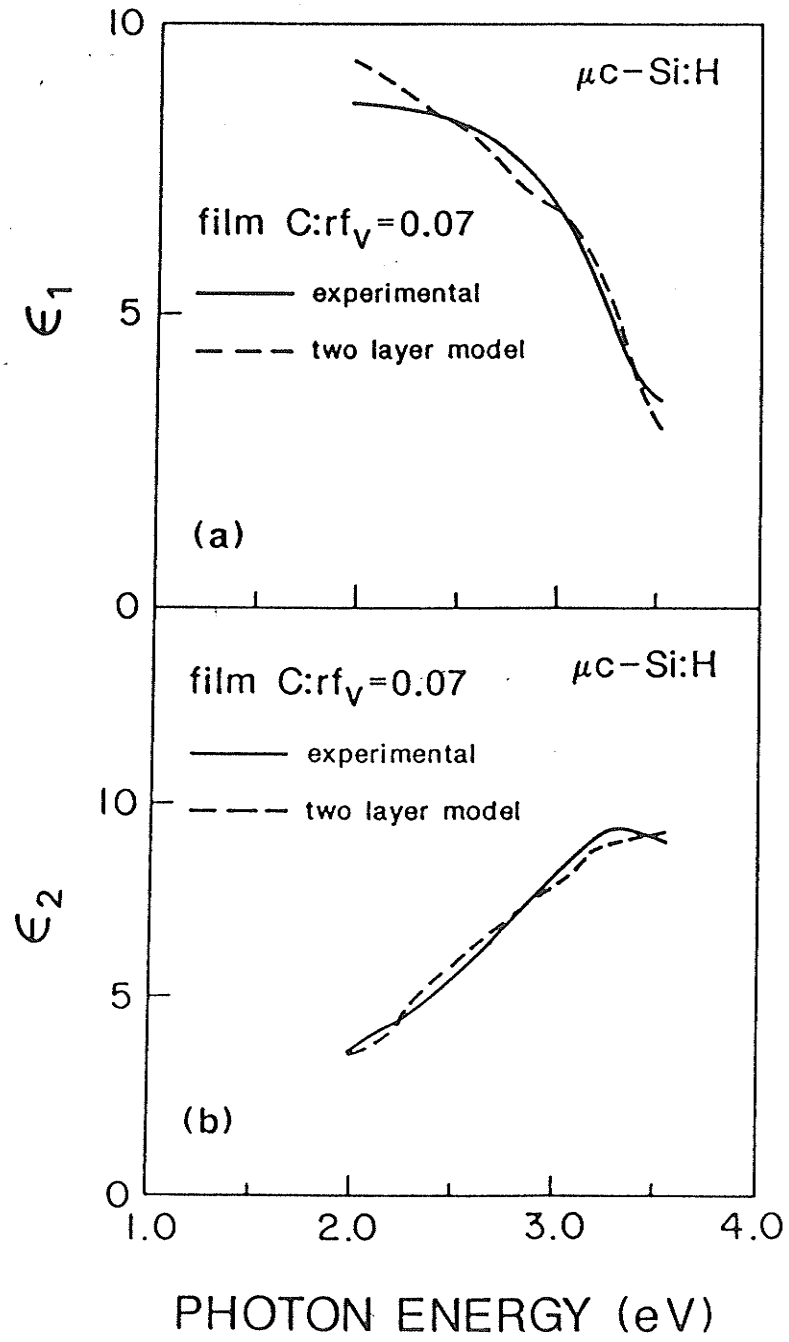

Fig. 5.5 Comparison between experimental and calculated dielectric functions for the best fit two layer model, from Table 5.3, of film C (μc-Si:H rf_v = 0.07). (a) Real part of the dielectric constant, ϵ_1. (b) Imaginary part of the dielectric constant, ϵ_2.

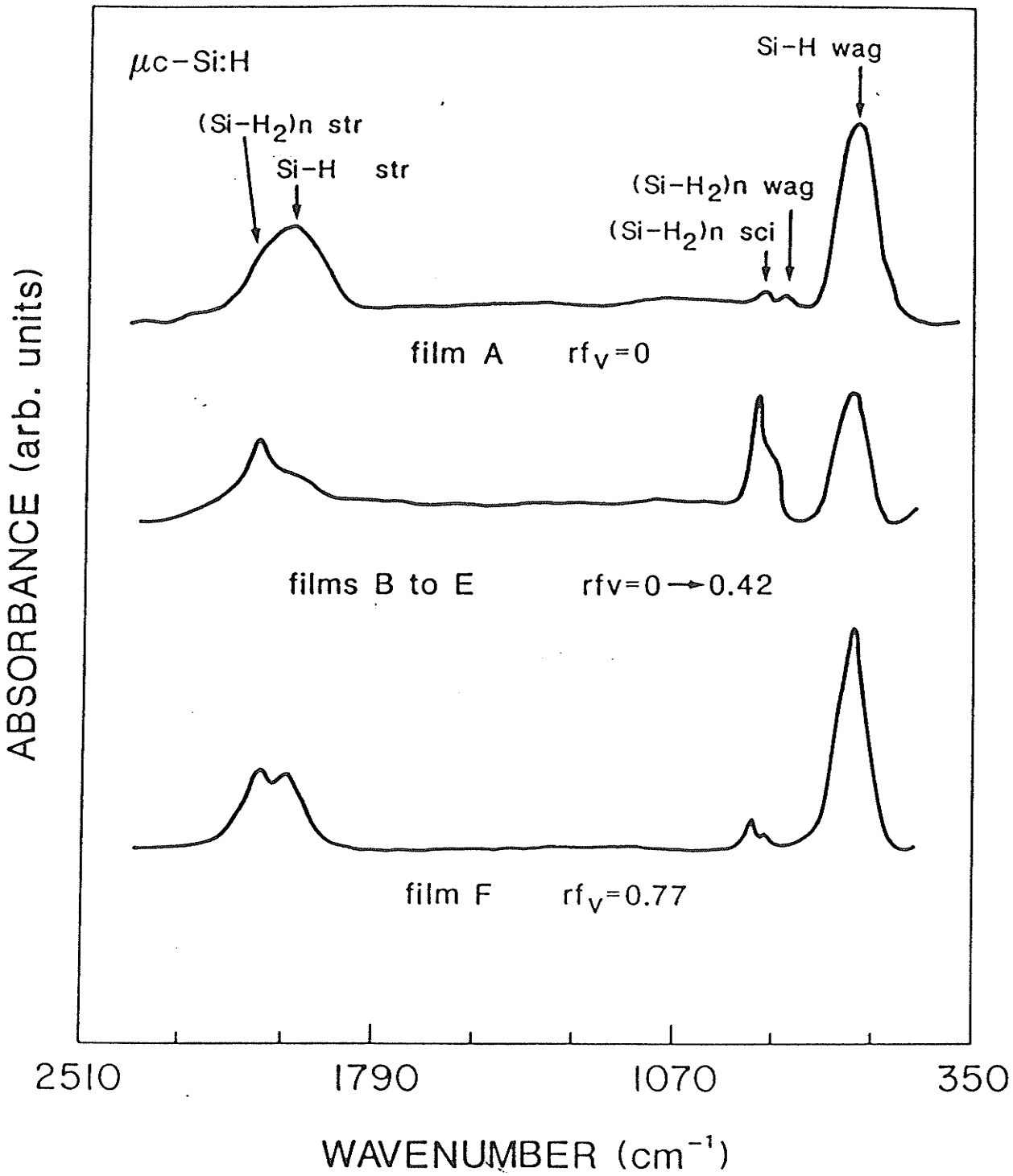

Fig. 5.6 IR absorption spectra of films A, that representative of films B to E, and film F. Absorption bands for monohydride (Si-H) and dihydride ($Si-H_2$) groups are labelled as; str: stretching, sci: scissors, and wag: wagging modes.

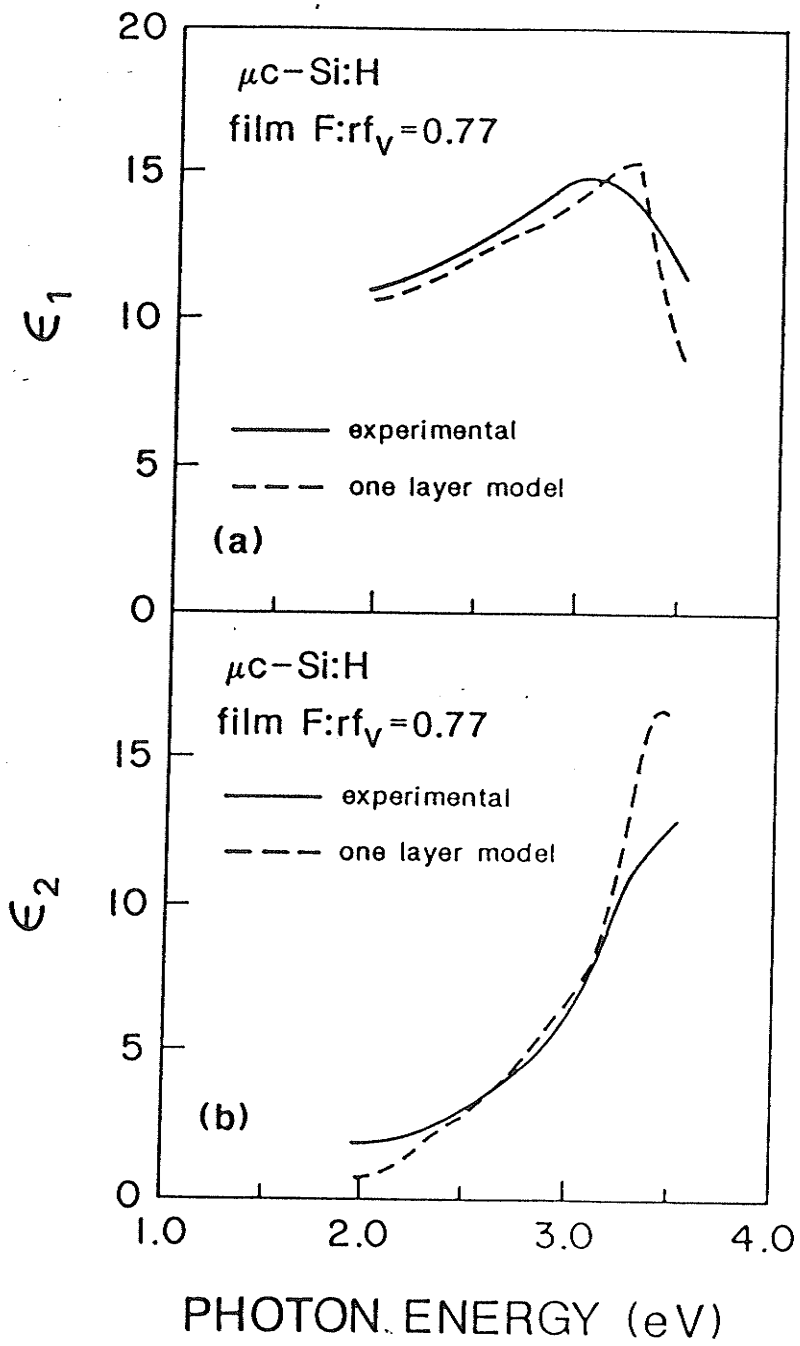

Fig. 5.7 Comparison between experimental and calculated dielectric functions for the best fit one layer model, from Table 5.1, of film F (μc-Si:H rf_v = 0.77). (a) Real part of the dielectric constant, ϵ_1 (b) Imaginary part of the dielectric constant, ϵ_2.

Table 5.1. The model parameters and confidence limits of the best fit two and three parameter one layer models for various a-Si:H films. The parameter rf_v is the relative volume fraction of crystallites and $\hat{\sigma}$ is a measure of the fit between model and experimental results.

film	rf_v	bulk layer (two parameter)	$\hat{\sigma}$	bulk layer (three parameter)	$\hat{\sigma}$
A	0	0.73 ± 0.01 a-Si 0.27 ± 0.01 void	0.0322	0.73 ± 0.04 a-Si 0.0 ± 0.04 c-Si 0.27 ± 0.08 void	0.0328
B	0	0.60 ± 0.01 a-Si 0.40 ± 0.01 void	0.0365	0.60 ± 0.04 a-Si 0.0 ± 0.04 c-Si 0.40 ± 0.08 void	0.0371
C	0.07	0.57 ± 0.02 a-Si 0.43 ± 0.02 void	0.0679	0.57 ± 0.07 a-Si 0.0 ± 0.07 c-Si 0.43 ± 0.14 void	0.0691
D	0.23	0.47 ± 0.01 a-Si 0.53 ± 0.01 void	0.0435	0.47 ± 0.04 a-Si 0.0 ± 0.04 c-Si 0.53 ± 0.08 void	0.0442
E	0.42	0.52 ± 0.03 c-Si 0.48 ± 0.03 void	0.111	0.41 ± 0.02 a-Si 0.10 ± 0.03 c-Si 0.49 ± 0.05 void	0.0272
		0.51 ± 0.01 a-Si 0.49 ± 0.01 void	0.0360		
F	0.77	0.72 ± 0.03 c-Si 0.28 ± 0.03 void	0.0765	0.39 ± 0.03 a-Si 0.30 ± 0.03 c-Si 0.31 ± 0.06 void	0.0257
		0.68 ± 0.02 a-Si 0.32 ± 0.02 void	0.0607		

Table 5.2. Comparison between the relative volume fraction of crystallites as calculated by x-ray diffraction measurements (rf_v) and optical modelling (rf_v') for various a-Si:H and μc:Si:H films.

film	rf_v	rf_v'
A	0	0
B	0	0
C	0.07	0
D	0.23	0
E	0.42	0.20
F	0.77	0.42

Table 5.3. The model parameters and confidence limits of the best fit two layer models for various a-Si:H and μc-Si:H films. The parameter rf_v is the relative volume fraction of crystallites, $\hat{\sigma}$ is a measure of the fit between model and experimental results, and d is the thickness of the surface layer.

film	rf_v	bulk layer	surface layer	$\hat{\sigma}$
A	0	0.78 ± 0.01 a-Si 0.22 ± 0.01 void	0.68 ± 0.03 a-Si 0.42 ± 0.03 void d = 79 ± 22 Å	0.0101
B	0	0.66 ± 0.02 a-Si 0.34 ± 0.02 void	0.60 ± 0.01 a-Si 0.40 ± 0.01 void d = 163 ± 29Å	0.0195
C	0.07	0.68 ± 0.01 a-Si 0.32 ± 0.01 void	0.56 ± 0.01 a-Si 0.44 ± 0.01 void d = 180 ± 10Å	0.0123
D	0.23	0.52 ± 0.01 a-Si 0.48 ± 0.01 void	0.47 ± 0.01 a-Si 0.53 ± 0.01 void d = 229 ± 16Å	0.0115

Table 5.4 The model parameters and confidence limits of the best fit two and three parameter one layer models for various a-Si:H and μc-Si:H films. The parameter rf_v is the relative volume fraction of crystallites and $\hat{\sigma}$ is a measure of the fit between model and experimental results. For comparison, results for rf_v from Table 5.2 are given in the last column.

film	rf_v	2 parameter bulk layer	$\hat{\sigma}$	3 parameter bulk layer	$\hat{\sigma}$	rf_v'	unscaled rf_v'
C	0.07	0.51±0.01 a-Si 0.49±0.01 void 0.59±0.01 c-Si 0.41±0.01 void	0.0339 0.195	0.49±0.02 a-Si 0.20±0.02 c-Si 0.31±0.04 void	0.0331	0	0
D	0.23	0.42±0.01 a-Si 0.58±0.01 void 0.48±0.01 c-Si 0.52±0.01 void	0.0303 0.163	0.39±0.01 a-Si 0.04±0.02 c-Si 0.57±0.03 void	0.0269	0.09	0
E	0.42	0.45±0.01 a-Si 0.55±0.01 void 0.52±0.01 c-Si 0.48±0.01 void	0.0909 0.111	0.28±0.02 a-Si 0.20±0.03 c-Si 0.52±0.05 void	0.0395	0.42	0.20
F	0.77	0.59±0.01 a-Si 0.41±0.01 void 0.72±0.01 c-Si 0.28±0.01 void	0.127 0.0765	0.30±0.03 a-Si 0.36±0.03 c-Si 0.34±0.06 void	0.0342	0.55	0.42

Chapter 6

EFFECTS OF SUBSTRATE BIAS ON STRUCTURE AND PROPERTIES OF a-Si:H FILMS DEPOSITED BY MICROWAVE PLASMAS'

Microwave plasmas (MW) have been demonstrated to be viable alternatives for the deposition of a-Si:H and μc-Si:H films[6.1-6.3]. The high deposition rates obtained are due to the more complete dissociation of the gas mixture as a result of the more energetic plasma. Electron cyclotron resonance (ECR) MW plasmas allow for the reduction of power requirements, of the order of watts, and also allow a reduced operating pressure (approximately 10^{-3} torr).

Although the correlation of optical and structural properties with deposition conditions has not been fully characterized, it is well known that high quality a-Si:H films are generally prepared at low discharge power densities[6.4] and high substrate temperature. The low power requirements of ECR MW plasmas is thus an attractive feature. The effect of ion bombardment during film growth appears to be an important factor influencing film properties[6.5,6.6]. The effects of ion bombardment on a-Si:H films deposited by rf glow discharge[6.7,6.8] and multipole dc discharge[6.9,6.10] have been reported, where the ion flux and ion energy can be controlled by suitable adjustment of substrate bias and chamber pressure. Ion bombardment in dc discharge grown films promotes densification and homogeneous growth, while these effects are weaker in rf discharge produced films. In this Chapter,

experimental results of the effects of substrate bias on the optical and structural properties of a-Si:H films deposited from an ECR MW plasma are presented.

6.1 Experimental Details

Deposition of a-Si:H occurred in a stainless steel waveguide chamber as described in Chapter 3. Stainless steel and quartz substrates were mounted on a thermostatically controlled table maintained at 250°C and biased from -300 to +100 V, with their surfaces normal to the dc magnetic field. The plasma was kept at a fixed distance from the table, approximately 10 cm, by the magnetic field peak ($\simeq$875 Guass) position. Films were deposited from a SiH_4(10%)-H_2(90%) gas mixture at a chamber pressure of 10^{-3} torr with 4 Watt absorbed microwave power. The plasma was monitored by OES and mass spectroscopy as described previously.

Langmuir probe measurements of a H_2 plasma under the conditions used for deposition, were used to determine plasma parameters. Film growth was monitored "in situ" by laser interferometry and final film thickness is determined from laser interferometry combined with ellipsometric measurement at the He-Ne laser wavelength. Thickness measurement was further supported by mechanical thickness profiler measurement and near infrared spectrophotometry. Film thickness ranged from 1.5 to 2 microns. Samples were characterized over the photon energy range 2 to 3.5 eV using spectrally resolved ellipsometry (SE). X-ray diffraction data was obtained employing Cu-Kα (40 KeV, 20 mA) radiation on $20° < 2\theta < 60°$.

6.2 Results and Discussion

The refractive index, n, and the imaginary part of the dielectric constant, ϵ_2, as functions of photon energy are shown in Fig. 6.1 and Fig. 6.2 for films deposited on stainless steel substrates biased at various voltages. The n and ϵ_2 spectra of films deposited with substrate bias, $V_b \leq$ -100 V, show no significant differences as compared to V_b = -100 V. The n spectrum has a limiting peak value of $\simeq$ 5 and the ϵ_2 spectrum has a limiting peak value of $\simeq$ 28, indicative of high density a-Si:H films as discussed previously. The position of the ϵ_2 peak does not appear to be significantly affected by V_b, indicating little or no effect of bias on surface roughness[6.11]. Both the n and ϵ_2 spectra are enhanced by increasing negative bias over the spectral range from 2.0 to 3.5 eV. All films deposited were determined to be amorphous based on X-ray diffraction measurements.

Fig. 6.3 shows the maximum value of the ϵ_2 spectra, $\epsilon_{2\,max}$, as a function of substrate bias for films deposited on stainless steel and quartz substrates. As suggested in previous chapters, increases in $\epsilon_{2\,max}$ can be mainly related to increased film density. Drevillon et al.[6.9] have shown that in a dc discharge deposition system, the mean ion energy is given by

$$E_{ion} = e(V_p - V_b) \quad , \tag{6.1}$$

where V_p is the plasma potential. The ion energy remains quasi-mono-energetic on the range $0 < V_b <$ -200 V for pressures $\leq$ 5 mtorr. At higher pressures, of 30-100 mtorr typical of rf discharge systems, considerable broadening of the ion energy

distribution occurs due to increased collisions of the ions with neutrals while accelerating; finally reaching the substrate at a relatively low energy. Since our films are deposited at 1 mTorr, we expect the ion energy is quasi-mono-energetic and given by Eqn(6.1) in the case of stainless steel or conducting substrates. In contrast, insulating quartz substrates become negatively self biased with respect to the plasma reactor walls. In this case the ion energy should be determined by the difference between this floating potential V_f, and the plasma potential. Langmuir probe measurements are summarized in Fig. 6.4, where measurements were carried out on a H_2 plasma with all other deposition conditions remaining unchanged. The SiH_4-H_2 (90%,10%) plasma is not significantly different from the H_2 plasma, as indicated by probe data at V_b = -150 V. The quantity $V_p - V_f$ should show the variation of the incident ion energy with substrate bias for the case of the films deposited on quartz substrates. The quantity $V_p - V_b$ in Fig. 6.4, gives the variation of the ion energy with V_b for the metallic substrates.

We see that ion bombardment during film growth results in film densification. For stainless steel substrates, $\epsilon_{2\,max}$ increases on the range V_b = 0 V to -100 V, thereafter remaining constant. For the case of films deposited on insulating substrates, the same behaviour is observed, that is $\epsilon_{2\,max}$ increases with increasing E_{ion}, where now E_{ion} should vary as $V_p - V_f$. An enhancement of the surface mobility of the reactive ion species due to an increase of ion bombardment energy may be responsible for the increase in density. For positive substrate bias, substantial numbers of electrons are drawn from the plasma. To maintain charge neutrality

within the plasma, ions are driven to ground potential, resulting in ion bombardment of the deposition chamber walls. As a consquence, films produced with positive V_b are contaminated with residual material from the chamber wall and are of poor quality. Fig. 6.3 and Fig. 6.4 indicate that high density a-Si:H films can be produced if $E_{ion} \geq 100$ eV.

Infared absorption measurements indicate that films deposited with $V_b < -100$ V contain $\simeq$ 6 at.% H. Films exhibit no absorption peak due to Si-H_2 bonds at 2090 cm^{-1} or any absorption due to Si-O bonds near 1000 cm^{-1}. All H is incorporated solely in a mono-atomic, singly bonded form. This is consistent with high density material as discussed in Chapter 5. Application of the optical modelling technique described in Chapter 4 gives 15% void content for $V_b = 0$ V and decreasing to 0% for $V_b < -100$ V. Lack of ion bombardment during film growth can result in very low density films and significant H bonded as Si-H_2. This is the case for films grown on substrates parallel to the magnetic field,where the field confines the ions and shields the growing film surface from ion bombardment. As we have seen in Chapter 5, films fabricated in this manner were of low density and contained significant amounts of H bonded as Si-H_2. We see now that these properties can be attributed to the lack of ion bombardment during film growth. The scouring action of ionic species on the film surface during growth[6.12] may be responsible for elimination of H bonded as Si-H_2.

Fig. 6.5 shows the variation of the optical gap E_{opt}, with substrate bias for metallic substrates. The optical gap initially increases strongly with negative

substrate bias or E_{ion}. Below $V_b \simeq$ -100 V or $E_{ion} \geq$ 100 eV, the optical gap is not affected by further increases in E_{ion}. A larger E_{opt} is associated with increased density as is seen by comparing Figs. 6.3 and 6.4 where E_{opt} increases with increasing ϵ_{2max}. Similar variation of E_{opt} is found for a-Si:H films deposited on quartz substrates. As E_{ion} increases, film density increases together with E_{opt}.

The deposition rate r_d, as a function of substrate bias is given in Fig. 6.6. As E_{ion} increases initially, r_d increases afterwhich a reduction to a value of $\simeq$ 3.3 A/s at V_b = -300 V occurs for films deposited on metallic substrates. The increase in r_d at low E_{ion} may be explained by an increased surface reaction rate if this reaction is energy activated. Further increases of E_{ion} would reduce the deposition rate due to etching of the growing film surface[6.9]. The deposition rate is weakly dependent on V_b, varying between $\simeq$ 3.6 to 2.25 A/s, the maximum r_d corresponding to the minimum E_{ion} of $\simeq$ 100 eV, required for high density films. For films deposited in quartz, the deposition rate is unaffected by V_b, remaining constant at $\simeq$ 2.25 A/s. Over this bias range E_{ion} does not vary strongly with V_b as shown in Fig. 6.4, and since r_d is weakly dependent on E_{ion}, r_d is approximately constant. Antoine et al.[6.7] have reported deposition rates of 0.5 - 0.9 A/s for -150 V $< V_b <$ 0 V, with r_d = 0.9 A/s at V_b = 0 V, for a-Si:H films fabricated by rf glow discharge.

As discussed in Chapter 2, the B-parameter defined by

$$\alpha h\nu = B(h\nu - E_{opt})^2 \quad , \tag{6.2}$$

is inversely proportional to the width of the tail states and reflects the steepness of

the density of states rise at the band edges. Therefore, this value is related to the quality of a-Si:H films. Fig. 6.7 shows the B-parameter as a function of V_b for a-Si:H films deposited on metallic substrates. The B-parameter behaves in the same manner as E_{opt}, increasing for low ion energies. The extent of the tail states at the band edges decreases with ion energy up to the threshold energy of 100 eV.

Figure 6.8 illustrates the ratio of photoconductivity to dark conductivity, σ_{ph}/σ_d, and σ_d as functions of the substrate bias for both stainless steel and quartz substrates. For films deposited under negative substrate bias typical values of σ_d are seen to be on the order of 10^{-9} (ohm-cm)$^{-1}$ which is comparable to high quality rf glow-discharge films. As anticipated, films deposited under positive substrate bias with poor optical properties also displayed poor electrical properties. The photoconductivity was measured at a wavelength of 6328 A with a photon flux of 10^{15} photons-s^{-1}-cm^{-2}. In a similar manner the films with good optical properties also displayed photoconductivities typical of good quality films.

High density and good optical and electronic grade films with mono-atomic H can be produced at low substrate temperature with some ion bombardment in ECR MW plasmas. Above E_{ion} = 100 eV, film properties are not strongly dependent on E_{ion}.

6.3 Conclusions

Some ion bombardment during film growth is favourable due to enhanced film density and reduction of dihydrides. In addition, the deposition rate is increased slightly with increases of E_{ion}. An enhanced surface mobility of the reactive ion species and an energy activated surface reaction at the growing film surface can explain the increases in density and deposition rate, respectively. Film surface roughness does not appear to be dependent on E_{ion} as evidenced by the constancy of the ϵ_2 peak position with V_b. Increased film density is accompanied by an increase in the optical gap, from 1.55 eV to 1.80 eV, with increased ion bombardment. The tailing of the density of states at the band edges is reduced by a small degree of ion bombardment. The ratio of photo- to dark-conductivity is on the order of 10^5 and is enhanced by moderate ion bombardment.

Fabrication of high density good quality a-Si:H films can be acheived by suitable adjustment of deposition parameters to attain some ion bombardment of the film surface during growth. A moderate amount of bombardment increased the deposition rate, the density, and the optical and electronic quality of the films. Film densification of approximately 15% can be acheived by ion bombardment. The optimum ion energy reguired, appears to be approximately 100 eV in MW plasmas operating at 1 mTorr.

References

[6.1] S.R. Mejia, R.D. McLeod, K.C. Kao, and H.C. Card, Rev. Sci. Instr. **57,** 493 (1986).

[6.2] J.J. Schellenberg, R.D. McLeod, S.R. Mejia, H.C. Card, and K.C. Kao, Appl. Phys. Lett. **48,** 163 (1986).

[6.3] S.R. Mejia, R.D. McLeod, W. Pries, P. Shufflebotham, D.J. Thomson, J. White, J. Schellenberg, K.C. Kao, and H.C. Card, J. Non-Cryst. Solids **77,78,** 765 (1985).

[6.4] J.C. Knights and R.A. Lujan, Appl. Phys. Lett. **35,** 244 (1979).

[6.5] J.A. Reimer, R.W. Vaughan, and J.C. Knights, Phys. Rev. B **24,** 3360 (1981).

[6.6] K.J. Chen and H. Fritzsche, Solar Energy Mater. **8,** 205 (1982).

[6.7] A.M. Antoine, B. Drevillon, and P. Roca I Cabarrocas, J. Appl. Phys. **61,** 2501 (1987).

[6.8] A.M. Antoine, B. Drevillon, and P. Roca I Cabarrocas, J. Non-Cryst. Solids **77,78,** 769 (1985).

[6.9] B. Drevillon, J. Perrin, J.M. Siefert, J. Huc, A. Lloret, G. de Rosnay, and J.P.M. Schmitt, Appl. Phys. Lett. **42,** 801 (1983).

[6.10]B. Drevillon, J. Huc, and N. Boussarssar, J. Non-Cryst. Solids **59,60,** 735 (1983).

[6.11]B. Drevillon and F. Vaillant, Thin Solid Films, **124,** 217 (1985).

[6.12]J.C. Knights, R.A. Lujan, M.P. Rosenblum, R.A. Street, and D.K. Biegelson, Appl. Phys. Lett. **38,** 331 (1981).

FIGURES

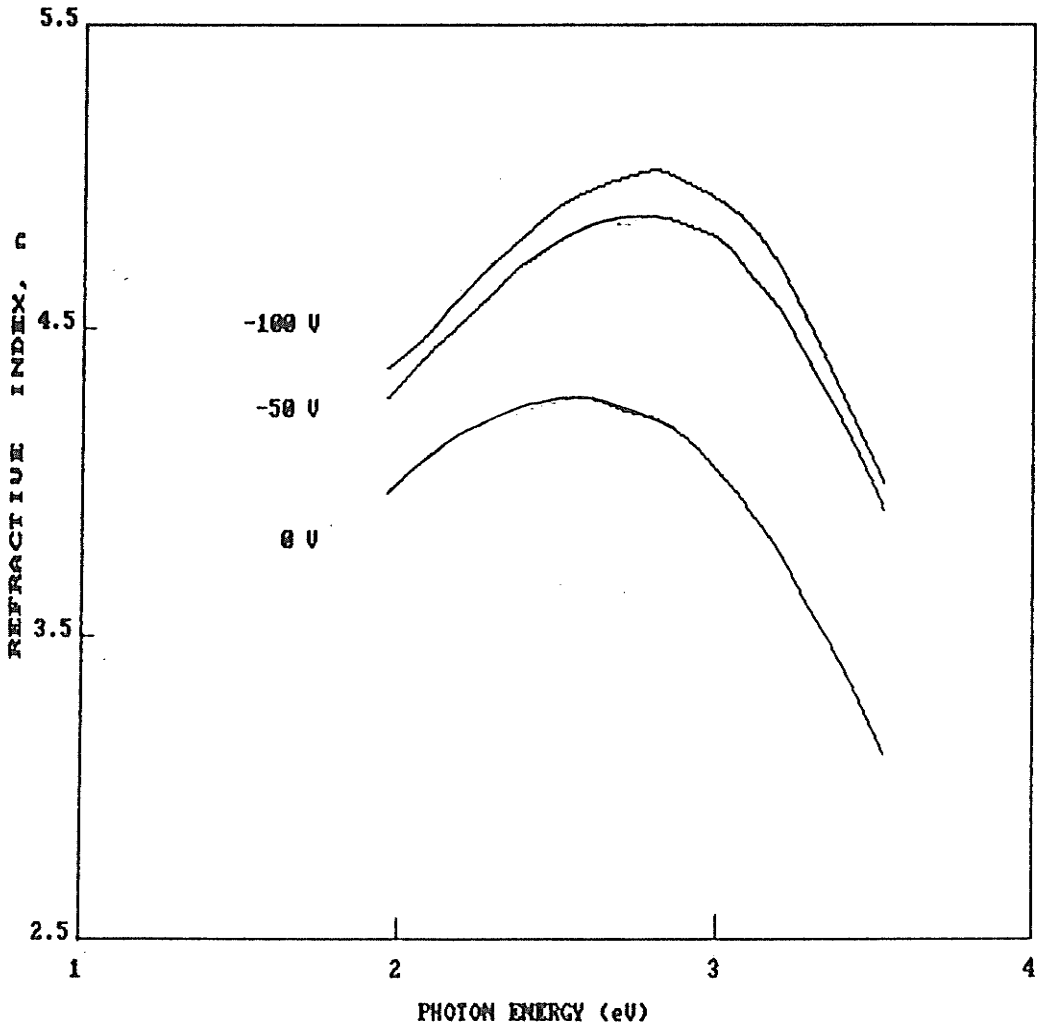

Fig. 6.1 The refractive index, n, as a function of photon energy for a-Si:H films deposited on stainless steel substrates. The substrate bias voltage, V_b, is indicated.

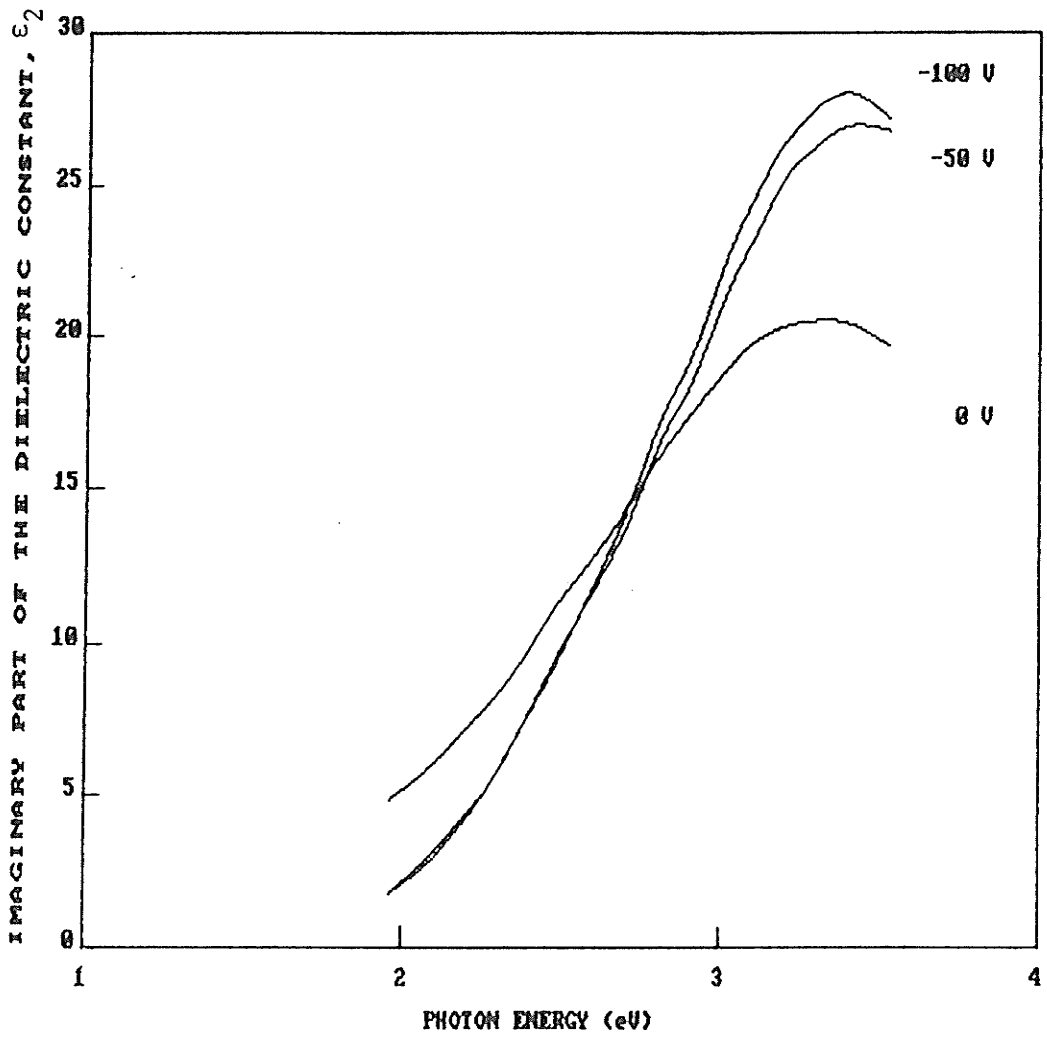

Fig. 6.2 The imaginary part of the dielectric constant, ϵ_2, as a function of photon energy for a-Si:H films deposited on stainless steel substrates. The substrate bias voltage, V_b, is indicated.

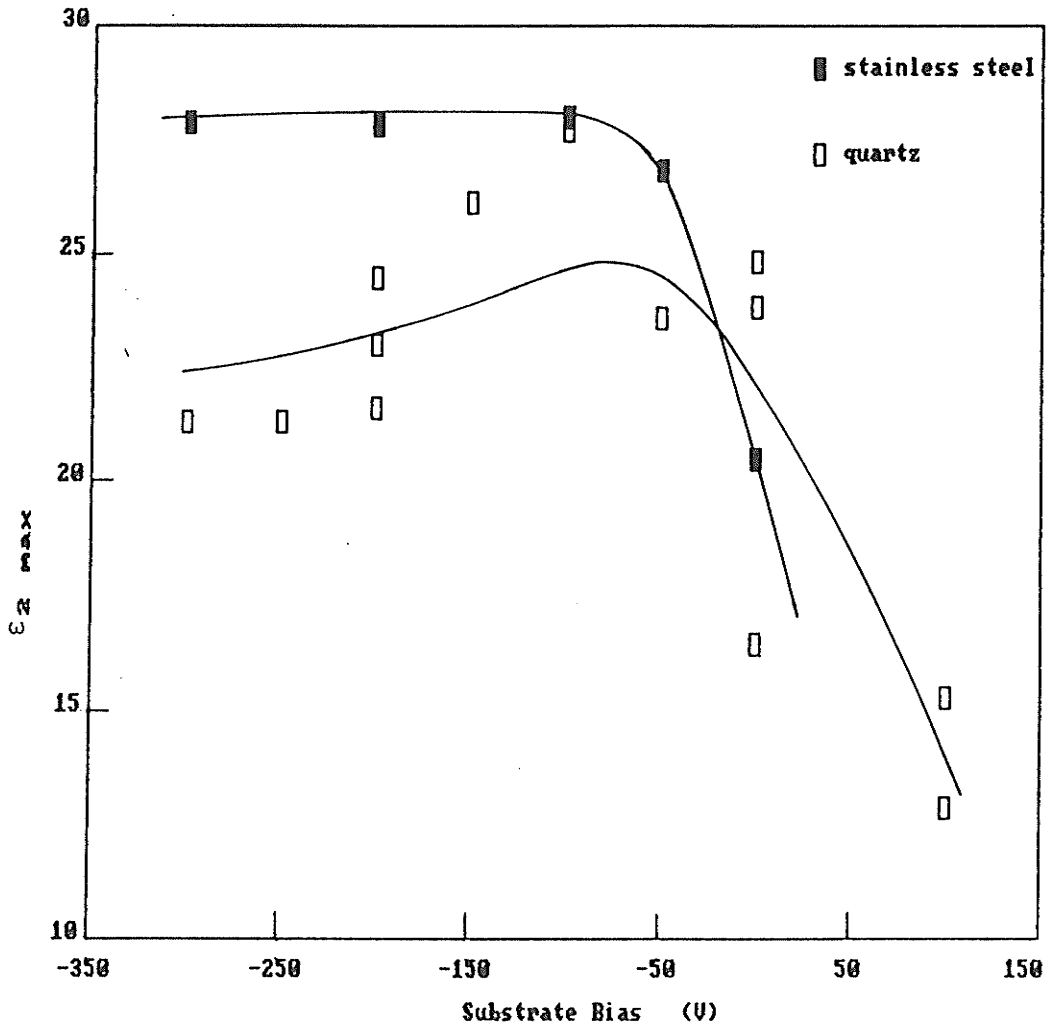

Fig. 6.3 The maximum value of the imaginary part of the dielectric constant, $\epsilon_{2\,max}$, as a function of substrate bias, V_b, for a-Si:H films deposited on stainless steel and quartz substrates.

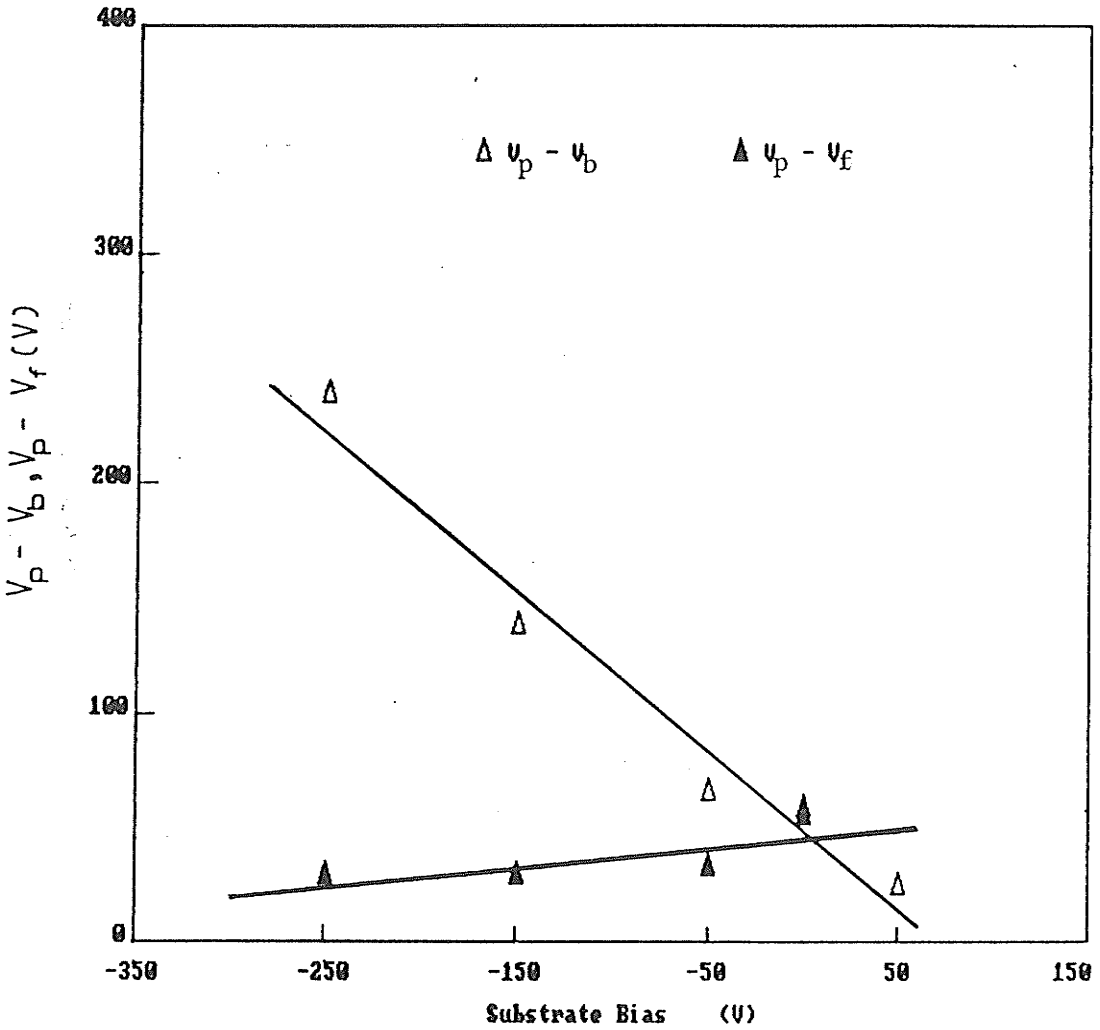

Fig. 6.4 The quantities $V_p - V_f$ and $V_p - V_b$ as a function of substrate bias voltage, V_b, where V_p and V_f are the plasma and floating potentials, respectively. Results are shown for a H_2 plasma at a pressure of 1 mtorr and 4 Watt absorbed microwave power.

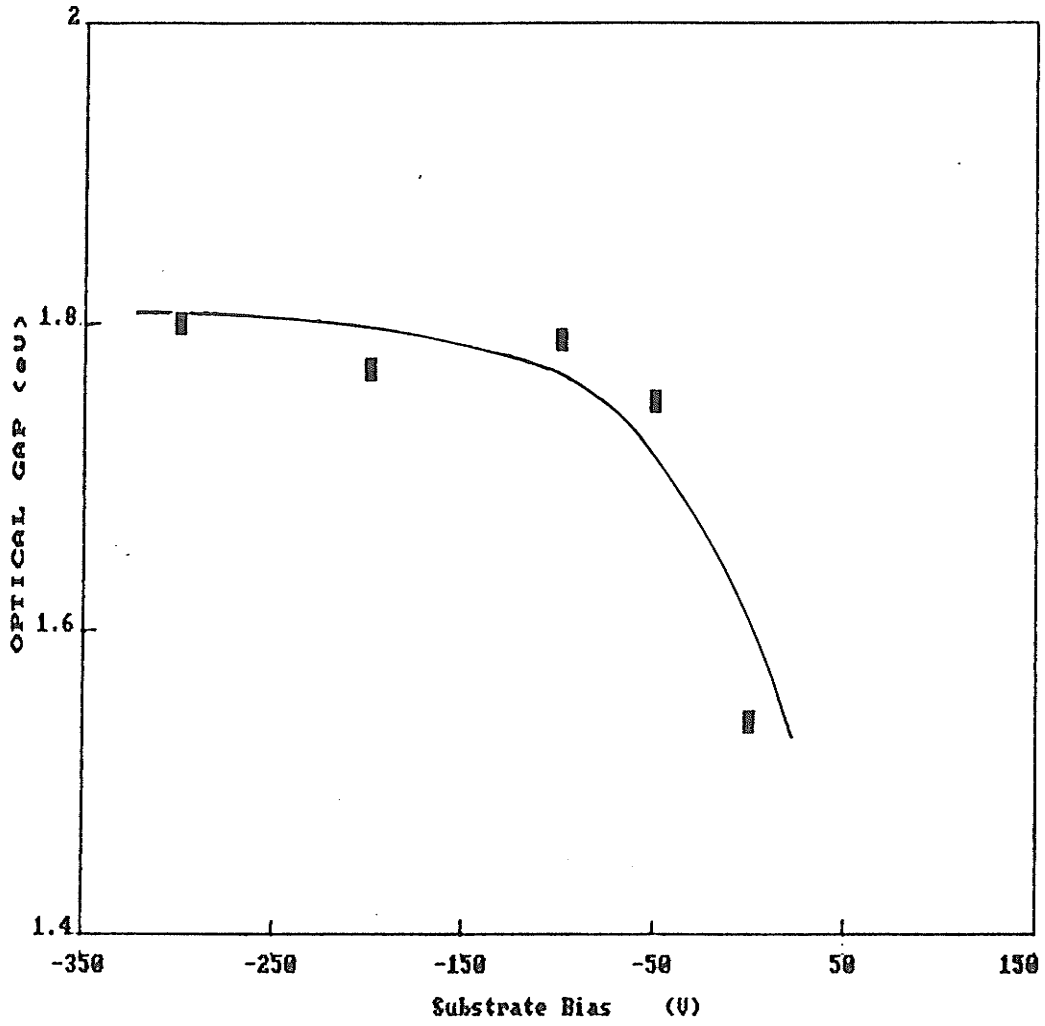

Fig. 6.5 Optical gap E_{opt} as a function of substrate bias V_b for a-Si:H films deposited on stainless steel substrates.

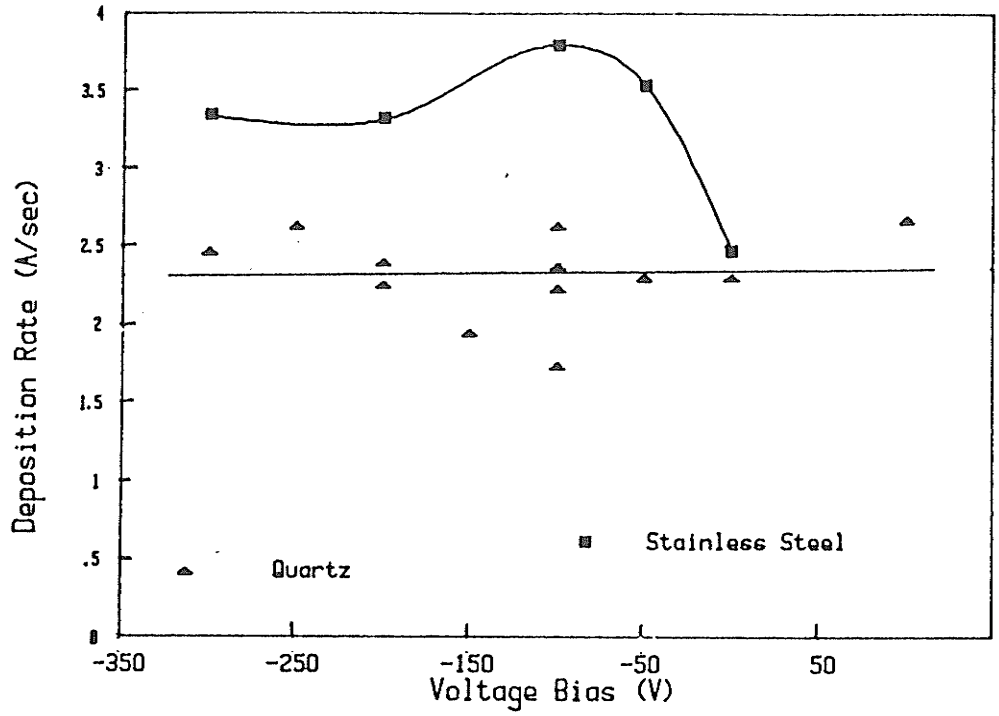

Fig. 6.6 **Deposition rate as a function of substrate bias V_b for a-Si:H films deposited on stainless steel and quartz substrates.**

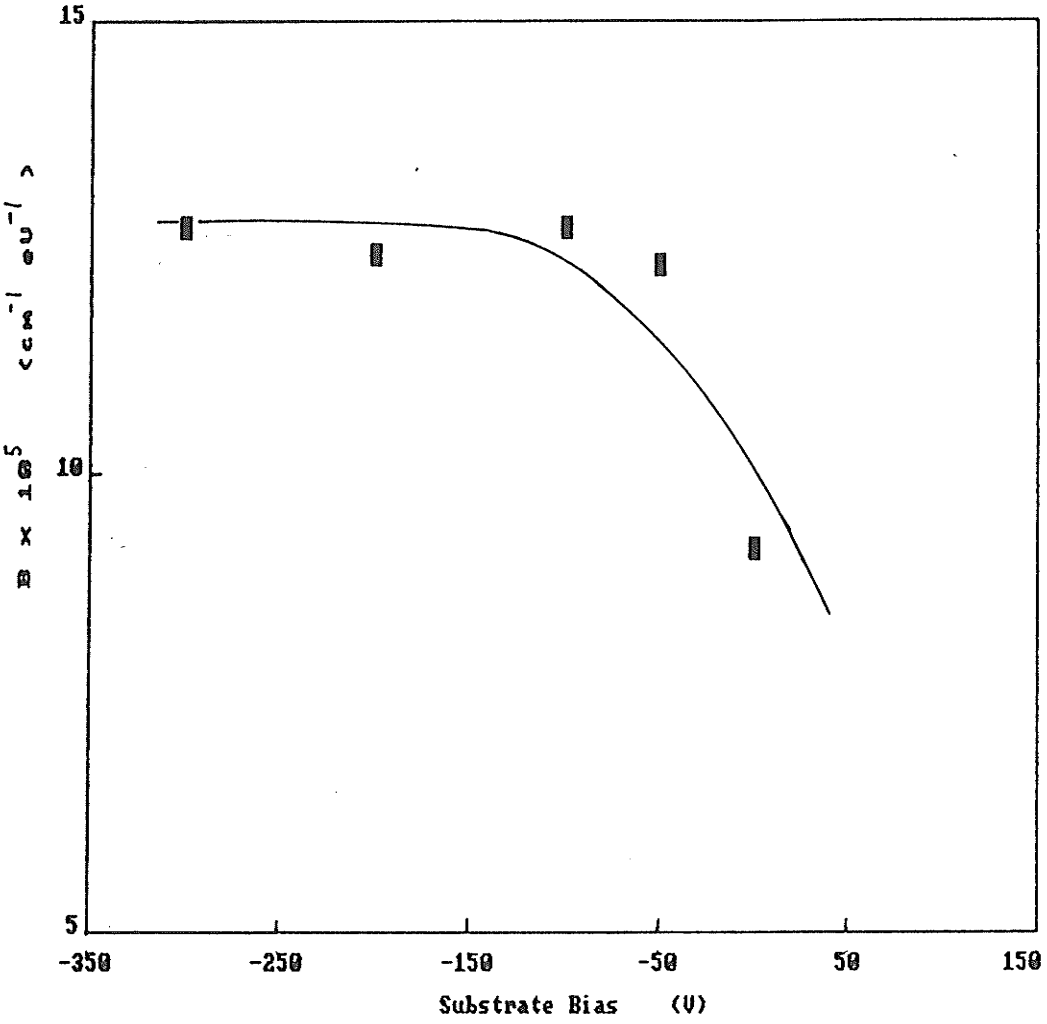

Fig. 6.7 The B-parameter defined by $\alpha h\nu = B(h\nu - E_{opt})^2$ as a function of substrate bias V_b, for a-Si:H films deposited on stainless steel substrates.

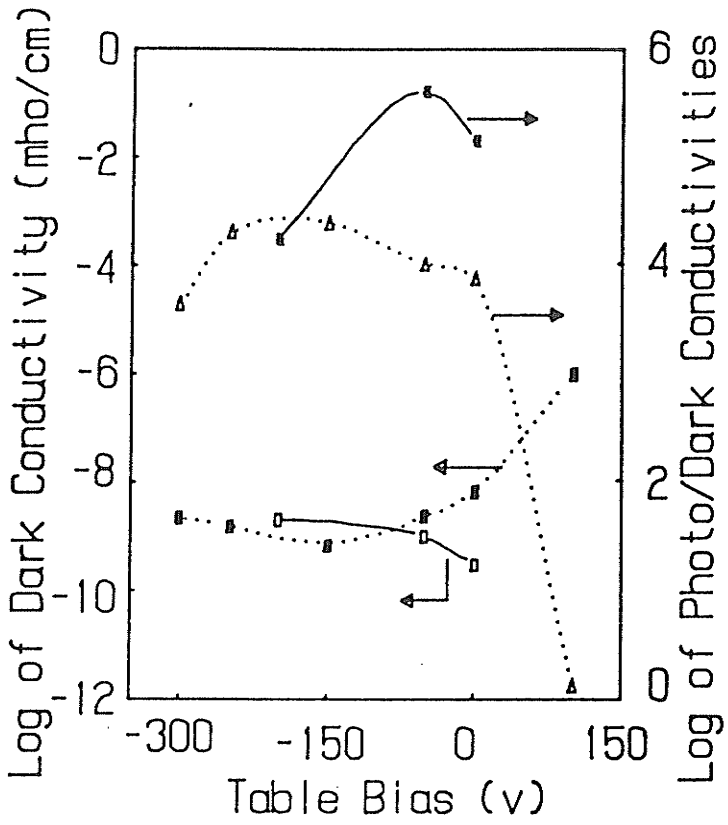

Fig. 6.8 Dark conductivity, σ_d, photoconductivity, σ_{ph}, and σ_{ph}/σ_d at room temperature as functions of table bias for a-Si:H films deposited on stainless steel (solid line) and quartz substrates (dotted line). Photoconductivity data is shown for a photon flux of 10^{15} photons-s^{-1}-cm^{-2} at λ = 6328 A.

CHAPTER 7

CONCLUDING REMARKS

For undoped a-SiN_x:H for $0 \leq x \leq 0.6$, the activation energy for extended-state electron conduction as well as the optical gap are unaffected by N content for $x \leq 0.4$. The electron mobility in extended states is improved by as much as a factor of 10 by the N incorporation. There is a rapid conversion from the tetrahedral network to a Si_3N_4 network as x increases above $\simeq$ 0.4.

Optical measurements over the range of $2.0 < h\nu < 3.5$ eV of both amorphous and microcrystalline hydrogenated silicon indicates that the optical gap decreases from 1.70 eV to 1.40 eV as the structure changes from an amorphous network into a microcrystalline-amorphous mixture. The amorphous to microcrystalline transition is clearly indicated by the spectra of the refractive index n, and the imaginary part of the dielectric constant ϵ_2. Modelling these films as multilayer structures shows that the transition from amorphous to microcrystalline films is accompanied by a reduction in material density and a significant increase in the surface roughness overlayer. X-ray diffraction measurements estimate a higher volume fraction of crystallites as compared to that obtained from optical data. The measurement of the ϵ spectra provide an alternative technique to x-ray diffraction in the investigation of amorphous and microcrystalline structure, and may be particularly useful for thin films.

For fabrication of hydrogenated silicon in microwave plasmas, some ion bombardment during film growth is favourable due to the resultant enhancement of the film density and the reduction of dihydrides. A moderate amount of ion bombardment also tends to increase the deposition rate and to improve the optical and electronic quality of these films. The optimum ion energy required appears to be approximately 100 eV in microwave plasmas operating at 1 mTorr.